Optical characterization of Ge- and InGaAs-semiconductor detectors for high accuracy optical radiant power measurements in the near infrared

Der Fakultät für Elektrotechnik, Informationstechnik und Physik
der Technischen Universität Carolo-Wilhelmina
zu Braunschweig

zur Erlangung des Grades eines
Doktors der Naturwissenschaften
(Dr.rer.nat.)
genehmigte
Dissertation

von Marco Antonio López Ordoñez
aus La Huerta, Mexiko

1. Referent: Priv. Doz. Dr. Stefan Kück
2. Referent: Prof. Dr. A. Hangleiter

eingereicht am: 12. Dezember 2007
mündliche Prüfung (Disputation) am: 27. März 2008
Druckjahr: 2008

Vorveröffentlichungen der Dissertation

Teilergebnisse aus dieser Arbeit wurde mit Genehmigung der Fakultät für Physik, vertreten durch den Mentor Priv. Doz. Dr. Stefan Kück, in folgenden Beiträgen vorab veröffentlicht:

Publikationen:

M. López, H. Hofer, K. D. Stock, J. C. Bermúdez, A. Schirmacher, F. Schneck, S. Kück, "Spectral reflectance and responsivity of Ge- and InGaAs-photodiodes in the near-infrared: measurement and model," Appl. Opt. **46**, 7337-7344 (2007).

M. López, H. Hofer, S. Kück, "High accuracy measurement of the absolute spectral responsivity of Ge and InGaAs trap detectors by direct calibration against an electrically calibrated cryogenic radiometer in the near-infrared," Metrologia **43**, 508 – 514 (2006).

M. López, H. Hofer, S. Kück, "Measurement of the absorptance of a cryogenic radiometer cavity in the visible and near infrared," Metrologia **42**, 400 – 405 (2005).

Tagungsbeiträge:

S. Kück, H. Hofer, M. A. López Ordoñez, "Cryogenic Radiometer-Based High Accurate Measurement of Ge and InGaAs Trap Detector Responsivity" in *Conference on Lasers and Electro-Optics/Quantum Electronics and Laser Science Conference and Photonic Applications Systems Technologies 2006 Technical Digest* (Optical Society of America, Washington, DC, 2006), CTuV6.

M. López, H. Hofer, S. Kück, "Measurement of the absorptance of a cryogenic radiometer cavity in the visible and near infrared (NIR)," Proceedings of the *9th International Conference on New Developments and Applications in Optical Radiometry* (NEWRAD 2005), J. Gröbner ed., 17-19 October 2005, Davos, Switzerland.

TABLE OF CONTENTS

1 Introduction

Nowadays optical fiber systems play a very important role in the field of telecommunications since they are the most efficient way to transport information (voice, data or video). To ensure that an optical fiber system works appropriately, it is necessary to have each of its components well characterized. An optical fiber system is composed basically of an optical light source, i.e. a laser, an optical fiber as the transmission medium, and an optical detector as the receiver. Here, the most basic measurement necessary is the optical flux or optical radiant power. Moreover, a fiber optic system, due to his flexibility by light transporting, is also used for other applications in different fields, i.e. spectroscopy, biomedical, space, military, automotive, metal-industry, etc. where the optical power measurement is also important.

The measurement of the optical radiant power is carried out with an optical power meter. It consists basically of an optical detector with its corresponding attached electronics. In most of the cases, the optical detector limits the spectral wavelength range and the measurement accuracy. Optical detectors can be classified in two groups [1]: photon detectors and thermal detectors. Photon detectors are quantum detectors based on the photoelectric effect, which converts a photon into an emitted electron or an electron-hole pair, i.e. phototubes, photodiodes, photoconductors, etc. Thermal detectors are based on a photothermal effect, which converts optical energy into heat, i.e. thermopiles, pyroelectric detectors, etc. For applications with fiber optics, photodiodes based in semiconductor materials like silicon (Si), germanium (Ge) or indium gallium arsenide (InGaAs) are used mostly because of their high speed response and high responsivity in the near infrared, where optical fiber communication systems are operated. Si photodiodes are typically used in multimode optical fiber applications, where the wavelength of the laser source used is around 850 nm. Ge and InGaAs photodiodes are used in single mode optical fiber systems. Here the wavelength of the laser source can be chosen between 1230 nm and 1675 nm.

It is known that the responsivity of a photodiode may change with its use over the time [2]; i.e. ageing of the diode responsivity or contamination of the sensitive surface, especially if it is not operated at stable conditions, which is often the case for optical power meters used in installed optical fiber networks. Confidence in optical power measurements is obtained, if the photodiode responsivity is well known and verified frequently. This is reached by calibrating the photodiode against a standard, whose traceability to primary standards is well established. Therefore, many national metrology institutes (NMIs) offer a calibration service for this quantity. In Germany, the institute in charge of defining and maintaining the national primary standards is the Physikalisch-Technische Bundesanstalt (PTB)[1], who provides also measurement or calibration services to secondary laboratories or to the industry.

Figure 1.1 shows the traceability chart of the PTB for the measurement of the optical power for fiber optic applications. Here, the accuracy level decreases along the chain of traceability, as the uncertainty of the high level standards is inherited to lower levels. The instrument capable of reaching, until now, the lowest measurement uncertainty is the cryogenic radiometer. Under specific conditions this instrument can achieve relative standard uncertainties below 10^{-4} [3, 4, 5]. Therefore, it has been adopted in the PTB and also in many NMIs, as a primary standard for the measurement of the absolute optical radiant power Φ, whose unit is Watt [6,7,8]. As the typical transfer standard, a trap detector is used [9,10, 11]. It is constructed of several photodiodes aligned to trap most of the incident radiation more efficiently as in the case of a single photodiode. For the visible and near-infrared spectrum, from 400 nm to 1100 nm, Si photodiodes are used in the trap detector so that by calibrating directly against the cryogenic radiometer, a relative standard uncertainty of ± 0.01 % can be achieved. Here, the calibration is carried out at a single wavelength (632.8 nm) and single optical power level, see Figure 1.1 For the near-infrared, where the optical fiber systems are operated, a spectrally non-selective thermal detector (thermopile) is used as a “calibration” standard [12, 13]. In this case, only the variation in reflectance of the detector as function of wavelength is required. Thereby, a thermopile can reach a relative standard uncertainty around ± 0.15 % between the visible and the near infrared. Although the advantage of a thermopile is precisely its “spectrally flat” response, it has also some disadvantages: low response time, high noise at low radiation level, vulnerability to damage from heating, aging, hardening, and physical contact [14,15].

The main goal of this project was the optical characterization of Ge and InGaAs detectors, both single and trap configuration, for their use as transfer standards in the near infrared, especially for the wavelengths where the optical fiber communication systems are operated.

---

[1] Physikalisch-Technische Bundesanstalt (PTB)
Bundesallee 100, D-38116 Braunschweig, Germany

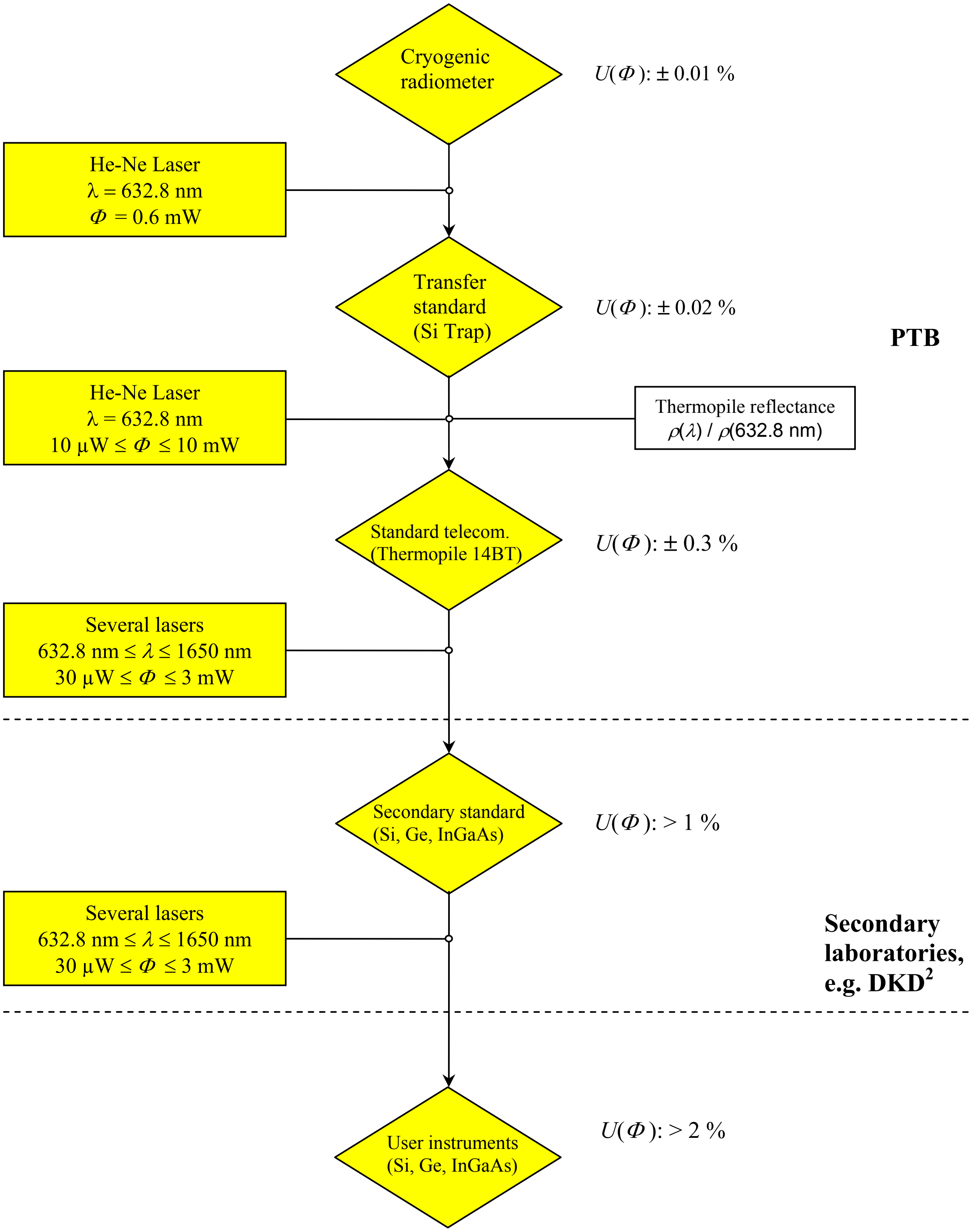

Figure 1.1 Traceability chart for the measurement of the optical radiant power for fiber optic applications. $U(\Phi)$ is the relative expanded uncertainty ($k = 2$).

---

[2] Deutscher Kalibrierdienst (DKD)
Bundesallee 100, D-38116 Braunschweig, Germany

This involves the measurement of the absolute spectral responsivity, nonlinearity, external and internal quantum efficiency, and the spatial non-uniformity.

In this project, Ge- and InGaAs-trap detectors were calibrated directly against the cryogenic radiometer in order to achieve the lowest available uncertainty in the measurement of the absolute responsivity in the near infrared. This implied a careful optical characterization of the optical beam used in the measurement as well as of the cryogenic radiometer itself. Therefore, a new measurement setup was implemented. This uses two tuneable laser sources operating between 1260 nm and 1360 nm and between 1460 nm and 1620 nm. The optical characterization of the cryogenic radiometer involved the measurement of the cavity absorption [16] and Brewster-angle window transmission in these wavelength ranges. The maximum relative standard uncertainty achieved in this measurement does not exceed 0.04 % for all wavelengths investigated. Until now, this is the lowest relative uncertainty worldwide reported for this spectral wavelength range. In addition, these trap detectors will probably replace the thermopile and the Si-trap detector in the traceability chart of the PTB shown in Figure 1.1, which will improve the accuracy significantly.

The determination of the internal quantum efficiency of the photodiodes implies also the measurement of the spectral reflectance of the diodes. In this work the spectral reflectance and responsivity of Ge- and InGaAs-single photodiodes at near-normal and oblique incidence (45°) were also investigated [17]. The measurements were carried out with s- and p-polarized radiation in the wavelength range from 1260 nm to 1640 nm. The spectral reflectance of both photodiodes was modeled by using the matrix approach developed for thin-film optical assembles [18]. This allows the calculation of the photodiode responsivity for any incident angle over the whole spectral range investigated. These data were also used to calculate the spectral responsivity of the Ge- and InGaAs-trap detectors. The difference obtained between calculated and measured spectral responsivity were similar to the one reported in [19] for Si photodiodes.

Another important parameter studied in this project was the nonlinearity of the photodiodes at high irradiance levels. Here, two new measurement setups were developed for the nonlinearity measurement. As a radiation source, a high power laser at 980 nm and an optical amplifier (Erbium Doped Fiber Amplifier, EDFA) operated at 1550 nm were used. One measurement setup was based on the differential spectroradiometry (DSR) method [20] and the other one was based on a simple relative method that uses only a fiber optic coupler (90/10). Both setups were proofed and validated with the classical flux addition method [21] used typically for low optical power levels ≤ 15 mW.

This thesis is organized basically in five parts. In the first part of the thesis, included in chapter 2 to 4, a brief description of the basic theory of photodiodes, description of the photodiodes to be characterized, the working principles of the cryogenic radiometer and its characterization are given. The second part is given in chapter 5, where the description of the different setups used for the photodiodes characterization is included. The third part in chapter 6 deals with the measurement results and some discussions. The fourth part includes the estimation of the measurement uncertainty of each of the characterized parameters, which is given in chapter 7. A summary and outlook of the work is given in the fifth part included in chapter 8.

2 Basic theory

2.1 Fundamentals of photodetectors

Photodetectors are semiconductor devices that convert, through electronic processes, an optical signal into an electrical signal. There are several types of photodetectors, for example: photoconductors, junction photodiodes (*p-n*, *p-i-n*, Schottky photodiodes, etc.), phototransistors, etc. For fiber optics applications the most used photodetectors are the *p-n* and *p-i-n* junction photodiodes because of their short response time and high responsivity in the near-infrared region (800 nm to 1650 nm). Although the operation principle of these types of photodiodes can be found elsewhere [22,23,24], in this section the most important principles are briefly given.

Basically, in a junction photodiode there are three processes present:

(1) carrier generation by incident light,
(2) carrier transport, and
(3) interaction of current with an external circuit to provide the output signal.

Figure 2.1 shows a schematic representation of a *p-i-n* photodiode and an energy-band diagram under reverse-bias together with the optical absorption characteristics. Photons with energy $h\nu \geq E_g$ (energy band gap of the semiconductor) are absorbed in the photodiode and produce electron-hole pairs. The absorption depends on the radiation wavelength and with it the penetration depth $1/\alpha$ (α: absorption coefficient) of the radiation (see Figure 1 (c)), which generate electron-hole pairs in different places cross the photodiode. Electrons and holes generated in the depletion layer quickly drift in the opposite direction under the influence of the strong electrical field E which can be also affected by an external bias voltage V_{bias}. Since the electrical field always points in the *n-p* direction, electrons move to the *n* side and holes to the *p* side (Figure 2.1(b)). Thus, a photocurrent is generated in an external circuit. Electron-hole pairs generated outside the depletion layer, but in its vicinity, have a high probability of entering the depletion layer by random diffusion. If so, an electron coming from the *p* side is quickly transported across the junction and therefore contributes to the photocurrent. A hole generated in the *n* side has also the same effect. Nevertheless, electron-hole pairs generated away from the depletion layer have very low probability to reach the depletion layer because of the absence of the electrical field. So, it is most probability that they are annihilated by recombination and therefore they do not contribute to the photocurrent.

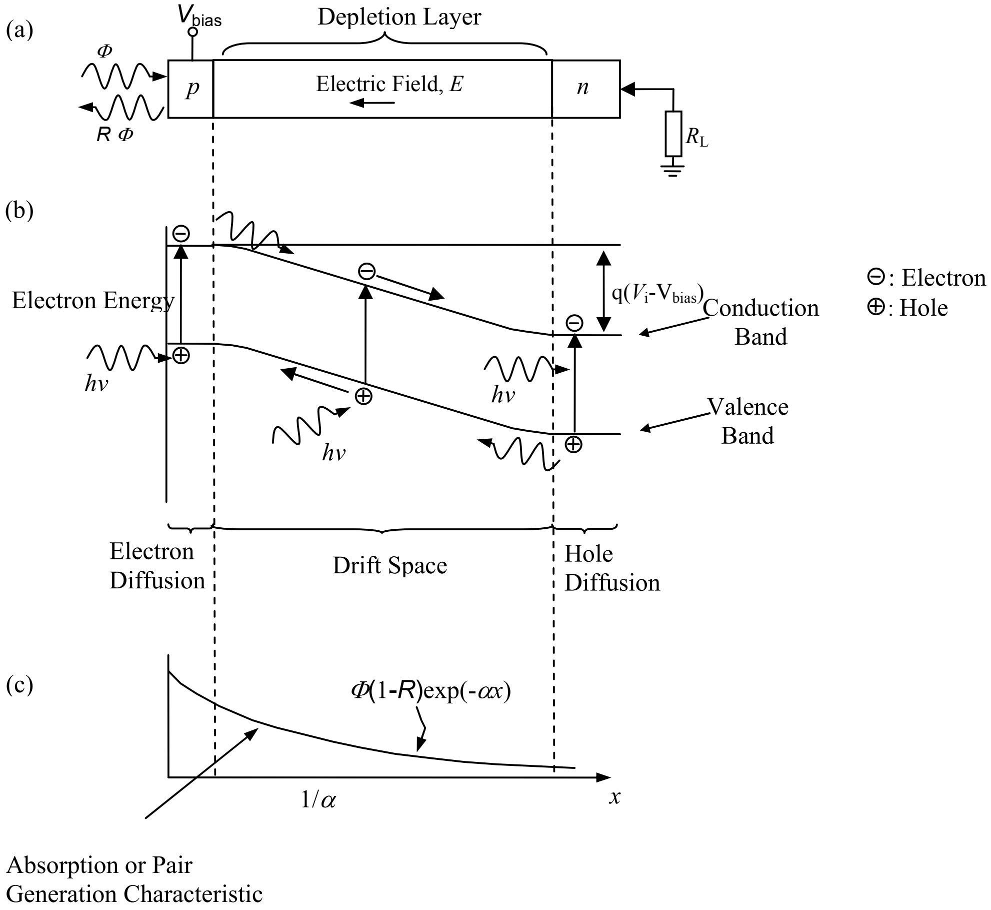

Figure 2.1 Schematic representation of the photodiode operation. (a) Cross-section view of *p-i-n* diode. (b) Energy-band diagram under reverse bias. (c) Carrier generation characteristic. (according to Ref. [25]).

Although the discussion given above is based on reverse-bias *p-i-n* photodiode, the basic principles discussed apply also for a photodiode with an external reverse or forward bias voltage V_{bias}. An external bias voltage V_{bias} modify basically just the width W of the photodiode depletion layer given by,

$$W = \sqrt{\frac{2(V_{\text{i}} - V_{\text{bias}})\varepsilon\varepsilon_0 (N_{\text{A}} + N_{\text{D}})}{qN_{\text{A}}N_{\text{D}}}}, \tag{2.1}$$

where V_{i} is the built-in potential, q is the electron charge, ε is the dielectric constant, ε_0 is the permittivity in a vacuum and N_{A} and N_{D} are the acceptor and donator concentration, respectively.

Under steady-state conditions the total current density through the depletion layer is given by

$$J_{\text{tot}} = J_{\text{dr}} + J_{\text{diff}} \tag{2.2}$$

where J_{dr} is the drift current density due to carriers generated inside the depletion region and J_{diff} is the diffusion current density due to carriers generated outside the depletion layer in the bulk of the semiconductor and diffusing to the reverse-biased junction. Assuming that the thermal generated current is negligible and the surface *p* layer is much thinner than $1/\alpha$, the hole-electron generation rate is given by

$$G(x) = F_0 \alpha \exp(-\alpha x) \tag{2.3}$$

where F_0 is the incident photon flux per unit area given by $\eta_{\text{int}}\Phi(1\text{-}R) / Ahv$, where η_{int} is the internal quantum efficiency, Φ is the optical radiation power, R is the reflection coefficient, A is the device area, h is Planck's constant and v is the radiation frequency. Thus, the drift current J_{dr} is given by

$$J_{\text{dr}} = -q\int_0^W G(x)dx = qF_0(1 - \exp(-\alpha W)). \tag{2.4}$$

For $x > W$, the minority-carrier density (holes) in the bulk semiconductor is determined by one-dimensional diffusion equation [22]

$$D_{\mathrm{p}} \frac{\partial^2 p_{\mathrm{n}}}{\partial x^2} - \frac{p_{\mathrm{n}} - p_{\mathrm{n0}}}{\tau_{\mathrm{p}}} + G(x) = 0 \tag{2.5}$$

where D_{p} is the diffusion coefficient for holes, τ_{p} the lifetime of excess carriers, and p_{n0} the equilibrium hole density. The solution of equation (2.5) under the boundary conditions $p_{\mathrm{n}} = p_{\mathrm{n0}}$ for $x = \infty$ and $p_{\mathrm{n}} = 0$ for $x = W$ is given by [26]

$$p_{\mathrm{n}} = p_{\mathrm{n0}} - \left(p_{\mathrm{n0}} + C_1 \exp(-\alpha W)\right) \exp\left(\frac{W - x}{L_{\mathrm{n}}}\right) + C_1 \exp(-\alpha x) \tag{2.6}$$

with

$$L_{\mathrm{p}} = \sqrt{D_{\mathrm{p}} \tau_{\mathrm{p}}} \quad \text{and} \quad C_1 = \left(\frac{F_0}{D_{\mathrm{p}}}\right) \frac{\alpha L_{\mathrm{p}}^2}{1 - \alpha^2 L_{\mathrm{p}}^2},$$

where L_{p} is the diffusion length of the excess carriers.

The diffusion current density is given by [22]

$$J_{\mathrm{diff}} = -q D_{\mathrm{p}} \left(\frac{\partial p_{\mathrm{n}}}{\partial x}\right)_{x=W},$$

$$J_{\mathrm{diff}} = q F_0 \frac{\alpha L_{\mathrm{p}}}{1 + \alpha L_{\mathrm{p}}} \exp(-\alpha W) + q p_{\mathrm{n0}} \frac{D_{\mathrm{p}}}{L_{\mathrm{p}}} \tag{2.7}$$

and the total current density is obtained as

$$J_{\mathrm{tot}} = q F_0 \left(1 - \frac{\exp(-\alpha W)}{1 + \alpha L_{\mathrm{p}}}\right) + q p_{\mathrm{n0}} \frac{D_{\mathrm{p}}}{L_{\mathrm{p}}}. \tag{2.8}$$

The latter term in equation (2.8) is the term for saturation current density due to holes in a non-illuminated diode, which is also known as dark current. Normally the dark current of a photodiode is very small ($\approx 10^{-10}$ A), so that the total photocurrent

$$I_{\mathrm{ph}} = A \cdot J_{tot} = \frac{q \cdot \Phi \cdot (1-R)}{h\nu} \cdot \eta_{\mathrm{int}} \cdot \left(1 - \frac{\exp(-\alpha W)}{1+\alpha L_{\mathrm{p}}}\right) \tag{2.9}$$

is proportional to the optical power.

Equation (2.9) can be used to define the external quantum efficiency η_{ext} (number of electron-hole pairs generated per incident photon) of the photodiode. That is,

$$\eta_{\mathrm{ext}} = \frac{I_{\mathrm{ph}}/q}{\Phi/h\nu} = (1-R) \cdot \eta_{\mathrm{int}} \cdot \left(1 - \frac{\exp(-\alpha W)}{1+\alpha L_{\mathrm{p}}}\right). \tag{2.10}$$

Photodiodes with high external quantum efficiency are always desirable in radiometry, especially when these are used as transfer standards for optical power measurements. According to equation (2.10), in order to achieve high external quantum efficiency, low reflection coefficient R and $\alpha W >> 1$ are required. Generally, an antireflection coating (AR-coating) is deposited on the photodiode surface to minimize the reflection coefficient (see section 3). On the other hand, the photodiode absorption can be increased by expanding the depletion layer, which is typically achieved by applying a reverse bias, especially for *p-n* junction photodiodes. For the case of a *p-i-n* photodiode, the intrinsic material (very lightly doped) placed between the *p* and *n* regions extends the depletion layer over the whole volume of this part of the device, which increases greatly the external quantum efficiency.

For a typical *p-i-n* photodiode, for example a photodiode based on a Ge semiconductor with absorption coefficient $\alpha = 10^4$ cm^{-1} for $\lambda \approx 1230$ nm and $W = 10$ µm, the term $\exp(-\alpha W)$ in equation (2.10) results to 4.54×10^{-5}. So, in the practice, the external quantum efficiency can be defined as

$$\eta_{\mathrm{ext}} = (1-R)\eta_{\mathrm{int}}. \tag{2.11}$$

One of the most important parameter of a photodiode is its responsivity S, which relates the optical power to the photocurrent. The responsivity of a photodiode is defined as the ratio between the generated photocurrent I_{ph} and the incident optical radiant power Φ,

$$S = \frac{I_{\mathrm{ph}}}{\Phi} = \frac{q}{h \cdot c} \cdot \lambda \cdot \eta_{\mathrm{ext}}, \qquad [\mathrm{A/W}]. \tag{2.12}$$

In an ideal case, the internal quantum efficiency of the photodiode is $\eta_{\mathrm{int}} = 1$ and the reflection coefficient $R = 0$. This gives that $\eta_{\mathrm{ext}} = 1$ and the resulted responsivity is then,

$$S = \frac{1}{1.24} \cdot \lambda \qquad [\mathrm{A/W}], \tag{2.13}$$

where λ is given in µm.

This ideal case is only possible, if all electron-hole pairs are generated in the depletion region. However, in a real photodiode the absorption coefficient is wavelength dependent and with it also the location of the electron-hole pairs generation, as mentioned previously. Thus, the internal quantum efficiency is normally lower than one. Equation (2.12) may only be used as a general estimation of the photodiode responsivity.

Since the absorption coefficient is a strong function of the wavelength, the responsivity of a given photodiode is then limited by the long-wavelength cutoff λ_{c} established by the energy gap E_{g} of the semiconductor. That is,

$$\lambda_{\mathrm{c}} = \frac{hc}{E_g} \cdot \tag{2.14}$$

For example, in the case of Ge with an $E_g = 0.67$ eV at 300 K, this long-wavelength cutoff occurs at 1.88 µm.

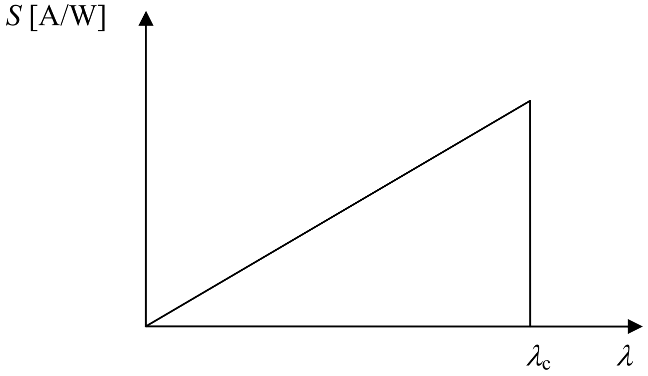

Figure 2.2 Example of the responsivity S of a photodiode in an ideal case where $\eta_{\text{int}} = 1$.

2.2 Operation modes of a photodiode

A photodiode can be operated basically in three different modes: open circuit (photovoltaic), short-circuit, and reverse biased (photoconductive). The generated output signal depends on the photodiode operation mode and it can be obtained using its equivalent circuit, see Figure 2.3 and 2.4.

(a) Photovoltaic mode (open circuit, $R_L = \infty$), see Figure 2.3 (a) and equation (2.15a):
In this mode, most of the electron-hole pairs are generated in the depletion region. The additional free electron on the *n* side recombines with the holes on the *p* side, and vice versa. This increases the electric field, which produces a built-in potential V_d across the junction that increases with increasing the incident optical power. In this case, the responsivity of the photodiode is not linear and is measured in $V \cdot W^{-1}$ rather than in $A \cdot W^{-1}$.

(b) Photoconductive mode (reverse bias), see Figure 2.3 (b) and equation (2.15b):
In this mode frequently a serial resistance is inserted in the circuit. There are some reasons why a photodiode is used in this mode. First, a strong reverse bias creates a high electrical field in the junction which increases the drift velocity of the carriers. Second, as mentioned previously, a reverse bias increases also the width of the depletion layer, thereby reducing the

junction capacitance and improving the response time. Furthermore, a wider depletion layer leads to a larger photosensitive area, making it easier to collect more light.

(c) Short-circuit mode (with $R_L \approx 0$), see Figure 2.3(b) and equation (2.15c):

In this mode a short-current is generated, which is simply the photocurrent I_{ph}. For the measurements of the optical power with photodiodes, this mode is preferably used. This is because the photocurrent measurement is direct and the photodiode has the larger linearity range due to the lower dark current. Furthermore, in this mode there are considerably few problems with the temperature sensitivity of the dark current. Generally, the measurement of the photocurrent is carried out through an operational amplifier used as a current- to voltage-converter, which has an input impedance virtually ≈ zero.

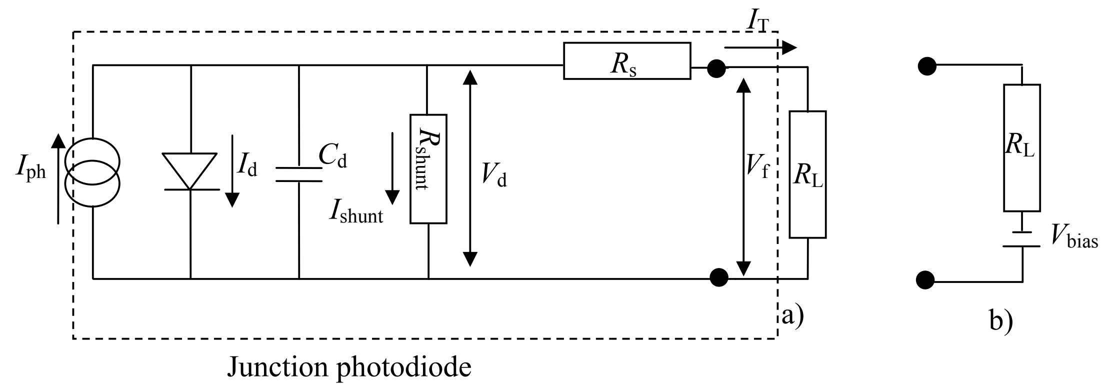

Figure 2.3 Equivalent circuit of a junction photodiode with an external load resistance R_L. a) Photovoltaic mode ($R_L = \infty$) or short-circuit mode ($R_L \approx 0$) and b) Photoconductive mode. I_{ph} = photocurrent; I_{shunt} = shunt current; V_d = diode voltage; V_f = output voltage; V_{bias} = bias voltage; C_d = junction capacitance; I_T = output current; R_{shunt}: shunt resistance and R_s: serial resistance.

(a)

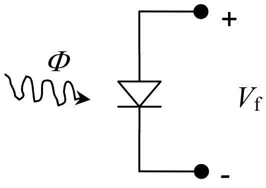

$$V_{\mathrm{f}} = \frac{kT}{q}\ln\left(\eta_{\mathrm{ext}}\frac{\Phi q\lambda}{hcI_{\mathrm{sat}}}\right) \tag{2.15a}$$

(b)

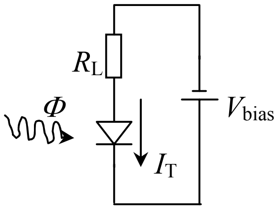

$$I_{\mathrm{T}} = I_{\mathrm{ph}} - I_{\mathrm{sat}}\left(\exp\left(\frac{q\left(V_{\mathrm{d}} - V_{\mathrm{bias}}\right)}{kT}\right) - 1\right) + \frac{V_{\mathrm{d}} - V_{\mathrm{bias}}}{R_{\mathrm{shunt}}} \tag{2.15b}$$

(c)

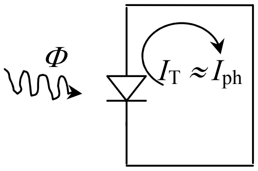

$$I_{\mathrm{T}} \approx I_{\mathrm{ph}} = \eta_{\mathrm{ext}}\frac{q\lambda}{hc}\Phi \tag{2.15c}$$

Figure 2.4 Operation modes of a photodiode. (a) Photovoltaic mode (open circuit), (b) Short-circuit (Photovoltaic mode with $R_{\mathrm{L}} \approx 0$) and (c) Photoconductive mode (reverse bias).

3 Devices investigated

3.1 Ge- and InGaAs-single photodiodes

There are several types of photodiodes with different sizes and shapes commercially available. Most of the characteristics of the photodiode depend not only on the type of the semiconductor material, but also on the sensitive area size. Photodiodes with large sensitive area have typically high responsivity and large linear range. However, the capacitance (short response time), dark current and Noise Equivalent Power (NEP) increase with the sensitive area size. So, the selection of a photodiode depends on the application. For metrological applications in radiometry, where high responsivity and large linearity play a very important role, photodiodes with large sensitive area are used preferably.

In this project the photodiodes to be characterized were chosen with the largest sensitive area commercially available. The Ge- (Hamamatsu B1920-01) and the InGaAs-photodiode (Anadigics, 35PD10M) had sensitive areas of 78.54 mm^2 (circular with a diameter of 10 mm) and 100 mm^2 (rectangular 10 mm × 10 mm), respectively. The detectors were mounted on a black aluminum housing designed and fabricated at the PTB. A temperature sensor (Pt100) was mounted in the housing, close to the photodiode, to monitor the temperature of the diode during the measurement process. Figure 3.1 shows a photograph of the photodiodes investigated.

Figure 3.1 Ge- (model: Hamamatsu B1920-01) and InGaAs- (model: Anadigics 35PD10M) photodiodes. The Ge- and InGaAs-photodiode had a sensitive area of 78.54 mm^2 and 100 mm^2, respectively.

The basic structures of the photodiodes investigated in this project are shown in Figure 3.2 Both photodiodes have a planar diffuse structure. The Ge-photodiode is composed of a *p-n* junction, which uses precisely a Ge semiconductor as the material base. The *p*- and *n*-regions are formed by doping the Ge semiconductor with arsenic and gallium, respectively. SiO_2 is deposited and patterned to form a window for the subsequent *p*-type dopant. On the front surface, ohmic metal contacts are patterned to allow light to enter the device, whilst the back is a planar ohmic metal contact. To minimize the reflection losses from the top surface, an antireflection coating of Si_xN_y is placed on the top of the photodiode.

Unlike the Ge-photodiode, the InGaAs-photodiode is composed of two different semiconductor materials, InGaAs and InP, which form a *p-i-n* heterojuntion $InP/In_{0.53}Ga_{0.47}As/InP$. In this structure, an intrinsic low doped $In_{0.53}Ga_{0.47}As$ layer is grown on the top of a *n*-type InP:S substrate. Generally this intrinsic layer is made thick enough (>1μm) to absorb most of the incident radiation in this region. The *p*-layer is formed of InP doped with zinc. An antireflection coating (Si_xN_y) is also used here to provide low reflections from the top surface and also act as passivation for the device. The ohmic contact on the front surface, like the Ge-photodiode, is formed by etching away a small region of the antireflection coating and depositing an ohmic metal contact. The *n*-side ohmic metal contact is deposited on the backside of the wafer on the InP:S substrate.

Photodiode with a *p-i-n* structure have some advantages and disadvantages compared to a *p-n* structure.

Advantage of a *p-i-n* structure:

- The width of the depletion layer of the device increases with the *i*-layer, which increase the area available for capturing light. This improves the responsivity of the photodiode.
- Increasing the width of the depletion layer reduces the junction capacitance and thereby the *RC* time constant.
- Reducing the ratio between the diffusion length and the drift length of the photodiode results in a greater proportion of the generated current being carried by the faster drift process.

Disadvantage of a *p-i-n* structure:

- Due to the increasing of the width of the depletion layer, the transit-time τ_{dr} of carriers drifting across the depletion layer is also increased.

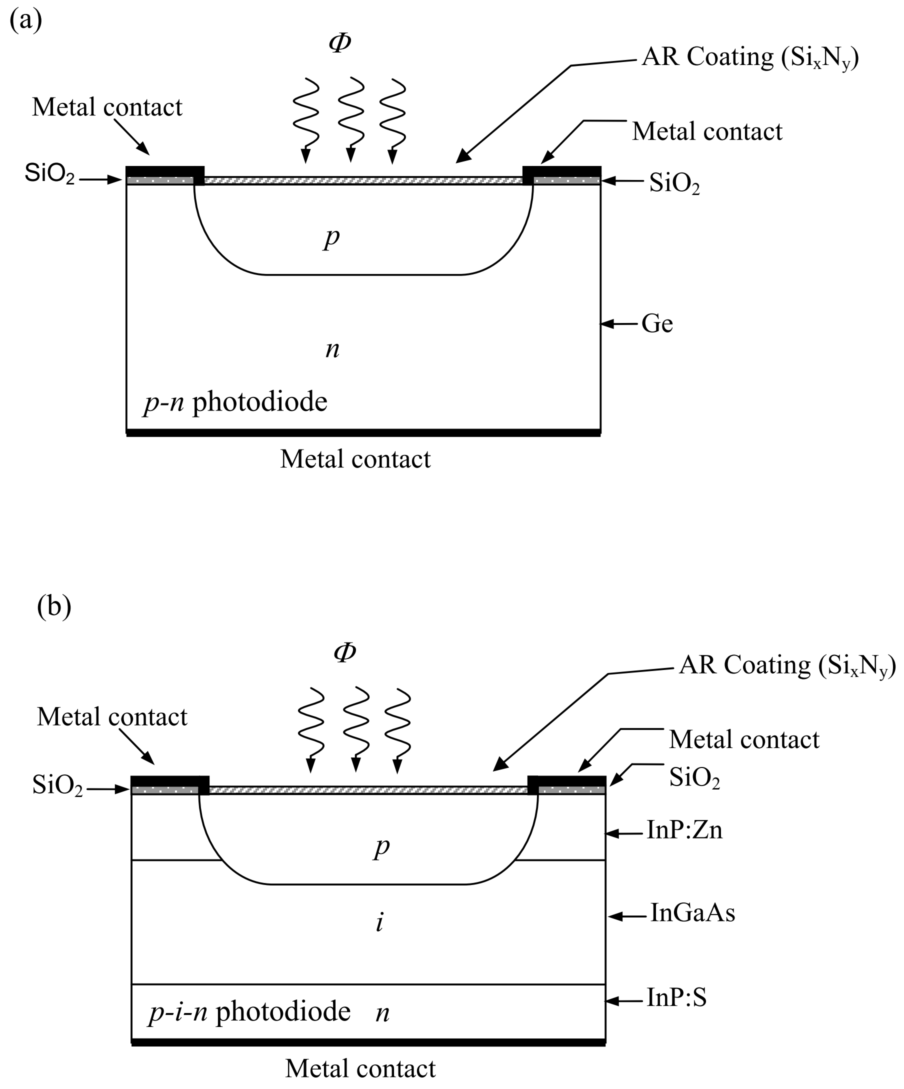

Figure 3.2 Structure of the photodiodes under characterization: (a) *p-n* Ge-photodiode and (b) *p-i-n* InGaAs-photodiode.

3.2 Ge- and InGaAs-trap detectors

A trap detector, as mentioned in section 1, is formed by several photodiodes aligned to trap or absorb most of the incident radiation. These detectors are used typically in most of the NMIs as transfer standards because of their high capability to transfer the absolute radiometric scale from the cryogenic radiometer to the user. There are several types of trap configurations [27, 28, 29]; e.g. the three-dimensional configuration (reflexion trap), a transmission trap, a tunnel trap, etc. The most popular configuration is the three-dimensional shown in Figure 3.3. Here, the photodiodes are connected in parallel and arranged each to lie in a different plane, in order to reduce the sensitivity to the polarization of the incident radiation. The first two photodiodes are placed at an angle of 45° with respect to the incident radiation and the third one at normal angle. Thus, the incident radiation undergoes five specular reflections before emerging from the trap detector and is therefore nearly totally absorbed. The responsivity of the trap is given by,

$$S_{\mathrm{trap}}(\lambda) = \frac{q\eta_{\mathrm{int}}\lambda}{hc}\left(1 - \prod_{\mathrm{i}=1}^{n} R_{\mathrm{i}}\right) \tag{3.1}$$

where n is the number of reflections and R_{i} is the reflectance of each photodiode.

A trap detector has several properties, which makes it more suitable as a transfer standard than a single photodiode; e.g. good homogeneity, linearity, spectral responsivity stability, etc. One of the most important properties is that the internal quantum efficiency of a trap detector can reach almost one when the quality of the semiconductor material of the photodiodes is good, which is the case for Si-photodiodes. The main limitation of a trap detector is its angular field of view, which is restricted by the long path length of the radiation necessary to activate five internal reflections. Typically, the field of view of a trap detector varies between 3° and 8° grad. This depends on the trap design and the sensitive area of the photodiodes.

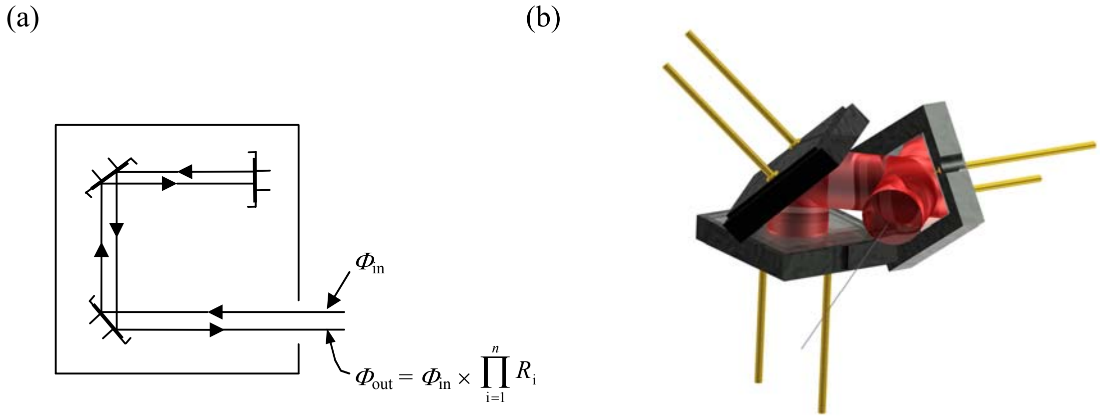

Figure 3.3 Trap detector (a) Schemes and (b) three-dimensional picture.

The trap detectors investigated in this project are shown in Figure 3.4. These are formed with three single Ge-photodiode from Hamamatsu (B1920-01) and InGaAs-photodiodes from Telcom Devices (35PD10), respectively. All photodiodes are windowless and have a sensitive area of 78.54 mm^2 (Ge-photodiodes) and 100 mm^2 (InGaAs-photodiodes), respectively. The photodiodes are connected in parallel and mounted on a skeleton that uses the three dimensional configuration described above. The distance between the photodiodes was optimized in order to allow a 3° angle of view of the device. Moreover, the skeletons have an incorporated Pt100 temperature sensor, which allows an accurate temperature monitoring during the measurement. Both skeleton and housing were designed in the PTB.

(a)

(b)

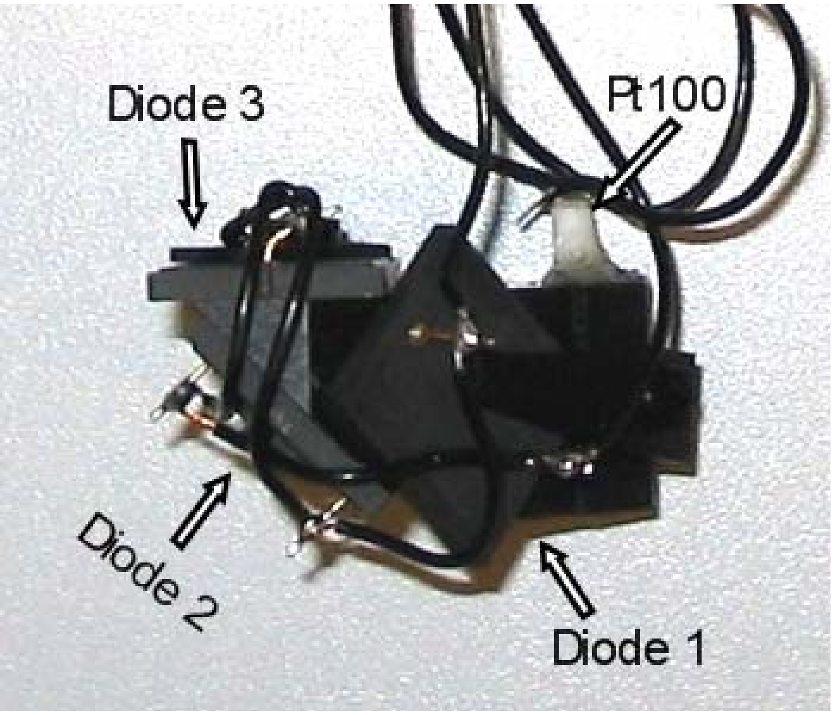

Figure 3.4 (a) Ge- and InGaAs-trap detectors mounted on a housing. (b) Photodiodes on the skeleton. The first two photodiodes are placed with an angle of 45° with respect to the incident light beam and the third one is placed at a normal angle.

4 Cryogenic radiometer

4.1 Electrical Substitution Radiometer

An Electrical Substitution Radiometer (ESR) is basically a thermal detector that measures optical radiant power by comparison to an equivalent amount of electrical power. Figure 4.1 shows a schematic diagram of an ESR. It is formed basically by a cavity, which, through a thermal link, is kept at a constant temperature by a heat sink. The principle of operation of such radiometer is as follows: First, without incident radiation (by closed shutter), the cavity is maintained at a reference constant temperature T_0. Second, by opening the shutter, the optical radiation power Φ raises the temperature of the cavity to $T_c = T_0 + T_1$. Here, T_1 is the raise temperature, which can be found by solving the equation (Putley 1980) [30]

$$\alpha\Phi = H\left(\frac{dT_1}{dt}\right) + GT_1\,, \tag{4.1}$$

where H is the thermal capacitance of the cavity, G is the thermal conductivity of the link and α is the cavity absorptance. After a long time ($t \to \infty$), once the temperature of the cavity has reached its equilibrium state, the solution of equation (4.1) gives the raise temperature:

$$T_1 = \frac{\alpha\Phi}{G}\,, \tag{4.2}$$

so, the final temperature of the cavity results as,

$$T_c - T_0 = \frac{\alpha\Phi}{G}\,. \tag{4.3}$$

Third, when the shutter is closed again, the electrical power of the cavity is increased to a sufficient amount to maintain the cavity temperature at the same temperature level T_c reached when the shutter is open. Thus, the optical power is equal to the electrical power P dissipated in the heater circuit, which is given by

$$P = i^2 R, \tag{4.4}$$

where i is the increased current applied through the heater of resistance R required to maintain the temperature stability. The advantage of this method is that the electrical current and the resistance can be measured very accurate. However, correction factors due to non-equivalence generated by small differences between the effect of radiant and electrical heating must be applied. Moreover, the absorption coefficient α of the cavity and the thermal conductivity of the link G have to be known.

ESRs have shown to be a good option for the optical radiation power measurements, when the uncertainty required is not lower than 0.1 %. Typically, an ESR can achieve uncertainties in the range from 0.1 % to 0.3 %. The performance of such radiometers is limited generally by the thermal properties of the materials at ambient temperatures (298 K) and some other correction factors, e.g. absorption of the incident radiation and the non-equivalence between the optical and the substituted electrical power. An alternative to improve the ESR accuracy is by modifying the cavity geometries and cooling it at cryogenic temperatures. Thereby, the correction factors can be reduced by approx. a factor 100.

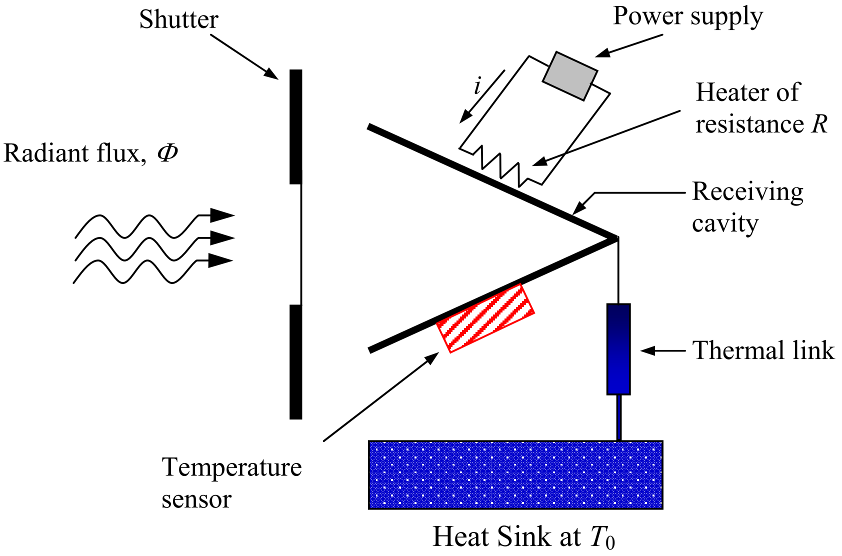

Figure 4.1 Schematic diagram of an electrical substitution radiometer. The total radiant flux is collected by a receiving cavity, in this case a cone. The temperature of the cavity T_c and the temperature of the heat sink T_0 are monitored by a temperature sensor system. When the shutter is closed, electrical power equivalent to the optical radiant power is applied by the power supply system, thereby substituting the optical radiant power.

Cooling the cavity of an ESR to very low temperatures has several advantages. The heat capacity of pure metals is dramatically decreased, which allows to construct large detector cavities that absorb almost 100 % of the light without incurring a large increase in the time constant of the detector. The non-equivalence errors due to differences in the temperature distributions in the cavity generated under radiant and electrical heating are strongly reduced due to the resulting higher thermal conductivity. As an example, the heat capacity and thermal conductivity of copper (Cu) cooled at cryogenic temperatures are shown in Figure 4.2. In this material, the heat capacity is reduced by a factor of 1000 at around 6 K and the thermal conductivity increases by a factor of 10 for the same temperature. Furthermore, thermal radiation losses of the absorber, power dissipation in the leads, etc. are practically negligible at such temperatures.

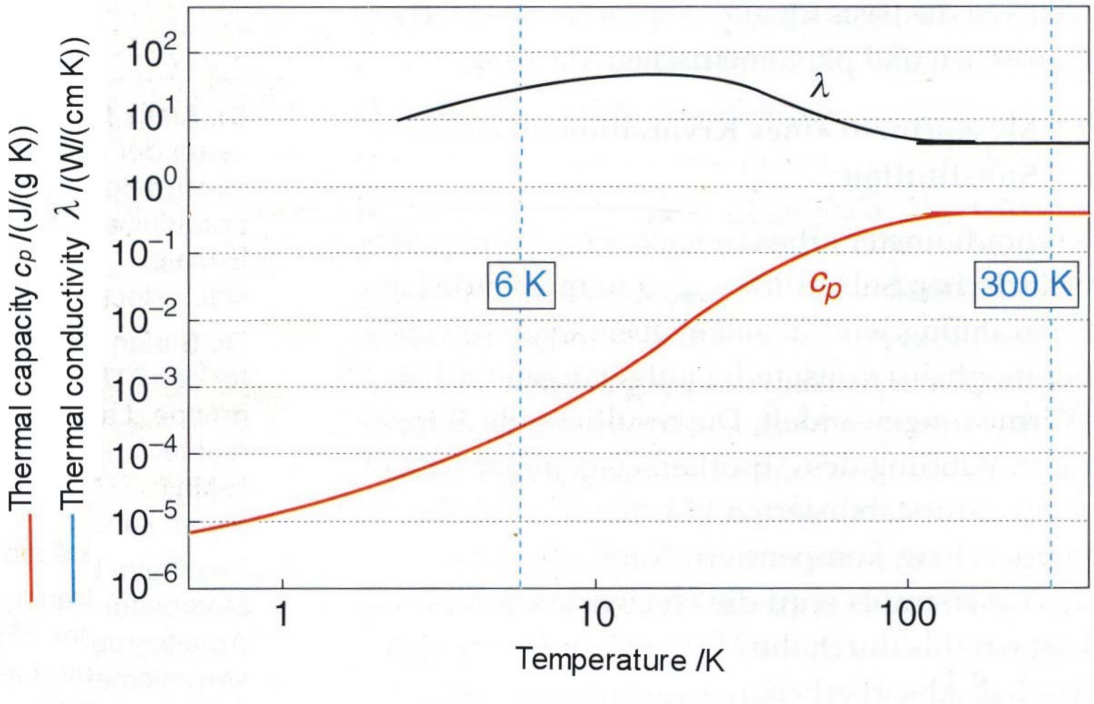

Figure 4.2 Temperature dependence of the thermal conductivity and thermal capacity of copper (Cu) [31].

4.3 Measurement of the absolute optical radiation power with the cryogenic radiometer

In this project, a commercial cryogenic radiometer LaseRad II from Cambridge Research & Instrumentation Inc. was used for the measurement of the absolute optical power. Figure 4.3 (a) and (b) show a schematic diagram and photo of the radiometer, respectively. It is formed of a cavity which is suspended with a heat sink and thermal link from a base plate of a liquid helium (4.2 K) reservoir. The heat sink is stabilized at a reference temperature of about 5 K. The thermal link is designed to give a temperature rise in the cavity of about 2 K when the input power to the cavity is 1 mW. Thus, the temperature of the cavity is maintained around 7 K. This temperature allows using a large cavity capable of absorbing most of the incident radiation. The cavity of this radiometer is made of an oxygen-free high-conductivity copper (OFHC) tube with a sloped bottom. It is approximately 6.0 cm long, has a diameter of approximately 0.5 cm and is coated internally with a black paint (Chemglaze Z 302), which by multiple internal reflections absorbs more than 99.98 % of the incident radiation in the visible wavelength range. Furthermore, the cavity has a temperature sensitivity of approx. 1.24 K/mW at 4.2 K.

The measurement principle of this radiometer is essentially very similar that of an ESR (see section 4.1). It uses the dynamic electrical power substitution method during the measurement process. In a first step, by opening the shutter, the laser beam hits the cavity producing a temperature rise on it, which is reduced immediately by the temperature controller by reducing the electrical power P of the cavity heater at exactly the amount of absorbed radiant power Φ. In a second step, by blocking the laser beam (shutter close), the cavity temperature decreases, and immediately the temperature controller increases the electrical power to the initial level (shutter open). Thus, the difference of the electrical power ΔP balances the absorbed radiant power Φ. Thereby, during the complete measurement cycle the temperature of the heat sink and the temperature of the cavity are kept almost exactly constant.

The electrical power difference ΔP is obtained by measuring the electrical voltage difference ΔV_{U} and the electrical current difference Δi of the cavity heater during a measurement cycle. Here, a measurement cycle means one sequence of electrical power measurement in each of the non-irradiated and irradiated states. Thus, the resulting electrical voltage difference ΔV_{U} is

$$\Delta V_{\mathrm{U}} = V_{\mathrm{U},1} - V_{\mathrm{U},2}\,, \tag{4.5}$$

where $V_{\mathrm{U},1}$ and $V_{\mathrm{U},2}$ are the voltages of the heater measured for the irradiated and non-irradiated state, respectively. The electrical current difference Δi is obtained by measuring the electrical voltage difference ΔV_{i} over an external 1 kΩ precision standard resistor R. That is,

$$\Delta i = \frac{\Delta V_{\mathrm{i}}}{R} = \frac{1}{R} \cdot \left(V_{\mathrm{i},1} - V_{\mathrm{i},2} \right), \tag{4.6}$$

where $V_{\mathrm{i},1}$ and $V_{\mathrm{i},2}$ are the voltages measured over the resistor R for the irradiated and non-irradiated state, respectively. Thus, the resulting electrical power difference ΔP is given by,

$$\Delta P = \Delta V_{\mathrm{U}} \cdot \Delta i$$

$$= \frac{\left(\Delta V_{\mathrm{U}} \cdot \Delta V_{\mathrm{i}} \right)}{R} = \frac{\left(V_{\mathrm{U},1} - V_{\mathrm{U},2} \right) \cdot \left(V_{\mathrm{i},1} - V_{\mathrm{i},2} \right)}{R}\,. \tag{4.7}$$

In an ideal case, the measured ΔP shall be equal to the optical radiation power Φ of the laser beam. However, in a real measurement with a cryogenic radiometer, ΔP deviates from the true optical power mainly because of two principal losses: the non-ideal absorptance $\alpha(\lambda)$ of the cavity and the non-ideal transmittance $\tau(\lambda)$ of the Brewster window. Both are wavelength dependent which cause that the measured optical power depends also on the wavelength. Thereby, the measured optical power corrected by these two factors is given by,

$$\Phi(\lambda) = \frac{\Delta P}{\alpha(\lambda) \cdot \tau(\lambda)}\,. \tag{4.8}$$

At cryogenic temperatures, the use of superconducting wires, e.g. wires of Niobium-Titanium (NbTi)[3], eliminates Joule heating losses in the heaters leads, which makes the errors due to the non-equivalence of the optical and electrical heating, the heat loss in the heater wiring, etc. small or negligible compared with the correction factors in equation (4.8).

---

[3] NbTi is a Type II superconductor with a critical temperature of 10 K

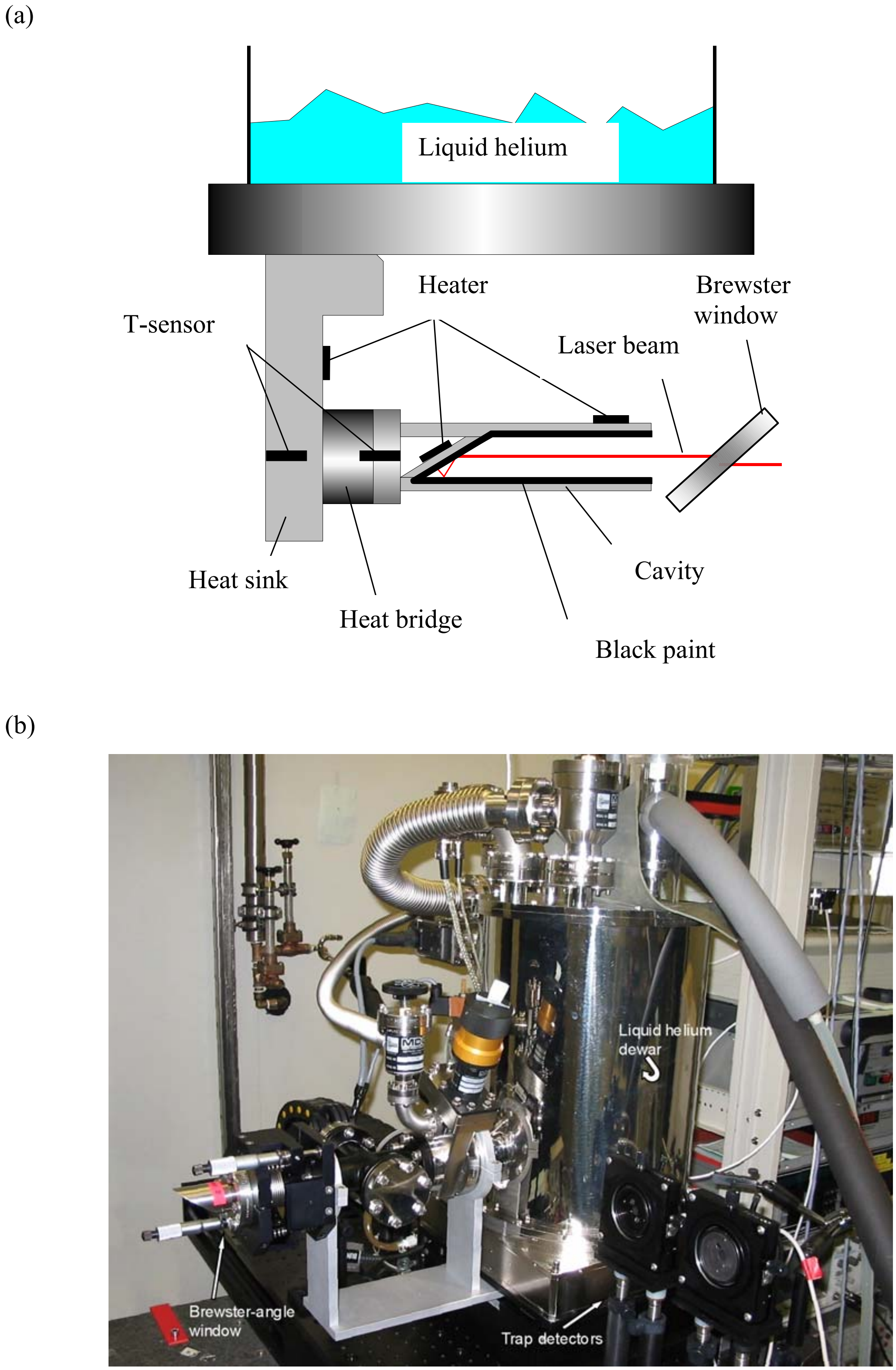

Figure 4.3 (a) Schematic diagram of a typical cryogenic radiometer. (b) Photo of the cryogenic radiometer LaseRad II from Cambridge Research & Instrumentation Inc. of the PTB.

4.4 Optical characterization of the cryogenic radiometer of the PTB

According to equation (4.8), the major correction factors that limit the accuracy of the cryogenic radiometer for optical power measurements are the non-ideal absorption coefficient $\alpha(\lambda)$ of the cavity and the non-ideal transmittance $\tau(\lambda)$ of the Brewster-angle window. These two factors are generally reported by the manufacturer, but just for the wavelength of 632.8 nm. For other wavelength ranges they may be considered to be constant, nevertheless, in this case a higher measurement uncertainty must be considered. To achieve lower measurement uncertainty, it is necessary to know the exact spectral response of both coefficients.

4.4.1 Reflectance measurement of the cavity absorptance

The absorption coefficient of the cavity was determined from the measurement of the diffuse reflection $\rho(\lambda)$ of the cavity given by

$$\alpha(\lambda) = 1 - \rho(\lambda). \tag{4.9}$$

The measurement was carried out by using a general-purpose integrating sphere that uses Spectraflect (barium sulphate) as a reflectance coating [32], see Figure 4.4. The measurement method consists basically of a relative comparison between the diffuse reflectance of a white standard and a 'sample' which in our case is the radiometer cavity. In a first step, a laser beam irradiates the cavity attached to the sample port, where most of the flux is absorbed and a small part reflected diffusely. The diffuse reflected flux is collected by the integrating sphere, from where a signal $S_c(\lambda)$ is generated by the photodetector. In this scheme the white standard is attached to the supplementary port. In a second step, the cavity and the white standard interchange their ports from where a second signal is generated $S_s(\lambda)$. A third signal $S_0(\lambda)$ is measured by taking off the white standard from the sample port. From the ratio between those signals the reflection coefficient of the cavity, ρ_c is obtained,

$$\frac{S_c(\lambda)-S_0(\lambda)}{S_s(\lambda)-S_0(\lambda)} = \frac{\rho_c(\lambda)}{\rho_s(\lambda)}\cdot\delta \rightarrow \rho_c(\lambda) = \frac{S_c(\lambda)-S_0(\lambda)}{S_s(\lambda)-S_0(\lambda)}\cdot\frac{\rho_s(\lambda)}{\delta}, \tag{4.10}$$

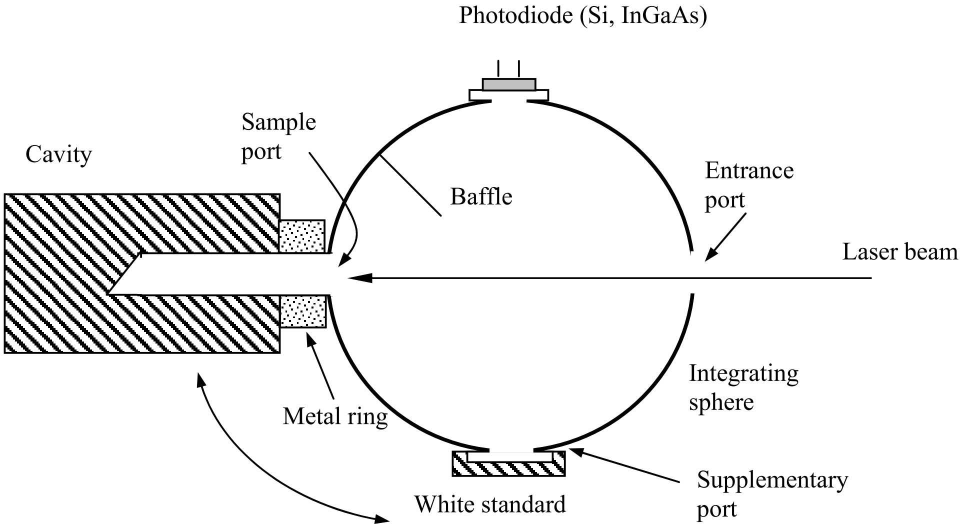

Figure 4.4 Measurement of the diffuse reflectance of the radiometer cavity by using an integrating sphere.

where $\rho_s(\lambda)$ is the reflection of the white standard and δ is the correction factor due to possible changes of the geometrical conditions of the sphere between the two measurement processes [33]. In this case, the whole characteristics of the sphere remains unchanged because all apertures have the same diameters, so $\delta = 1$.

Figure 4.5 shows the complete experimental setup used for the measurement of the diffuse reflectance of the cavity. The measurement was carried out in the visible wavelength range as well as in the near infrared. In the visible wavelength range, a He-Ne laser operating at 632.8 nm with an optical power of approx. 10 mW is used as radiation source. The beam irradiates a 2-mm diameter circular aperture and is imaged 1:1 by a 200 mm focal length lens - passing through the sphere - into the cavity. To reduce the fluctuation of the laser power, an external stabilizer is used. In addition, the laser beam is divided by a plan-parallel plate and monitored by a monitor detector. An attenuator and a polarizer are used to maintain the power level and the linear polarization of the laser beam. The detector placed on the sphere for the measurement at 632.8 nm is a Si detector of 5-mm diameter (Hamamatsu S1227 66BR). The photocurrent generated by the detector is converted to voltage by a trans-impedance amplifier, whose output voltage is measured by a digital-voltmeter.

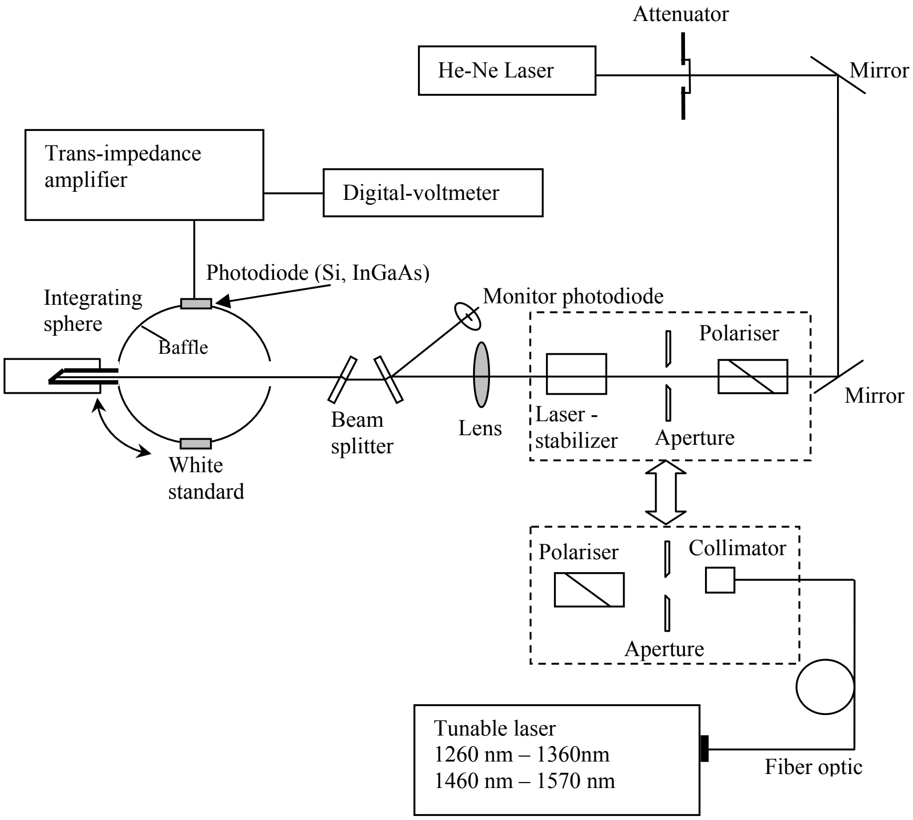

Figure 4.5 Experimental set-up used to measure the diffuse reflectance of the radiometer cavity.

For the measurement of the cavity reflectance in the IR, two tunable diode laser sources were used as radiation sources (Agilent 81600B), whose wavelength were adjusted from 1280 nm to 1360 nm and from 1480 nm to 1620 nm, respectively. The outputs of the laser sources are fiber optic connectors; therefore an external collimator with a fiber optic pigtail is used to collimate the laser beam. The laser-stabilizer, used during the measurement at 632.8 nm, is not needed for the measurement in the IR, instead, the collimator was placed front of the aperture. An InGaAs-photodiode (Telcom 35PD5M) of 5-mm diameter placed on the integrating sphere carries out the measurement of the reflected fluxes.

Figure 4.6 shows the results of the absorption coefficient measurements. At 632.8 nm the absorption coefficient obtained was 0.999885, which matches very well with the value reported by the manufacturer (0.999879). At the infrared wavelengths, the absorption coefficient varies from 0.999765 to 0.999785 between the wavelength ranges of 1280 nm – 1360 nm and 1480 nm – 1620 nm, respectively. The deviation observed for these ranges is 19×10^{-6}, which means that in this spectral range the value of the absorption coefficient is practically flat. Thus, for the whole NIR wavelength range, a value of 0.999777 ± 0.000014 can be used. Although no significant difference in the absorptance within the infrared spectral range investigated is observed, the mean value for the NIR range is about 1.1×10^{-4} lower than the value at 633 nm. This difference can be significant in the total correction factor of the CR, especially when one wish to reach uncertainties lower than 10^{-4}.

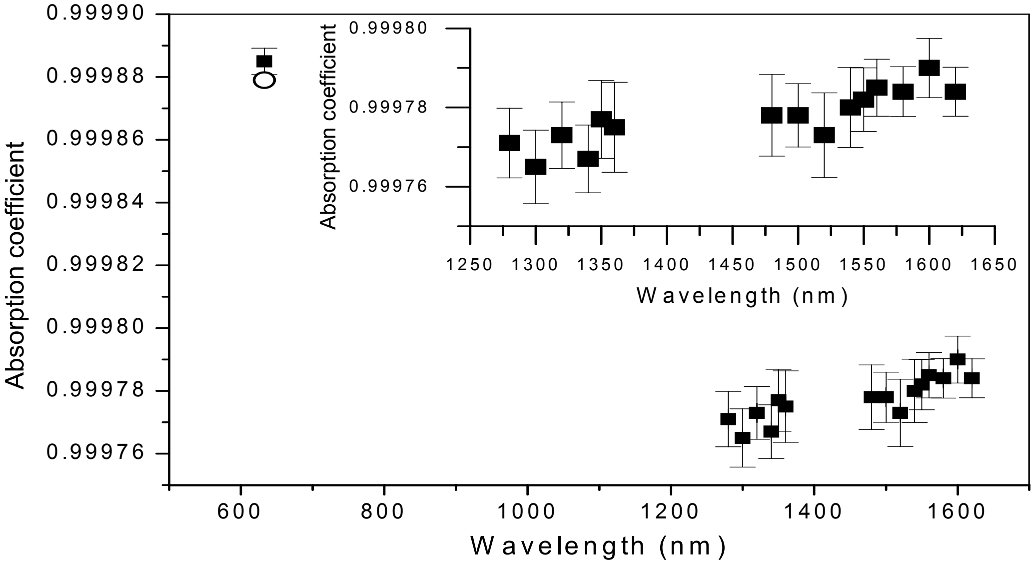

Figure 4.6 Absorption coefficients of the cavity measured in the visible and at near infrared wavelengths. The error bars correspond to the standard uncertainty of the measurement. Open circle: manufacturer result.

4.4.2 Transmittance measurement of the Brewster-angle window

The transmittance measurement of the Brewster-angle window was carried out in a similar way as described in [34]. It consists in measuring the radiant power of a laser beam with and without the Brewster-window. Figure 4.7 shows the experimental arrangement used for the transmittance measurement of the Brewster-angle window. An InGaAs photodiode (10 mm × 10 mm) placed at an angle of 45° measures the laser power with/without the window placed in front of the photodiode. In this arrangement, the photodiode position was fixed and the cryogenic radiometer was movable with respect to the laser beam (see Figure 4.7). When the Brewster-window is placed in front of the photodiode, the laser beam undergoes a vertical shift (approximately 1.2 mm), which must be compensated. The ratio of both measurements determines the transmittance of the window. An aperture of 5 mm diameter was placed in front of the diode in order to match the field-of-view of the photodiode with that of the cryogenic radiometer.

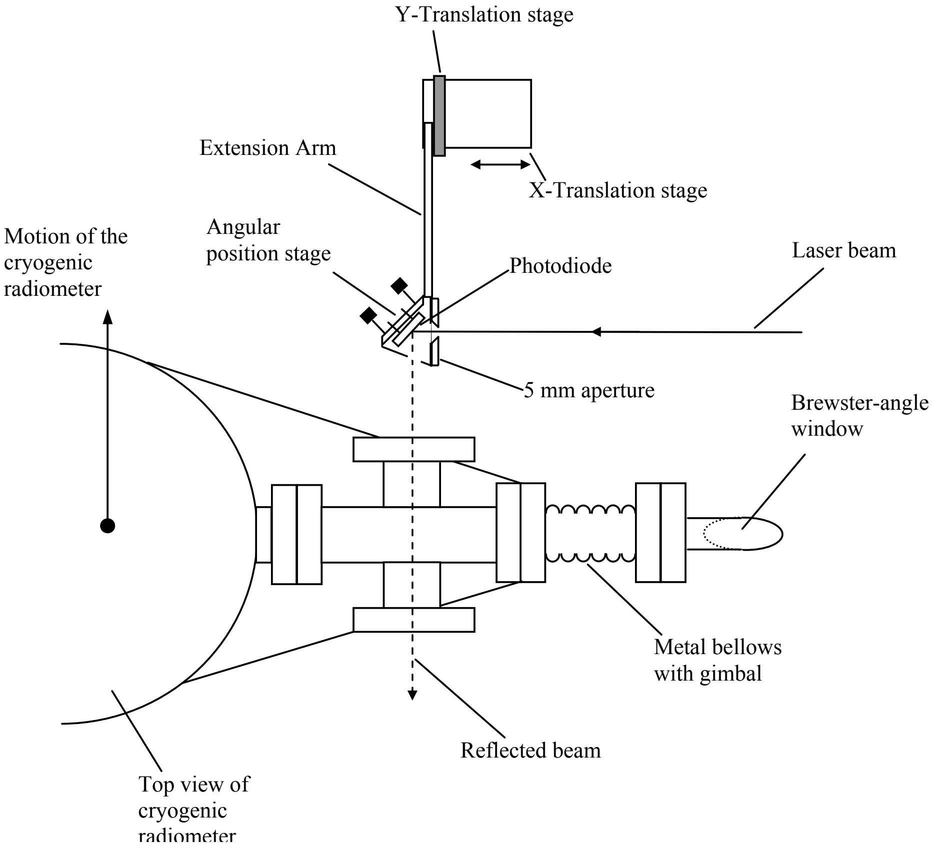

Figure 4.7 Experimental arrangement for transmittance measurement of the Brewster-window of the cryogenic radiometer (view from top). The ratio of the measurements of the radiant power of a laser beam with and without the Brewster-window determines the transmittance of the window.

Figure 4.8 shows the window transmittance measured in the spectral range between 1260 nm and 1360 nm and between 1460 nm and 1620 nm in steps of 10 nm. A maximum transmittance value of 0.9990 and 0.9992 was measured at 1300 nm and 1550 nm, respectively. However, from 1320 nm to 1360 nm the transmittance value drops down to 0.9965, and increases again from 0.9966 to 0.9990 between 1440 nm and 1500 nm, respectively. For the rest of the wavelengths the value of the window transmittance remains practically constant. The fact that the transmittance value goes down and up between 1320 nm and 1500 nm indicates that the Brewster-window contains an absorption due to water molecules content in the Quartz, since the window is made of S1-UV Schlieren grade fused silica where this kind of absorption is typically present [35]. To verify these measurements, the window was dismounted from the cryogenic radiometer and measured with a commercial instrument (Spectrophotometer Cary 5E) in the Spectrometry working group of the PTB, see Figure 4.9. Here, the whole spectral range (1260 nm – 1620 nm) was covered with the Spectrophotometer, where a minimum transmission value of 95.5% at 1382 nm was observed.

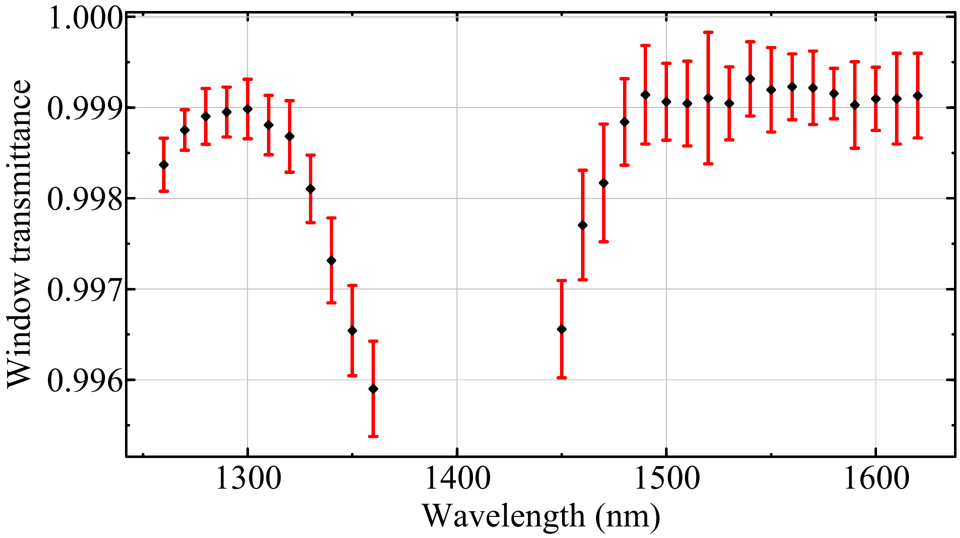

Figure 4.8 Measurement of the window transmittance of the cryogenic radiometer. Window material: S1-UV Schlieren grade fused silica.

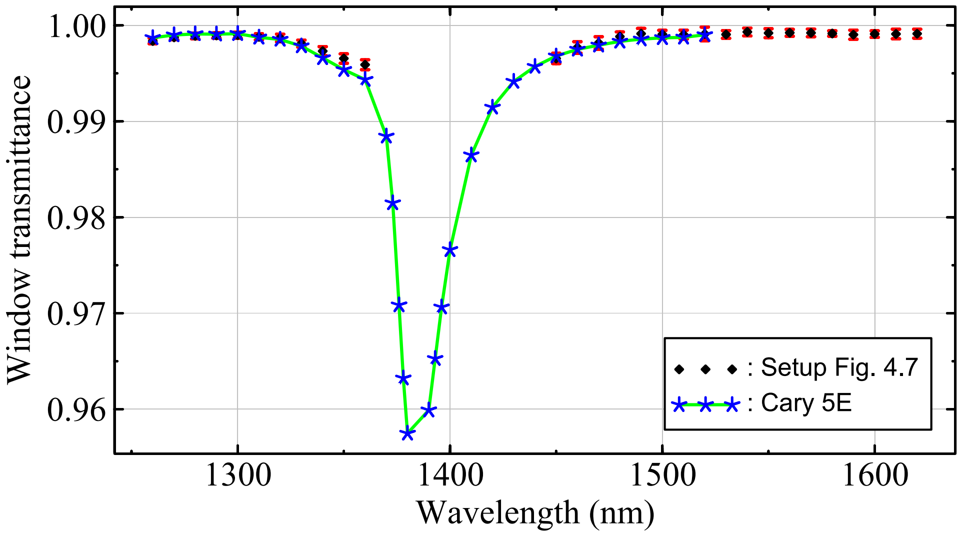

Figure 4.9 Measurement of the window transmittance over the whole spectral wavelength range, 1240 nm – 1620 nm, carried out with a commercial spectrophotometer (Cary 5E).

5 Measurement methods and setups

5.1 Method and setup for the measurement of the spectral responsivity of the trap detectors

According to equation (2.12) (see section 2.1) the responsivity of a photodiode or a trap detector can be obtained by measuring the photocurrent generated by the detector I_{ph} and the incident optical power Φ. In this work, in order to archive the lowest uncertainty, the spectral responsivity $S_{\mathrm{trap}}(\lambda)$ of the trap detectors was determined by comparing the optical power measured by the cryogenic radiometer and the photocurrent generated by the trap detector irradiated with the same optical power. So, the ratio of both measurements gives the detector responsivity,

$$S_{\mathrm{trap}}(\lambda) = \frac{I_{\mathrm{ph}}}{\Phi(\lambda)} = \frac{I_{\mathrm{ph}}}{\Delta P \cdot 1/\tau(\lambda) \cdot 1/\alpha(\lambda)}. \tag{5.1}$$

To achieve the maximum level of accuracy in the measurement of the optical radiation power with the cryogenic radiometer, the laser beam used should satisfy the following conditions:

1) polarization ratio of at least 10000 to 1, and
2) diameter ≤ 2mm (at $1/e^2$), to ensure that more than 99.99% of the radiation beam falls within the 5 mm defining aperture placed front of the radiometer cavity (see Figure 5.3).

Figure 5.1 shows a schematic diagram of the experimental setup used to measure the responsivity of the trap detectors. As the radiation source, two tunable diode lasers were used, whose wavelength can be adjusted from 1260 nm to 1360 nm and from 1460 nm to 1620 nm, respectively. These lasers provide a beam free from mode-hops in the full wavelength range and an optical power stability of ± 0.2 % within one hour. The laser beam is highly collimated by a fiber optic collimator and polarized by two Glan-laser Polarizers (Polarizer 1 and 2) to ensure the polarization ratio required by the cryogenic radiometer and to maximize the transmission of the Brewster-window.

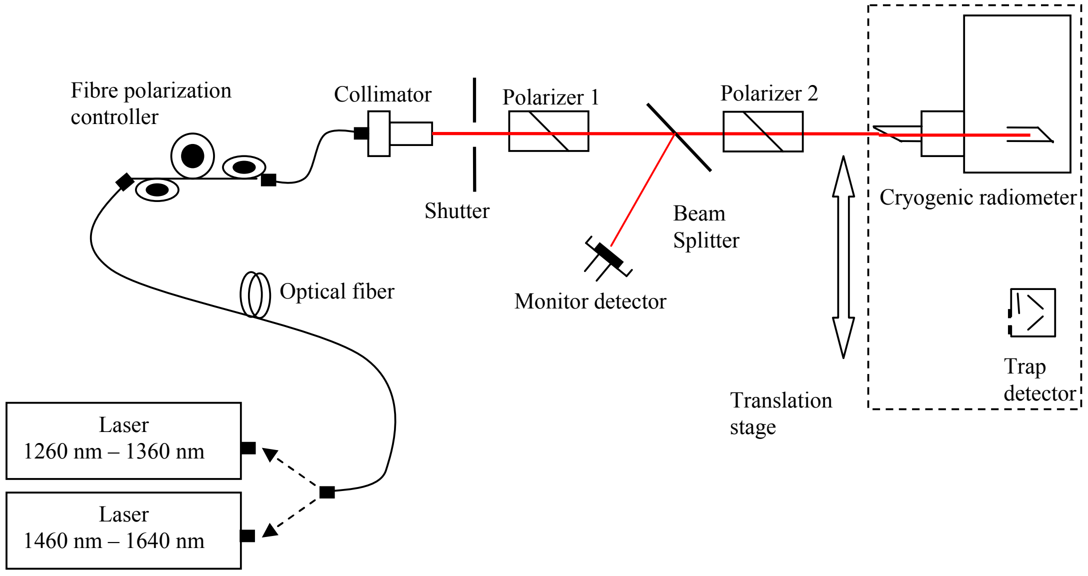

Figure 5.1 Setup for the measurement of the absolute spectral responsivity of the trap detector.

Typically the laser beam is spatially filtered to ensure the propagation just of the TEM_{00} mode [34, 36, 37]. However, in this setup the use of a single mode spatial filtering of the laser beam is not necessary, because the core diameter of the single mode fiber (9 µm) acts as a spatial filter itself. The linear polarization of the laser beam - provided by the tunable laser - is transformed into an elliptical polarization at the fiber optic output; therefore a fiber polarization controller (Thorlabs FPC562) is used to obtain a maximum laser power parallel to the polarization axis of the Polarizer 1. To minimize possible influences on the measurement due to the laser power fluctuation, the beam was monitored by an InGaAs monitor detector. The laser beam power used in the measurement was approx. 400 µW.

To ensure that the diameter of the laser beam used in the measurement satisfies the condition described above, the diameter of the laser beam was measured by a BeamScope at different positions between the cavity plane of the cryogenic radiometer and the Brewster-window. An average diameter of approx. 2.06 ± 0.04 mm at $1/e^2$ was obtained, see Figure 5.2. Furthermore, it must be ensured that the cryogenic radiometer and the trap detector collect the same amount of radiation, so that an aperture of 5 mm diameter was placed in front of the trap detectors, which matches well with the smallest aperture inside the cryogenic radiometer, see Figure 5.3. In addition, the trap detector, together with the aperture, was placed at the same aperture plane as the cryogenic radiometer cavity (see Figure 5.1). Both the cryogenic radiometer and the trap detector were mounted on a translation stage, which moves (horizontally) alternately the cryogenic radiometer and the trap detector into the laser beam. To minimize the temperature influence in the measurement process, the laboratory was highly stabilized at 20.5 ± 0.5°C. Moreover, the temperature of the trap detectors was measured with the temperature sensor (Pt100) incorporated in the housing.

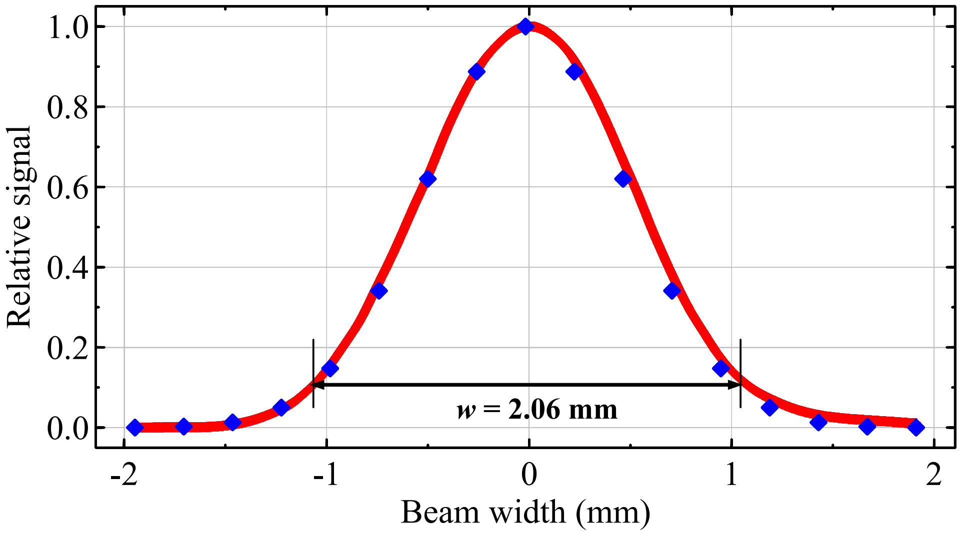

Figure 5.2 Normalized intensity of the laser beam distribution used in the measurement of the spectral responsivity. The curve presents the measurement (solid line) and model (filled diamonds) of the beam profile.

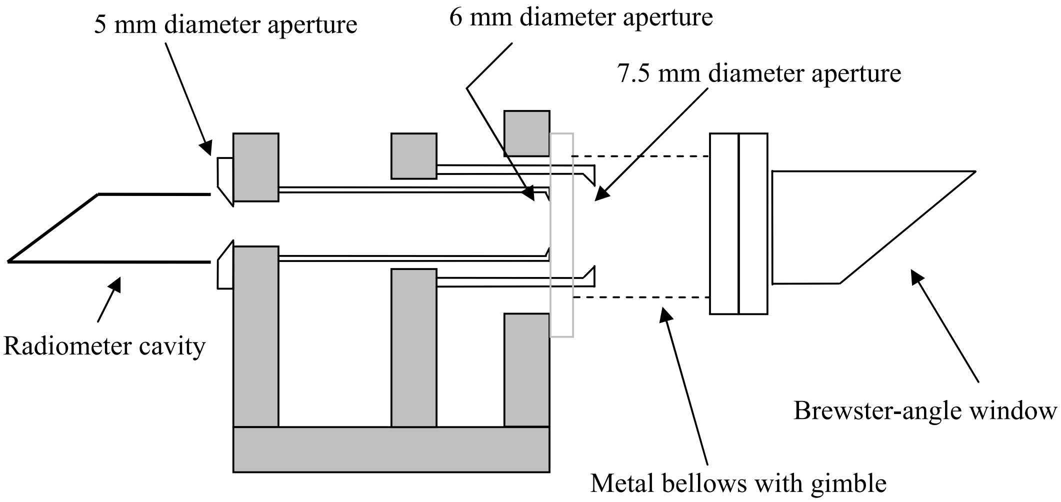

Figure 5.3 Window/baffle arrangement contained in the cryogenic radiometer [38]. This arrangement is used to reduce the possible stray light of the laser beam.

5.2 Method and setup for the measurement of the spectral responsivity of single photodiodes at normal and oblique incidence

The responsivity of a single photodiode was measured using a similar measurement principle as the one described in section 5.1. However, in this case the aim is the measurement of the responsivity of the photodiodes at normal and oblique incidence with polarized light, specifically at s- and p-polarization states. Therefore the photodiode responsivity was obtained by comparing the measurements carried out by the photodiode under test and an InGaAs-trap detector which is not sensible to the polarization state of the light [27]. In this case the trap detector acts as a standard which is calibrated previously directly against the cryogenic radiometer [39], see section 5.1.

Figure 5.4 shows the experimental setup used for the measurement of the photodiode responsivity at oblique incidence. Here the test photodiode is placed on a rotary stage which allows measuring the photodiode responsivity at several angles. The collimated laser beam irradiates a 2 mm diameter circular aperture which, through a 200 mm focal length lens, is 1:1 imaged on the active area of the photodiode. A rotatable Glan-laser polarizer is used to polarize the laser beam at s- and p-polarization. To obtain a maximum power ratio of the laser beam provided by the tunable diode lasers in the s- and p- polarization, a polarization controller (HP 11896A) is also used. As in Figure 5.1, the laser beam is here also monitored by a monitor detector (Ge detector with stabilized temperature) to minimize possible influences on the measurement due to laser power fluctuations.

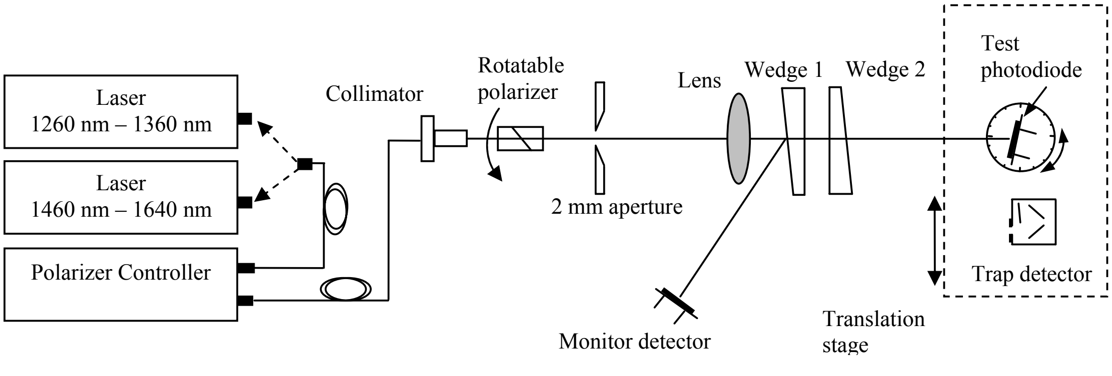

Figure 5.4 Setup used to measure the spectral responsivity of Ge- and InGaAs-photodiodes at normal and oblique incidence.

5.3 Method and setup for the measurement of the spectral reflectance at normal and oblique incidence

The spectral reflectance of the photodiodes was measured by using a reference goniometric setup[4] shown in Figure 5.5. In this setup, a water-cooled tungsten halogen lamp was used as a radiation source. After a spectral selection, the circular polarized beam was made nearly parallel by forming an image (height approx. 7 mm, width approx. 3 mm) of the exit slit of the double monochromator on the surface of the sample. The remaining divergence of the beam was approximately 0.7° in vertical and 1° in horizontal direction, the spectral bandwidth was a little less than 2.5 nm. The regular spectral reflectance was determined for the two different states of linear polarization by comparing the measured flux for the reflection angle Θ_r with the 100 % values measured in the straight-on position when the sample was moved out of the beam. As a detection unit an InGaAs-detector (EOS IGA-050-TE2-H/SEL, diameter of active area: 5 mm) was used, equipped with an integrating gold sphere (Labsphere 4P-GPS-040-IG, diameter: 98.6 mm). Due to mechanical limitations of the set-up, a smallest reflection angle of 7° was accessible.

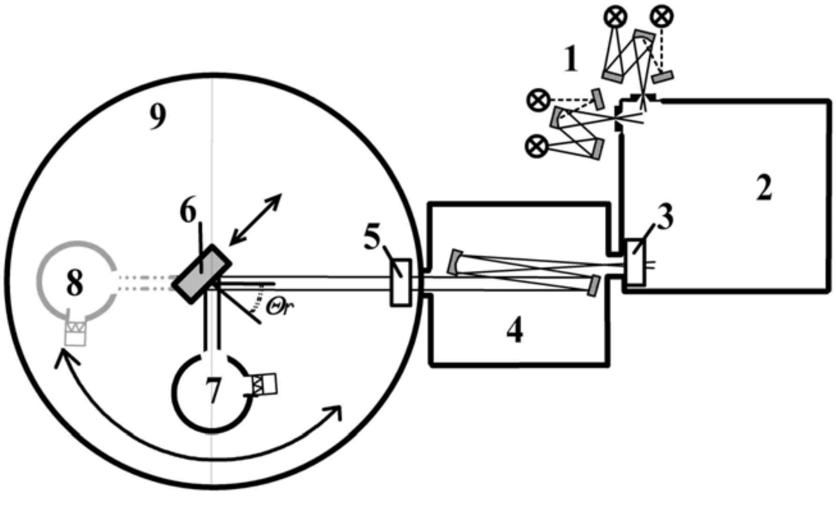

Figure 5.5 Sketch of the goniometric setup for the measurement of the regular reflectance. 1: lamp units, HeNe adjustment laser; 2: double monochromator Jobin Yvon HRD1, $f = 0.6$ m, 3: λ/4-wave plate, 4: beam forming chamber, 5: rotatable polarizer, 6: sample under test, 7: detector unit with integrating sphere in reflection position, 8: detector unit with integrating sphere in 100 % position, 9: sample chamber, $r = 0.66$ m.

---

[4] Reference goniometric setup established in the working group 4.51 "Spectrometry and micro-optical measuring techniques" of the PTB.

5.4 Method and setup for the measurement of the nonlinearity of the photodiode responsivity at high irradiance levels

As mentioned previously, the calibration or measurement of the absolute spectral responsivity of the photodiodes is carried out at one level of optical radiant power, see section 5.1 and 5.2. However, the photodiodes are frequently used for a variety of power levels where their linearity may be overcome. The linearity of a photodiode is limited by a certain dynamic range where its quantum efficiency and responsivity are constant and independent of the incident optical power. To avoid time consuming and costly absolute calibrations at several power levels, nonlinearity measurements covering the intended power level range are carried out for the determination of the corresponding responsivities.

The International Electrotechnical Commission standard IEC 61315 defines the nonlinearity of a detector responsivity used for optical power measurements as the relative difference between the response at an arbitrary optical radiation power and the response at the reference optical radiation power [40]. It should be understand as reference optical power as the optical power level Φ_c used for the detector calibration. So, the expression for the nonlinearity is then given by,

$$NL(\Phi;\Phi_\mathrm{c}) = \frac{S(\Phi) - S(\Phi_\mathrm{c})}{S(\Phi_\mathrm{c})} \tag{5.2}$$

A photodiode can show two types of nonlinearity: nonlinearity due to saturation of the diode and supralinearity or supraresponsivity, see Figure 5.6. The saturation of the photodiode is presented when its responsivity decreases by increasing the incident optical power; see section 6.7.1. Otherwise, when the responsivity of the photodiode increases by increasing the incident optical power, the photodiode presents a supralinearity. According to A. R. Schafer, et. al. [41], the supralinearity of a photodiode is caused by recombination losses due to traps incorporated during the fabrication process. If the photodiode contains many traps, the minority carriers have high probability to be captured and recombined. At very low optical radiation the traps are empty most of the time, because the rate of minority carrier density is so low that the rate at which minority carries are captured is much less that the lifetime of the trapped state. Thus, the number of minority carriers that recombine is proportional to the minority carrier density and the response of the photodiode is in this case linear. At high optical radiation power, the density of carriers increases causing that the traps are occupied most of the time with increasing the optical power level. Thus, the number of minority carriers that recombine is less than the linearity with increasing the optical power. In this case the photodiode is nonlinear.

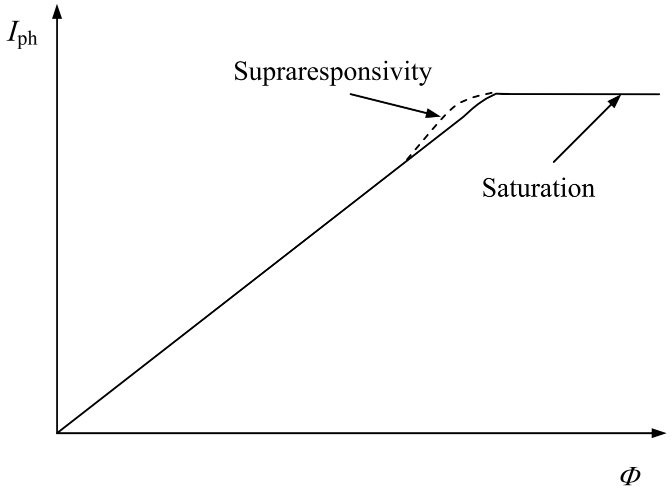

Figure 5.6 Saturation and supraresponsivity of a photodiode.

Supralinearity had been reported for Si-photodiodes in [42, 43]. It has been attributed, following the explanation given above, to a decrease of the recombination losses in the bulk region – behind the junction – for longer wavelengths (≥ 800 nm). Photons absorbed there create electron-hole pairs that have to diffuse toward the depletion region to be collected. Since this is a slow process, the minority carriers have a high probability to be captured. Because at high incident optical power most of the traps are filled, the number of minority carriers that arrive the junction is higher, which increase the photodiode responsivity.

There are many methods to measure the nonlinearity of a photodiode: superposition or flux-addition method [44, 45], AC-DC method or DSR (Differential Spectral Responsivity) [46,20, 47], filter combination method [48], etc. The flux-addition method is the mostly used in most of the NMI's, since it is an absolute method where and no reference detector is needed. This method is based on the non-interferential addition of two optical fluxes. The measurement process is illustrated in Figure 5.7 and it is as follows: In a first step, an arbitrary optical radiant power Φ_a is incident on the photodiode generating a photocurrent I_a. In a second step, the photodiode is irradiated with a second optical power Φ_b, whose level is approximately the same as Φ_a ($\Phi_a \cong \Phi_b$), which generates a photocurrent I_b. In a third step, both optical power

Φ_{a+b} incident simultaneously on the photodiode, generating a photocurrent I_{a+b}. If the generated photocurrent $I_{a+b} = I_a + I_b$, the photodiode responsivity is linear between $I_{a \text{ or } b}$ and I_{a+b}, otherwise the photodiode is nonlinear. Thus, the "local" nonlinearity of the photodiode responsivity NL_1 ($I_{a \text{ or } b}$; I_{ab}) is calculated by

$$NL_1(I_a; I_{a+b}) = \frac{I_{a+b}}{I_a + I_b} - 1 . \tag{5.3}$$

This process is repeated by increasing the incident optical power in steps of $\Phi = 2^n \cdot \Phi_a$ until the whole optical power range wished or limited by the radiation source is covered. Thus, the total nonlinearity NL_{total} of the photodiode responsivity is obtained by summing all local nonlinearities. That is,

$$NL_{total}(I_a; I_x) = \sum_{k=1}^{n} NL_k \tag{5.4}$$

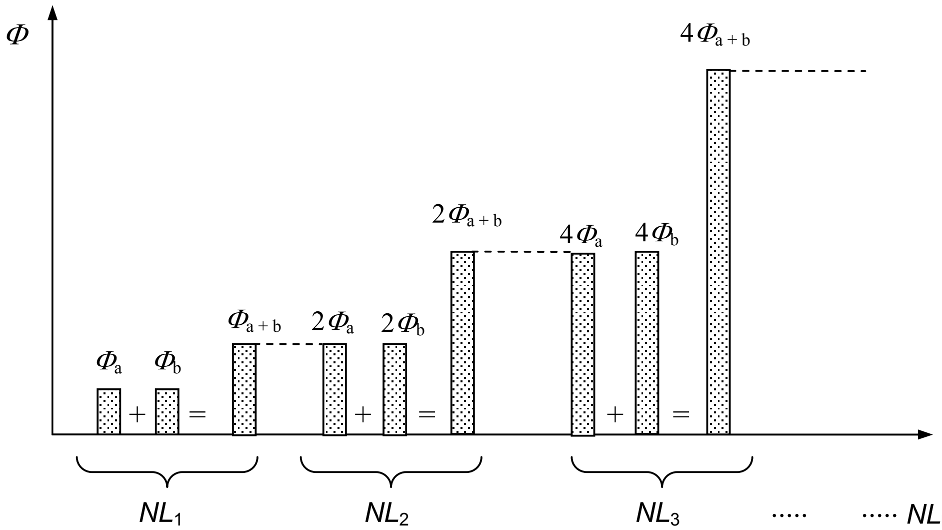

Figure 5.7 Measurement procedure of the flux-addition method to measure the nonlinearity of a photodiode responsivity. First, two similar optical powers Φ_a and Φ_b ($\Phi_a \cong \Phi_b$) are successively incident on the photodiode, from where two photocurrents I_a and I_b are generated, respectively. Second, both optical powers Φ_a and Φ_b irradiate the photodiode at the same time which generates a photocurrent I_{a+b}. The photodiode responsivity is linear if $I_{a+b} = I_a + I_b$, otherwise it is nonlinear.

The setup used in this work for the measurement of the nonlinearity of the photodiode responsivity based on the flux-addition method is shown in Figure 5.8 . The two optical powers Φ_a and Φ_b needed in this method are generated by dividing a laser beam with a 1 × 2 fiber optic coupler (50/50), which later are joined with a second 1 × 2 fiber optic coupler (50/50). This configuration form a system like a Mach-Zehnder interferometer, however, to avoid interference of the two beams, a fiber of ≈ 100 m length was added in one of the arms and the frequency jitter of the laser source was reduced with an internal coherence control. The measurement process is carried out by opening and closing the shutters 1 and 2 sequentially (see Figure 5.7); that is, shutter 1 open and shutter 2 closed → Φ_a, shutter 1 closed and shutter 1 open → Φ_b and both shutters open generates Φ_{a+b}. The fine adjustment of the optical power level $\Phi_a \cong \Phi_b$ is carried out with the attenuators 2 and 3. The attenuator 1 is used to adjust the optical power level (in steps of 3dB) of each measurement step.

Although the flux-addition method is a reference or absolute method used commonly for the measurement of the nonlinearity of the photodiode responsivity, the measurement process may be slow when several steps are required to cover a large optical power range. Furthermore, because of the number of components required in the measurement setup, the optical power losses are considerable high; e.g. the setup in Figure 5.8 presents an insertion loss, generated by the fiber optic connectors, attenuators, etc. of ≈ 8 dB. Thus, in this work others alternatives, for example the DSR-method, were tested.

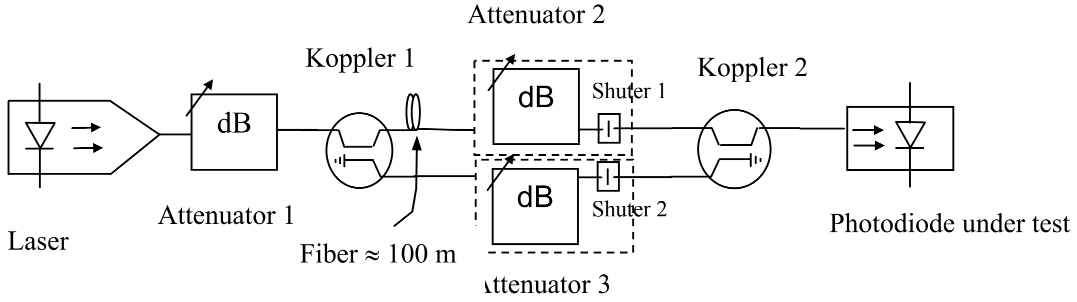

Figure 5.8 Setup used for the measurement of the nonlinearity of photodiodes responsivity by using the flux-addition method.

The DSR method has been successfully applied to measure the nonlinearity at high irradiance levels on solar cells [49]. The basic principle of this method is shown in Figure 5.9. Two optical radiations irradiate the photodiode, a steady-state radiation Φ_{bias} and a modulated radiation with constant amplitude $\Delta\Phi_{\mathrm{mod}}(\lambda)$. By using Lock-in technique, the change of the modulated signal $\Delta\Phi_{\mathrm{mod}}(\lambda)$ depending on Φ_{bias} (d.c. background signal) can be easily detected. In this case Φ_{bias} may be up to 10^6 larger than the modulated signal $\Delta\Phi_{\mathrm{mod}}(\lambda)$. The ratio between the photocurrent $\Delta I_{\mathrm{ph,mod}}$, read e.g. by a Lock-in amplifier, and the modulated signal $\Delta\Phi_{\mathrm{mod}}(\lambda)$ corresponds to the slope of the $I_{\mathrm{bias}}(\Phi,\lambda)$-curve, see Figure 5.9. This slope is the so-called differential spectral responsivity [20] given by

$$\tilde{s}(\Phi_{\mathrm{bias}},\lambda) = \frac{\Delta I_{\mathrm{mod}}(\Phi_{bias},\lambda)}{\Delta\Phi_{\mathrm{mod}}} = \frac{\partial I_{\mathrm{ph}}}{\partial \Phi} \tag{5.5}$$

In general $\tilde{s}$ can be written as: $\tilde{s} = \frac{\partial I_{\mathrm{ph}}}{\partial \Phi}\Big|_{\Phi_{\mathrm{bias}}}$

By knowing the differential spectral responsivity $\tilde{s}$, the responsivity S of a photodiode can be obtained easily by an iterative integration over the photocurrent $I_{\mathrm{bias,x}}$,

$$S(\Phi_{\mathrm{bias}},\lambda) = I_{\mathrm{bias}}(\Phi_{\mathrm{bias}}) \cdot \left[\int_0^{I_{\mathrm{bias,x}}} \frac{dI_{\mathrm{bias}}}{\tilde{s}(I_{\mathrm{bias}})}\right]^{-1} . \tag{5.6}$$

It should be noted that when the photodiode is linear, the responsivity S is equal to the differential responsivity $\tilde{s}$ **.**

Thus, the nonlinerity of the photodiode under test is calculated by normalizing the responsivity $S(\Phi_{\mathrm{bias}},\lambda)$ to a reference responsivity $S(\Phi_{\mathrm{ref}},\lambda)$

$$NL(I_{\mathrm{bias,0}};I_{\mathrm{bias,x}}) = \frac{S(\Phi_{\mathrm{bias}},\lambda)}{S(\Phi_{\mathrm{ref}},\lambda)} - 1 . \tag{5.7}$$

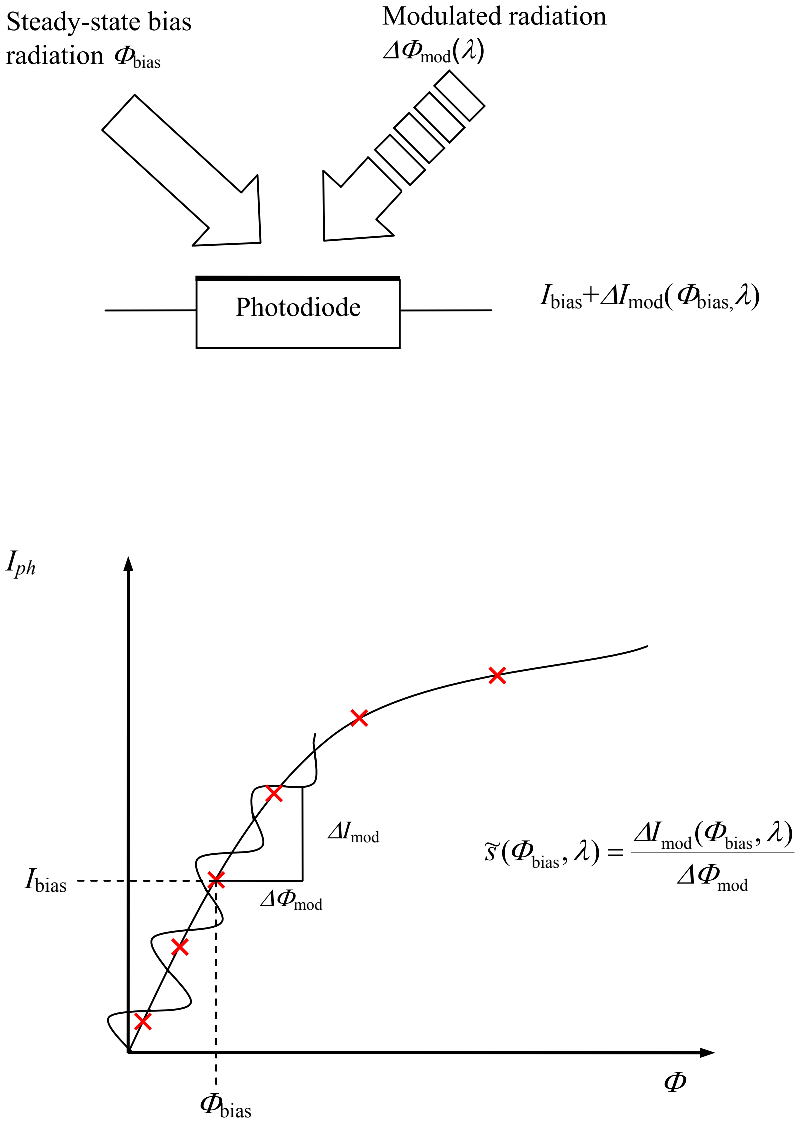

Figure 5.9 Principle of the DSR method for the measurement of the nonlinearity of the photodiodes. Here, the change of an AC-Signal depending of a variable DC- background signal is detected, from where a differential spectral responsivity $\tilde{s}$ is calculated.

Figure 5.10 shows the setup for the measurement of the photodiode nonlinearity by using the DSR method. Here a WDM-coupler is used to join the continuous radiation Φ_{bias} and the modulated radiation Φ_{mod}. As radiation sources two laser diodes, one operated at 980 nm and another one at 1550 nm, were used. Both can be operated in a continuous or modulated mode, so the nonlinearity of the detectors can be measured at 980 nm or 1550 nm depending on the laser chosen as Φ_{bias}. The laser diode operated at 980 nm can reach a maximum optical power level of 300 mW. On the other hand, by using an Erbium-Doped Fiber Amplifier (EDFA) the optical signal of the laser diode at 1550 nm can reach a maximum optical power level of 500 mW. A pre-amplifier is used to convert the photocurrent produced by the photodiode to voltage. The slope of the differential spectral responsivity $\tilde{s}$ at $I_{\mathrm{bias}}(\Phi,\lambda)$ is measured finally by a lock-in amplifier.

In this work another alternative to measure the nonlinearity of the photodiodes at high irradiance levels – the “relative” method – was also tested. It consists of the determination of the ratio between the signal generated by the photodiode under test (DUT) Y_{DUT} and the signal of a standard photodiode Y_{ref}. In this case the linearity of the standard photodiode should be previously known, so that it is operated within its linear range which is generally at low irradiance levels. Thus, the nonlinearity is given by

$$NL = \frac{Y_{DUT}}{Y_{\mathrm{ref}}} - 1 . \tag{5.8}$$

Although this method is not absolute, since it is based on a photodiode whose linearity must be known, the measurement system is easy and economical to implement. Figure 5.11 shows the experimental setup for the nonlinearity measurement based on this method. In this case, a modulated radiation is not required. A 1 × 2 fiber optic splitter with a ratio of approx. 10:90 is used to divide the laser beam. Here, 10 % of the laser beam irradiates the standard photodiode and 90 % irradiates the DUT. In that way, a reference photodiode that presents a linear response, for instance up to 4 mW, allows the measurement of the nonlinearity, without any correction, up to 36 mW. Obviously, here the linearity of the fiber optic splitter must be verified previously. The linearity of the fiber optic splitter used in this work was tested by attenuating the output radiation of the 90 % arm, so that the photodiode under test was kept within the linear range for all optical power levels tested. The linearity of the splitter was tested up to approx. 100 mW where a linearity ≤ 0.03 % was observed.

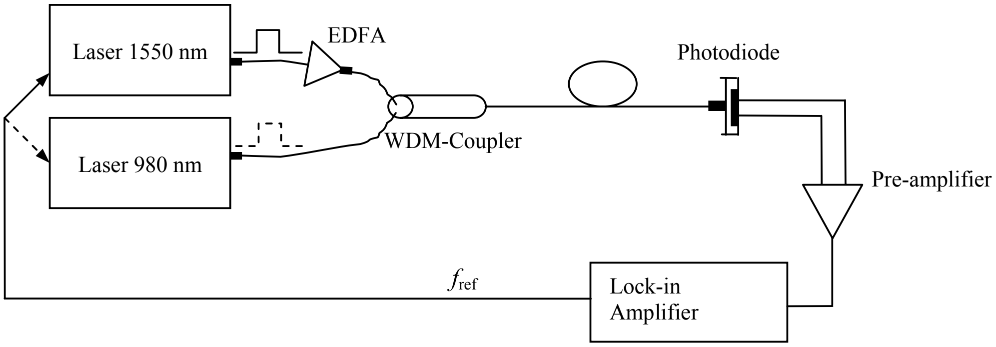

Figure 5.10 Setup for the measurement of the photodiode nonlinearity by using the Differential Spectral Responsivity (DSR) method.

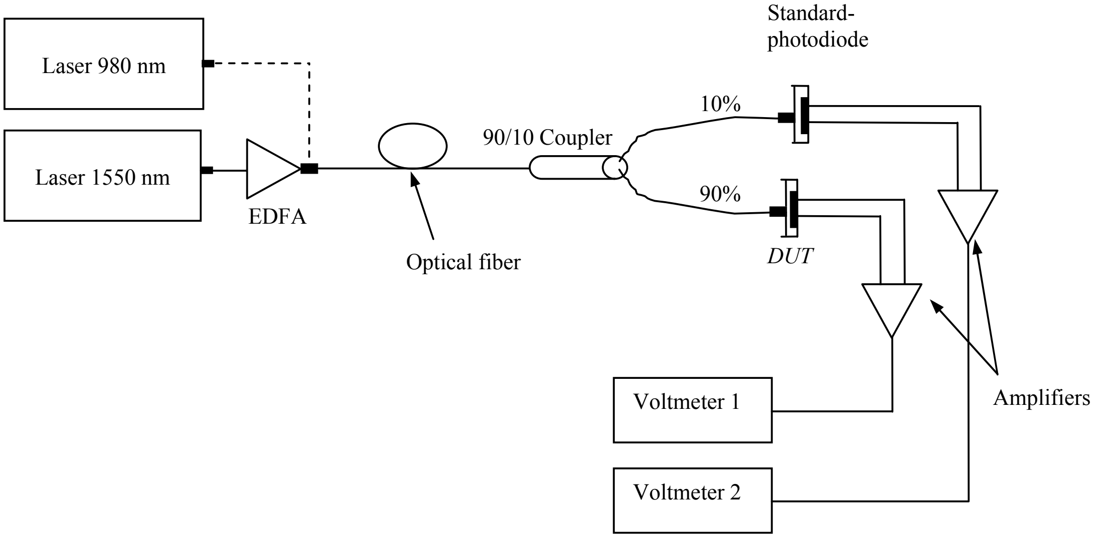

Figure 5.11 Setup for the measurement of the photodiode nonlinearity by using the relative method.

6 Measurement results

6.1 Measurement of the absolute spectral responsivity of the trap detectors and single photodiodes

As mentioned previously, the measurement of the absolute spectral responsivity of the Ge- and InGaAs-trap detectors was carried out by direct calibration against the cryogenic radiometer, since in this case the determination of the absolute responsivity of the trap detectors is with the lowest measurement uncertainty. Thus, the setup described in section 5.1 was used for this purpose. Moreover, in order to compare the absolute spectral responsivity of the trap detector with the absolute spectral responsivity of a single photodiode, measured with the setup described in section 5.2, the responsivity of the single photodiode is also included in this section.

Figure 6.1 shows the absolute spectral responsivity of both the Ge-trap detector and the single Ge-photodiode. The measurements were carried out in the spectral range between 1260 nm and 1360 nm and between 1460 nm and 1620 nm. As expected, the spectral responsivity of the Ge-trap detector is higher than the responsivity of the single photodiode over the whole measured spectral range, because the trap configuration reduces practically all reflection losses by means of multiple reflections between the photodiodes. In that way most of the incoming radiation is absorbed, see section 3.2.

The absolute spectral responsivity of Ge-photodiodes increases with increasing wavelength. However, in both cases, a very sharp cut-off peak is observed around 1540 nm, which is caused mainly by the direct band gap transition of Ge. Unfortunately, this sharp peak is located at the wavelength where the so-called third window of optical communications is operated. This makes Ge-detectors in general very sensitive around this wavelength to the change of the measurement conditions, e.g. variation of the temperature. Stock et. al. investigated the temperature dependence of the responsivity of a Ge-photodiode and observed a temperature coefficient of 0.2 % / °C at 1550 nm [11]. This value is very significant, especially for high accuracy measurements.

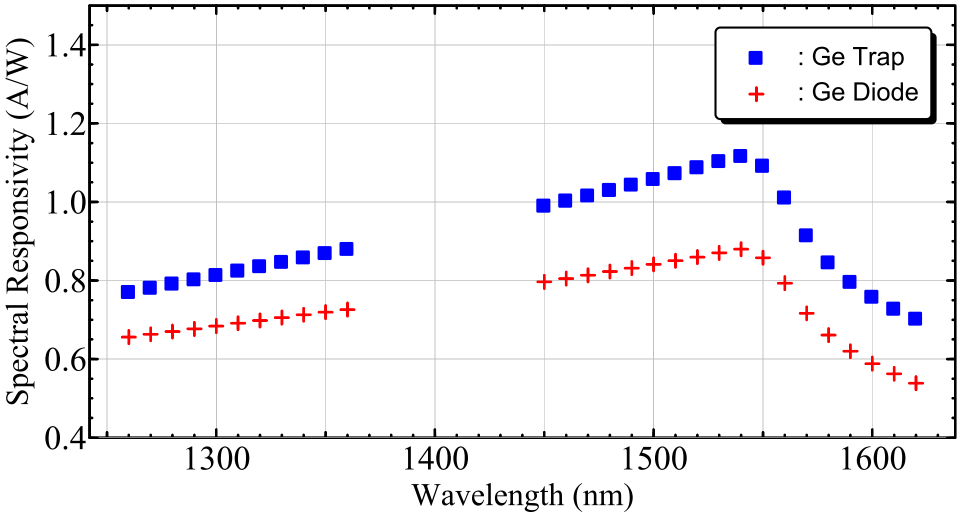

Figure 6.1 Absolute spectral responsivity of a Ge-trap detector and a single Ge-photodiode (measured against the InGaAs-trap) at 20.5 °C.

The absolute spectral responsivity of the InGaAs-trap detector and single photodiode is shown in Figure 6.2. Here, contrary to the Ge-photodiodes, a sharp-peak is not observed within the measured spectral wavelength range. In this case, because of the band gap of InGaAs is about 0.72 eV, the cut-off wavelength is located at about 1700 nm, which is beyond the spectral range investigated in this work.

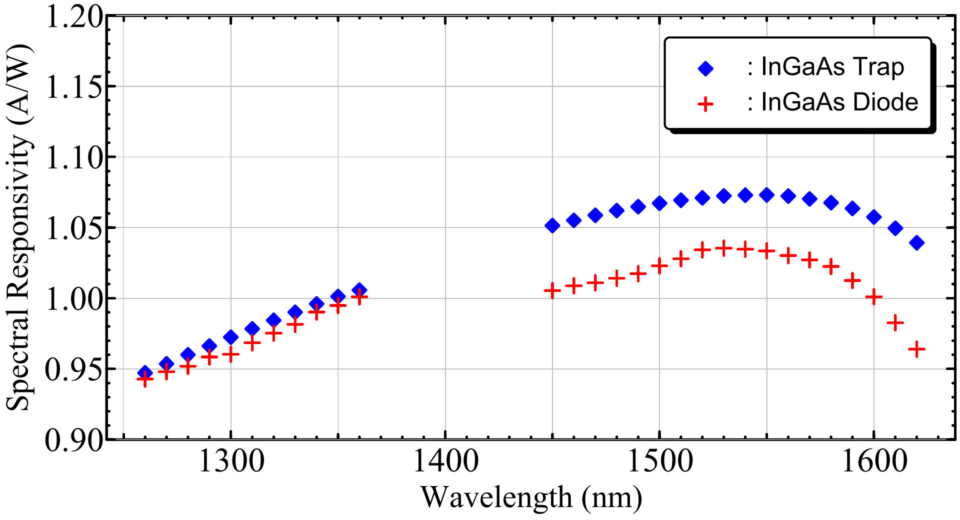

Figure 6.2 Absolute spectral responsivity of an InGaAs-trap detector and a single InGaAs-photodiode (measured against the InGaAs-trap) at 20.5 °C.

Here, also as expected, the responsivity of the InGaAs-trap detector is higher than that of the single photodiode. However for short wavelengths, e.g. between 1260 nm and 1360 nm, the spectral responsivity of the InGaAs-trap and the single photodiode is almost the same, which means that the reflectance of the InGaAs photodiode is lower for short wavelengths than for long wavelengths (see also section 6.3). In Figure 6.2 a dip of the responsivity of the single photodiode between 1450 nm and 1530 nm is also observed, however it disappears practically for the InGaAs-trap detector. It indicates that this dip of the responsivity is caused mainly by the reflectance of the photodiode. In this case one should consider that the InGaAs-photodiode is formed by several layers (InP/InGaAs/InP) and an anti-reflection coating (SiN), which all together form a multilayer assemble whose reflectance depends on the wavelength, see section 6.3 for detailed discussion.

The absolute values of the spectral responsivity of the Ge- and InGaAs-trap detectors are given in Table 6.1.

By knowing the absolute responsivity of the photodiode, the external quantum efficiency can be obtained from equation (2.12) by

$$\eta_{\text{ext}}(\lambda) = \frac{hc}{qn\lambda} S(\lambda). \tag{6.1}$$

Figure 6.3 shows the external quantum efficiency of both, the Ge-trap detector and the single photodiode. Obviously the difference between both efficiencies is only due to the photodiode reflectance. For the case of the trap detector it is valid to assume that the internal and external quantum efficiency are almost equal, $\eta_{\text{ext}} \approx \eta_{\text{int}}$, considering that all photodiodes contained in the trap possess almost the same internal quantum efficiency η_{int} and that the total reflectance of the trap $R \approx 10^{-4}$. So, in Figure 6.3 the external quantum efficiency of the Ge-trap detector increases for long wavelengths until a maximum value of about 0.9 at 1540 nm is reached. For longer wavelengths, it decreases rapidly due to the rapid drop of the absorption coefficient of the Ge semiconductor near the band gap and the finite thickness of the diode. Here, it should be considered that the absorption coefficient and the penetration depth of the radiation in the photodiode depend strongly on the wavelength. Photons with short wavelengths are absorbed in the front region of the diode, and vice versa, see section 2.1. At shorter wavelengths the decrease of the quantum efficiency is due mainly to recombinations

Table 6.1 Values of the absolute spectral responsivity of the Ge- and InGaAs-trap detectors measured with the cryogenic radiometer from 1260 nm to 1360 nm and from 1460 nm to 1620 nm in steps of 10 nm. The uncertainties correspond to a relative combined standard uncertainty (see chapter 7).

	Ge-trap		InGaAs-trap	
Wavelength (nm)	**Responsivity (A/W)**	**Uncertainty $\times 10^5$**	**Responsivity (A/W)**	**Uncertainty $\times 10^5$**
1260	0.76861	18	0.94714	18
1270	0.77929	15	0.95359	14
1280	0.79013	19	0.96000	19
1290	0.80099	17	0.96621	17
1300	0.81194	20	0.97242	20
1310	0.82291	20	0.97832	20
1320	0.83410	23	0.98436	24
1330	0.84523	22	0.99006	22
1340	0.85662	28	0.99596	28
1350	0.86762	29	1.00119	29
1360	0.87807	31	1.00569	31
1460	1.00118	36	1.05510	35
1470	1.01423	38	1.05867	38
1480	1.02817	28	1.06198	28
1490	1.04193	32	1.06476	32
1500	1.05611	25	1.06714	25
1510	1.07108	28	1.06931	28
1520	1.08591	42	1.07097	42
1530	1.10189	24	1.07237	24
1540	1.11492	25	1.07288	24
1550	1.09000	31	1.07305	28
1560	1.00920	27	1.07226	22
1570	0.91282	24	1.07023	24
1580	0.84382	17	1.06755	18
1590	0.79439	28	1.06347	28
1600	0.75652	21	1.05744	21
1610	0.72594	29	1.04951	29
1620	0.70057	28	1.03922	28

occurring at the interface between Ge and the passivation layer. The passivation on Ge photodiodes is not so effective as for the case of Silicon photodiodes, where SiO_2 is used as passivation layer and antireflection coating and with it the recombination centers are strongly reduced. In the case of the Ge photodiode, a nom-native oxide as SiN is typically used as a passivation and antireflection coating which leads to a high density of recombination centers at the front region.

In contrast to the Ge-detectors, the external quantum efficiency of the InGaAs-detectors drops constantly with increasing wavelengths, see Figure 6.4. In the measured spectral range, a maximum value of the external quantum efficiency of about 0.93 was observed at 1260 nm. However, although the external quantum efficiency of the InGaAs-trap detector is higher than of the Ge-trap detector, it does not reach one. Contrary, the external quantum efficiency decreases continuously for longer wavelengths. This behaviour can be attributed exclusively to the InGaAs intrinsic layer of the photodiodes of the trap, since the AR-coating (SiN) and InP-layer are almost free of absorption for the whole wavelength range measured in this work.

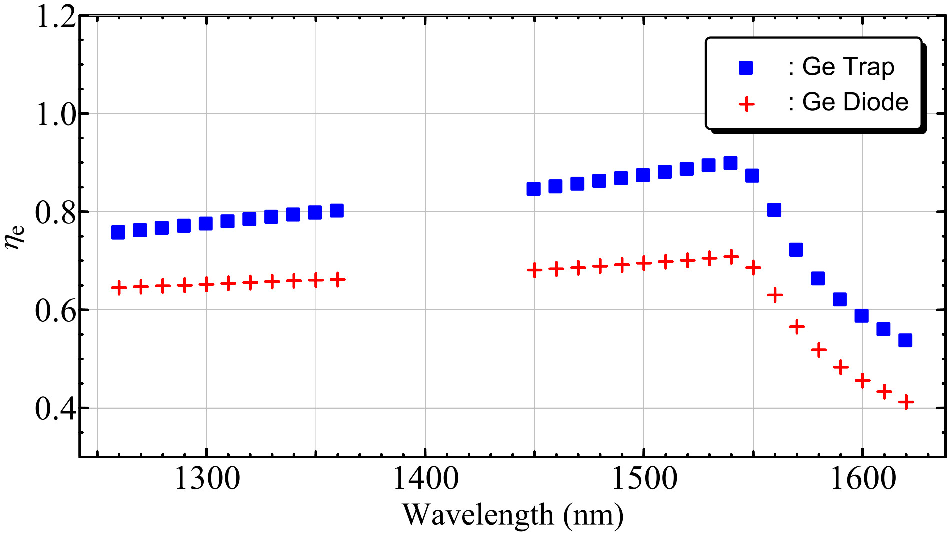

Figure 6.3 External quantum efficiency of the Ge-trap detector and a single photodiode measured at 20.5 °C.

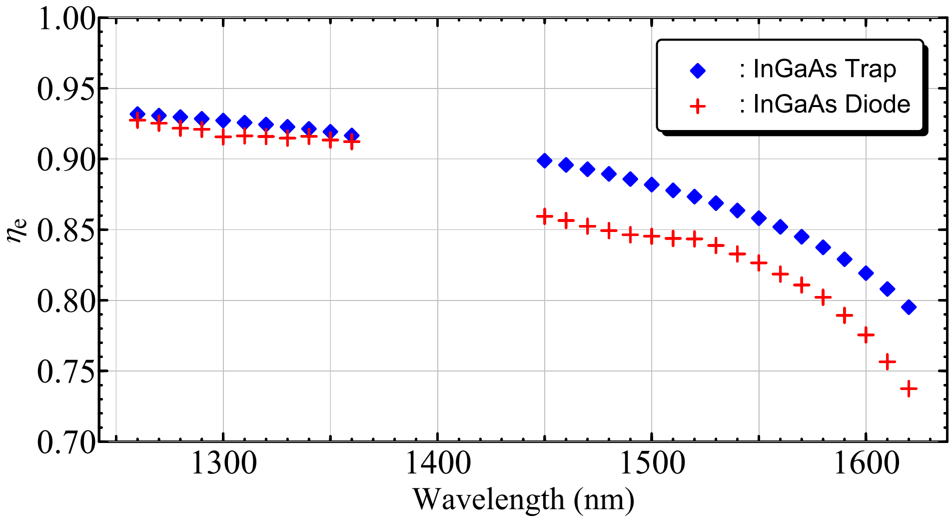

Figure 6.4 External quantum efficiency of the InGaAs trap detector and a single photodiode measured at 20.5 °C.

6.1.1 Comparison with the thermopile

The absolute spectral responsivity of the trap detectors obtained by direct comparison against the cryogenic radiometer gives the possibility to establish a new improved scale for the spectral responsivity of detectors in optical communications. Nevertheless, as part of the PTB responsibilities, it is important to validate such results. The validation of these measurements was carried out by calibrating the trap detectors also against a thermopile (Laser Instrumentation, 14BT) which maintains the actual spectral responsivity scale of detectors for the optical fiber communications at the PTB, see section 1. This scale was compared with the scale of the National Institute of Standard and Technology (NIST), the US National Metrology Institute, [50, 51] resulting in very good agreement.

Figure 6.5 and 6.6 show the absolute spectral responsivity of the Ge- and InGaAs-trap detectors together with the deviations obtained by comparing them with the thermopile and the cryogenic radiometer, respectively. The comparison of both scales shows a maximal deviation of ± 0.15 % for the InGaAs-trap detector and ± 0.30 % for the Ge-trap detector. Considering that the relative standard uncertainty of the scale established with the thermopile is ± 0.30 % (see the traceability chart in section 1), all deviations are well within the combined uncertainty. However, in the case of the Ge-trap detector, the deviations obtained are higher than for the InGaAs-trap, especially in the spectral range between 1460 nm and 1620 nm. Here, one should consider that the dependence of the responsivity of the Ge-trap detector to changes in the ambient temperature is critical in this wavelength spectral range, despite the fact that the temperature effect was corrected.

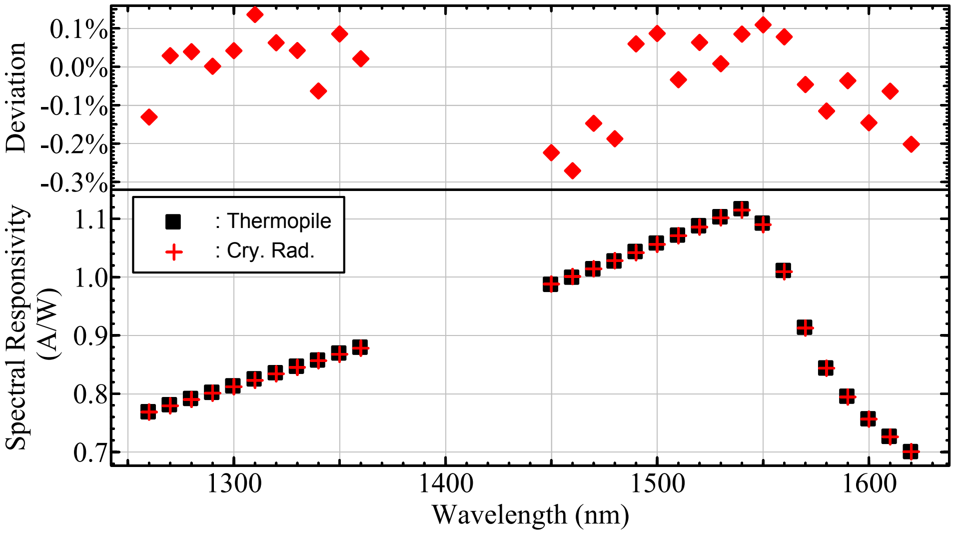

Figure 6.5 Comparison of the absolute spectral responsivity of the Ge-trap detector calibrated against the thermopile (filled squares) and against the cryogenic radiometer (crosses). The deviation (filled diamonds) is also given on the top of the graph.

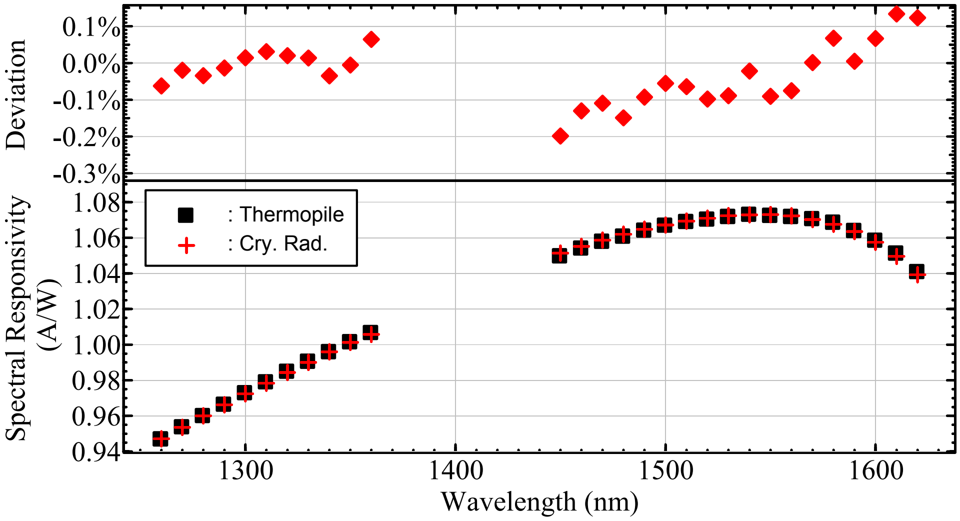

Figure 6.6 Comparison of the absolute spectral responsivity of the InGaAs-trap detector calibrated against the thermopile (filled squares) and against the cryogenic radiometer (crosses). The deviation (filled diamonds) is also given on the top of the graph.

6.2 Model of the spectral responsivity of the single photodiodes and the trap-detectors

The most accurate way to know the spectral responsivity of the photodiodes and trap detectors is, without doubt, the direct measuring of the incident optical power and the resulting photocurrent, as shown in section 5.1 and 5.2. On the other hand, if the spectral responsivity is modelled, the response of the detectors may be predicted for any other condition that may not be accessible due to limitations of the measurement setup, even when it may be not so accurate. The accuracy of the model will depend on the fit level of the parameters to the physical properties of the photodiode.

The spectral responsivity of a photodiode, according to equations (2.11) and (2.12), is given by

$$S(\lambda) = \frac{q}{h \cdot c} \lambda (1 - R) \eta_{\mathrm{int}} \, . \tag{6.2}$$

From equation (6.2) it is clear that the two parameters to be modelled are the reflectance R and the internal quantum efficiency of the photodiode. Both parameters are wavelength dependent, and for the case of the reflectance, it depends also on the incident angle θ_i and polarization of the incident radiation. The internal quantum efficiency has been modelled successfully, e.g. for Si-photodiodes, by J. Geist and E.F. Zalewski [52,53]. On the other hand, in order to model the spectral responsivity of a trap detector, it is necessary to model first the spectral reflectance of the photodiode as a function of the incident angle θ_i and the polarization state p. The process for modelling the spectral reflectance and the responsivity followed in this work is illustrated in Figure 6.7. The models are based on the measurement of the absolute spectral responsivity $S_{\mathrm{mes}}(\lambda,\ \theta_{\mathrm{i}} = 0)$ and the reflectance $R_{\mathrm{mes}}(\lambda,\ \theta_{\mathrm{i}}, p)$. Because the internal quantum efficiency neither depend on the polarization state p nor on the incidence angle θ_i, in principle just one measurement of the photodiode responsivity and reflectance is required. The details of the modelling process and the measurements are given in the following sections.

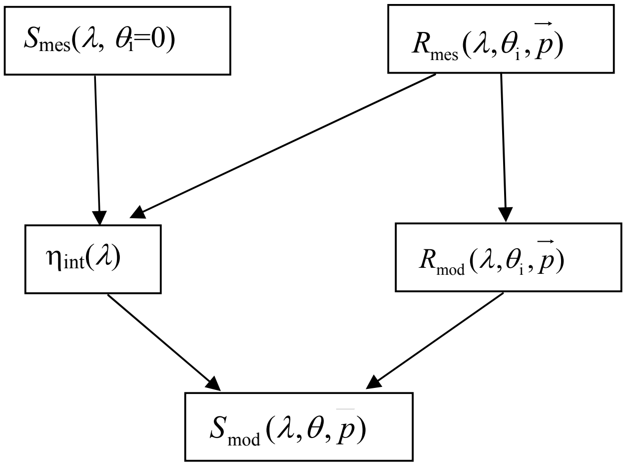

Figure 6.7 Illustrative process for modeling the spectral reflectance and responsivity of the photodiodes.

6.2.1 Optical model of the spectral reflectance of single photodiodes

Photodiodes are devices whose structure can be considered, for the purpose of the optical model of its reflectance, analogous to an optical thin film assembly. The reflectance of such assembly depends basically on their complex index of refraction $N(\lambda) = n(\lambda) - ik(\lambda)$, which is wavelength dependent, and thickness d of the layers. The real part $n(\lambda)$ includes the normal dispersion and the imaginary part, the extinction coefficient $k(\lambda)$, governs the absorption of the light waves propagating inside a medium. For the case of a *p-n* Ge-photodiode, analog to the case of a Si-photodiode reported in [54, 55], an assembly composed of a Ge substrate with a thin cover layer can be considered, see Figure 6.8. However, for the case of the *p-i-n* InGaAs-photodiode a multilayer structure must be taken into account for the optical assembly, see Figure 6.9. Both photodiodes use SiN as the material for the AR-coating and passivation (see section 3.1*)*.

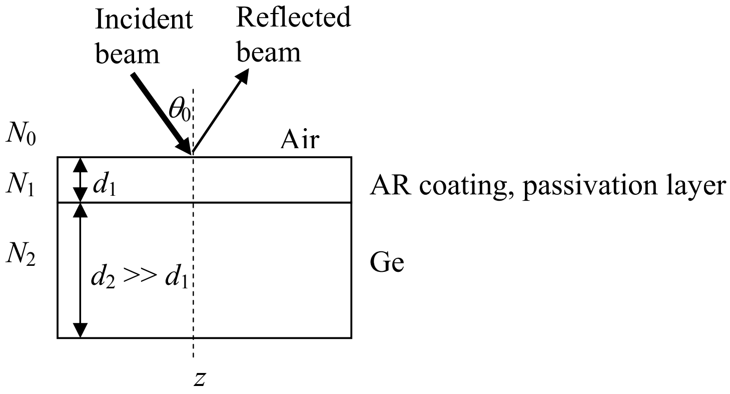

Figure 6.8 Optical assembly of the *p-n* Ge-photodiode. N_i denotes the complex refractive index of the corresponding material.

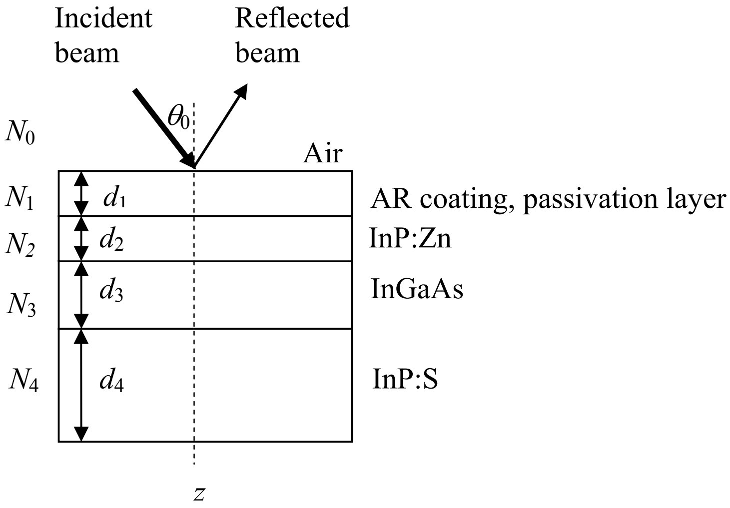

Figure 6.9 Optical assembly of the *p-i-n* InGaAs-photodiode. N_i denotes the complex refractive index of the corresponding material.

There are several methods to model the reflectance of a photodiode with structures such as shown in Figure 6.8 and Figure 6.9. The method commonly used for an optical assembly of three interfaces like the Ge-photodiode is based on thin-film Fresnel formulas described elsewhere [56, 57]. Here, the reflected and transmitted waves are sums of multiple internal reflection at the three interfaces. Although this method is straightforward, the calculations are complicated and can be tedious when the problem includes a certain number of layers as in the case of the InGaAs-photodiode. Thus, in order to generalize the solution for both cases, in this work the matrix approach [18] is used, which takes also advantage of the modern computer calculations.

The matrix approach uses the Maxwell´s equations and the properties of optical impedance and admittance to calculate the reflectance of an assembly of thin films. It is based on the approach to replace the multilayer assembly by a single surface which presents an admittance Y, which is the ratio of the total tangential magnetic H and the total electric E fields and is given by:

$$Y = \frac{H}{E} = \frac{C}{B} \tag{6.3}$$

with:

$$\begin{bmatrix} B \\ C \end{bmatrix} = \left\{ \prod_{\mathrm{r}=1}^{\mathrm{q}} \begin{bmatrix} \cos\delta_{\mathrm{r}} & (i\sin\delta_{\mathrm{r}})/\eta_{\mathrm{r}} \\ i\eta_{\mathrm{r}}\sin\delta_{\mathrm{r}} & \cos\delta_{\mathrm{r}} \end{bmatrix} \right\} \begin{bmatrix} 1 \\ \eta_{\mathrm{m}} \end{bmatrix} \tag{6.4}$$

where $\delta_{\mathrm{r}} = \frac{2\pi}{\lambda} N_{\mathrm{r}} d_{\mathrm{r}} \cos\theta_{\mathrm{r}}$ is the phase shift of the wave front acquired while traveling through the layers, η_{r} is the optical admittance and η_{m} is the substrate admittance. The subindex r denotes the number of the layer and q denotes the number of the layer just in front of the substrate m. The optical admittances for incident angles θ_{r} are given by:

$$\eta_{\mathrm{p_r}} = \frac{N_{\mathrm{r}}}{\cos\theta_{\mathrm{r}}} \text{ (for p-polarization)} \tag{6.5a}$$

$$\eta_{\mathrm{s_r}} = N_{\mathrm{r}} \cos\theta_{\mathrm{r}} \text{ (for s-polarization).} \tag{6.4b}$$

with $N_{\mathrm{r}} = n_{\mathrm{r}} + ik_{\mathrm{r}}$ as the complex refractive index. The incidence angles θ_{r} are calculated by Snell’s law:

$$N_0 \sin\theta_0 = N_{\mathrm{r}} \sin\theta_{\mathrm{r}} = N_{\mathrm{m}} \sin\theta_{\mathrm{m}} . \tag{6.6}$$

The amplitude reflection coefficient ρ and the reflectance $R(\lambda,\theta_0)$ are calculated by:

$$\rho = \frac{\eta_0 - Y}{\eta_0 + Y} \text{ and} \tag{6.7}$$

$$R(\lambda,\theta_0)_{\mathrm{s,p}} = |\rho|^2 \tag{6.8}$$

Note that the number of 2 × 2 matrixes in equation (6.4) depends on the number of layers of the optical assembly. For the Ge-photodiode, only one matrix (for the AR-coating) is required, and germanium is the substrate material, which is considered to be of infinite thickness. For the InGaAs-photodiode, three matrixes are required, corresponding to the three layers of the diode, i.e. the AR-coating, the InP:Zn layer and the InGaAs layer. In this case, InP:S is the substrate material and considered to be of infinite thickness.

So far, the equation (6.7) can be considered as a general solution for the spectral reflectance of both photodiodes at s- and p-polarization and for any incident angle θ. Now the problem is reduced basically in finding the complex refractive indices and thickness of the respective layers. In this work, the complex refractive indices of pure Ge (N_2 in Figure 6.8) and InGaAs (N_3 in Figure 6.9) were taken from the Refs. [58] and [59], respectively. However, for InP:Zn and InP:S it is not possible to use the refractive index of pure InP, because this value is strongly dependent on the dopant and dopant level. For example, in the case of InP doped with Zn (InP:Zn), the value of its refractive index increases, because the material is affected by, e.g., a change in surface conditions, changes of the transition probabilities with photon energies, injection of free carriers and/or change in the bonding and accordingly the material polarizability [66].

There is a huge variety of techniques to determine the refractive index and thickness of a thin-film. These techniques can be classified in two groups: single-wavelength and multi-wavelength. The principal idea of the two methods is to use the experimental measurements of the reflectance or transmittance to determine the optical parameter of the thin-film. The single-wavelength method uses typically the experimental measurement data obtained by spectrophotometric, ellipsometric or interferometric techniques where a laser is mainly used as a radiation source. Although this method is capable to obtain accurate results, the fact of using just a wavelength makes it susceptible to both random and systematic errors in the measurements.

On the other hand, the multi-wavelength method uses the whole data set of the reflectance or transmittance measured over a certain spectral wavelength range. Thus, the sensitivity to the measurement errors is strongly reduced. Here, the determination of the constants of thin-films is based typically on the Kramers-Kronig relation or on curve fitting with the aid of dispersion equations. The Kramers-Kroning method [60, 61] requires the measurement of the reflectance / transmittance for all possible wavelengths, which is not always possible in practice. In contrast, the multi-wavelength curve fitting method does not require that the measured spectral range is wider than the wavelength range of interest. In this case, the experimental data are fitted by adjusting the coefficients of the dispersion equations describing $n(\lambda)$ and $k(\lambda)$ and the thickness of the layer. Dobrowolski et al. [62] showed that a good fit of the coefficients was obtained by using the so-called Inverse Synthesis technique, introduced by himself, which consist basically in minimizing a single-valued merit (discrepancy) function defined in terms of the differences between the measured and calculated values.

So, in this work, the indices of InP:Zn and InP:S as well as of the AR-coating and their corresponding layer thicknesses d_r were obtained by using a multiparameter numerical curve-fitting technique that employs precisely the Inverse Synthesis technique. Although InP:Zn and the InP:S layer may absorb a small amount of the incident radiation, it is negligible in comparison with the absorption present in the InGaAs layer for the spectral range measured in this study. So, for simplicity, we assume that the AR coatings as well as the InP:Zn and the InP:S layer are free of absorptions over the whole spectral range measured. Thus, we approximated the corresponding real refractive index by the first two terms of the Cauchy formula [63]:

$$n_1(\lambda)_{\text{AR-coating}} = x_1 + \frac{x_2}{\lambda^2} \text{ (for the Ge- and the InGaAs-photodiode)} \tag{6.9}$$

$$n_2(\lambda)_{\text{InP:Zn}} = x_3 + \frac{x_4}{\lambda^2} \text{ (for the InGaAs-photodiode)} \tag{6.10}$$

$$n_4(\lambda)_{\text{InP:S}} = x_5 + \frac{x_6}{\lambda^2} \text{ (for the InGaAs-photodiode),} \tag{6.11}$$

where x_1, x_2 and d_1 (for the Ge-photodiode) and x_1, x_2, x_3, x_4, x_5, x_6, d_1, d_2 and d_3 (for the InGaAs-photodiode) are the unknown parameters to be determined. These are found by least-squares fitting, in which the squared differences between the calculated and the measured reflectances are minimized, that is

$$\sum_{\lambda_{\min}}^{\lambda_{\max}} \left[\left[R_{\text{s,meas}}(\lambda,\theta) - R_{\text{s,mod}}(\lambda,\theta) \right]^2 + \left[R_{\text{p,meas}}(\lambda,\theta) - R_{\text{p,mod}}(\lambda,\theta) \right]^2 \right] \rightarrow \text{minimum.} \tag{6.12}$$

Table 6.2 lists the best parameters for both photodiodes found by minimizing equations (6.12) with respect to the data presented in section 6.3. The summation over the squared differences was carried out simultaneously for the spectral range from 1260 nm to 1640 nm in both s- and p-polarization at both incidence angles of 7° and 45°. The refractive indices of the AR-coatings were determined to be 1.87 in case of the Ge-photodiode and to be 1.81 in case of the InGaAs-photodiode and are almost constant over the whole spectral range considered. It should be noted that SiN-films might have different refractive indices, depending on the method of fabrication and the thickness. Thus, the values derived here match well with data from literature [64, 65]. The refractive index obtained for InP:Zn is also close to the reported one in [66] and is shown in Figure 6.10 together with the refractive index for InP:S.

Table 6.2 Best parameters obtained by minimizing the sum of the squared differences between the modeled and the measured reflectance of the Ge- and the InGaAs-photodiode. The summation was carried out simultaneously over the spectral range from 1260 nm to 1640 nm for s- and p-polarization at 7° and 45° incident angles.

Ge		**InGaAs**	
$n_1(\lambda)_{\text{AR-coating}}$	~ 1.87	$n_1(\lambda)_{\text{AR-coating}}$	1.81
	x_1: 1.865		x_1: 1.808
	x_2: 5.369×10^{-4} nm^2		x_2: 2.4×10^{-3} nm^2
$d_{1,\text{AR-coating}}$	115 nm	$d_{1,\text{AR-coating}}$	162 nm
$n_2(\lambda)_{\text{Ge}}$	from [58]	$n_2(\lambda)_{\text{InP:Zn}}$	see Figure 6.10
			x_3: 2.881
			x_4: 1.085×10^{6} nm^2
$d_{2,\text{Ge}}$	infinite	$d_{2,\text{InP:Zn}}$	1235 nm
		$n_3(\lambda)_{\text{InGaAs}}$	from [59]
		$\mathrm{d}_{3,\text{InGaAs}}$	1561 nm
		$n_4(\lambda)_{\text{InP:S}}$	see Figure 6.10
			x_5: 3.277
			x_6: 7.167×10^{5} nm^2
		$d_{4,\text{InP:S}}$	infinite

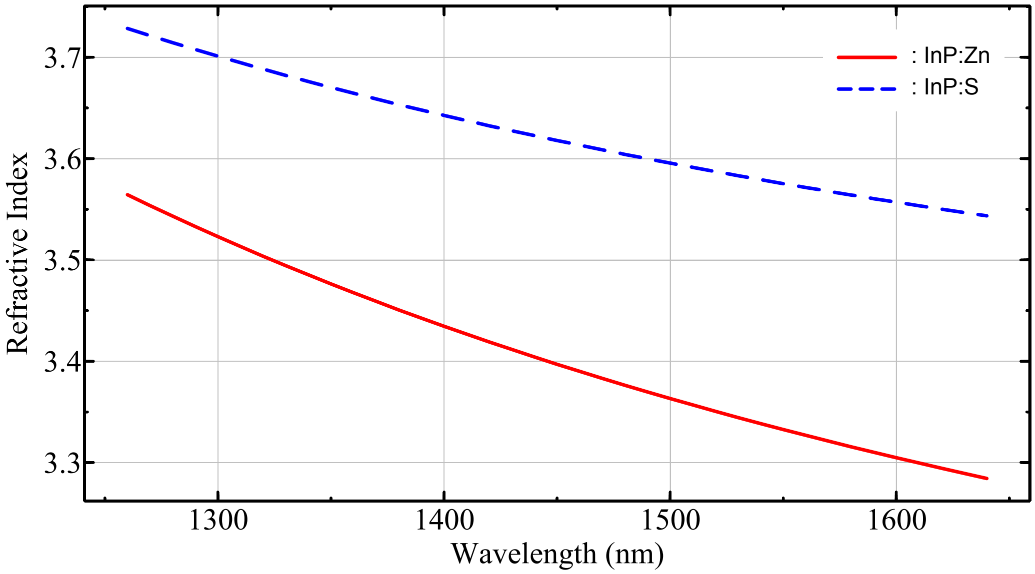

Figure 6.10 Refractive index of InP:Zn and InP:S obtained by least-squares fitting (see text above).

6.3 Spectral reflectance of single photodiodes at normal and oblique incidence

Figure 6.11 and 6.12 show the results of the spectral reflectance measurements for the Ge- and the InGaAs-photodiode, respectively. The reflectance measurements were carried out by using the measurement system described in section 5.3, with s- and p-polarized radiation at 7° and 45° over a spectral range from 1260 nm to 1640 nm. The parameters listed in Table 6.2 were used for the calculation of the reflectance of the Ge- and the InGaAs-photodiode, respectively.

As shown in Figure 6.11, the reflectance of the Ge-photodiode increases smoothly from 12.5 % to 22.5 % for s- and p- polarization at an incidence angle of 7°. In this case the reflectance of the photodiode is nearly independent from the polarization state, since the incidence angle is almost zero. However, at an incidence angle of 45° the photodiode reflectance depends strongly on the polarization state, as expected. For the whole measured spectral range, a maximum reflectance value of 35 % was found at 1640 nm for s-polarization at an incidence angle of 45°. In this case of the Ge-photodiode local minima or maxima are not observed.

Also for the InGaAs-photodiode the reflectance increases with increasing wavelength, see Figure 6.12, however, in this case small oscillations with local minima and maxima are observed. This is due to the interference produced by the multiple interreflections caused by the multilayer structure of the diode, which depends on the thicknesses of the layers and the refractive indices of the materials. The lowest reflectance value of 1 % is measured at 1260 nm for both s- and p- polarization at 7°. The highest reflectance value of 16.2 % was observed at 1640 nm for s-polarization at 45°.

Figure 6.13 and Figure 6.14 show the absolute and relative deviation between the measured and calculated spectral reflectance of the Ge- and InGaAs-photodiode, respectively. For the Ge-photodiode, an absolute deviation of less than 0.5 % and a relative deviation less than 2 % was found in the whole spectral range investigated. The relative expanded uncertainty of the reflectance measurement depends on the absolute reflectance level (see chapter 7); at low reflectance levels the uncertainty is high and vice versa. For the Ge-photodiode, it is between 2.5 % and 4.1 % ($k = 2$). Thus, the deviations between measured and calculated values are within the measurement uncertainty for the whole spectral range investigated.

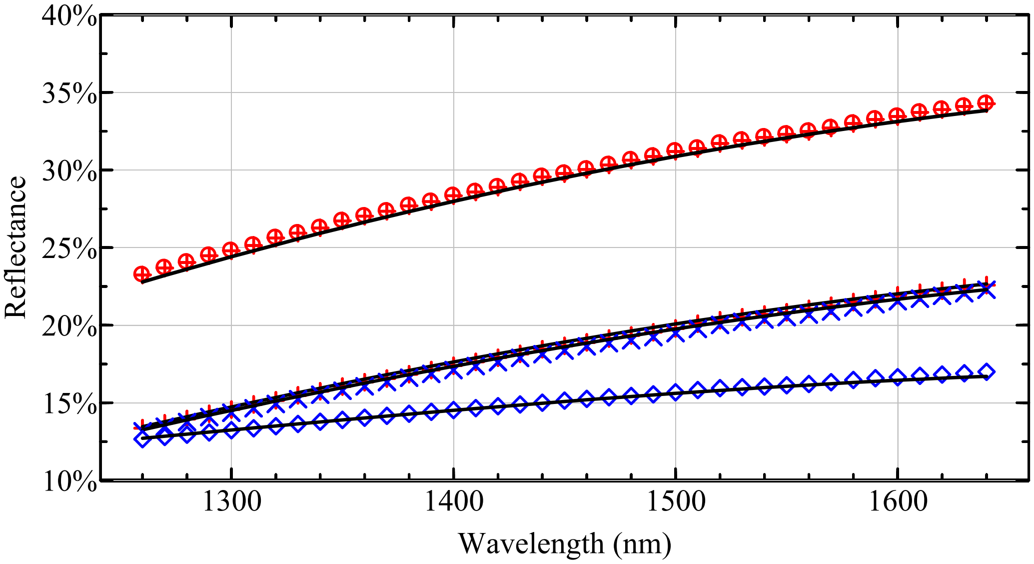

Figure 6.11 Spectral reflectance of the Ge-photodiode measured at 7° and 45° in s- and p-polarization. + and ⊕ → s-polarization at 7° and 45°, respectively. × and ◊ → p-polarization at 7° and 45°, respectively. Continuous lines represent the modeled reflectance values.

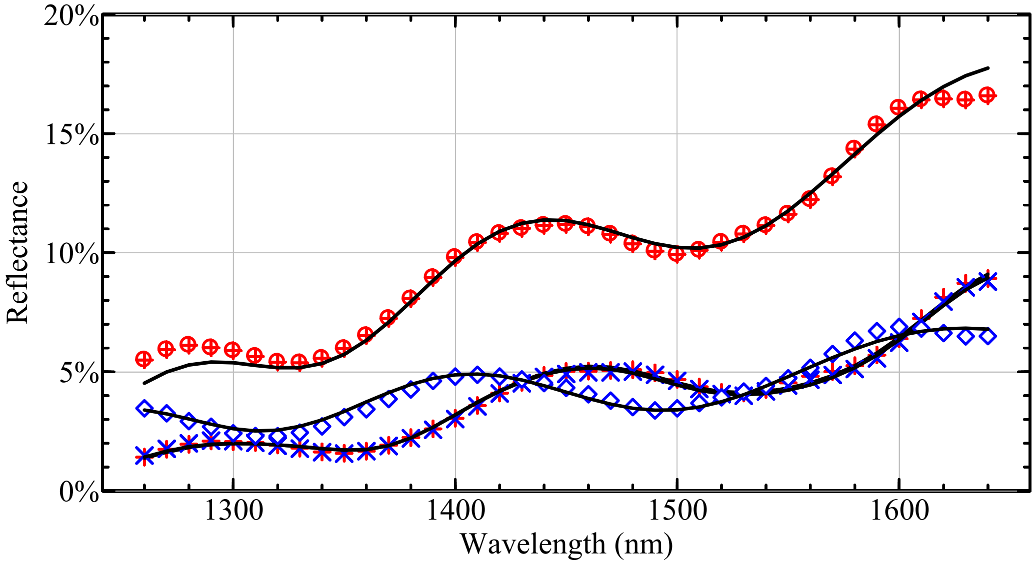

Figure 6.12 Spectral reflectance of the InGaAs-photodiode measured at 7° and 45° in s- and p- polarization. + and ⊕ → s-polarization at 7° and 45°, respectively. × and ◊ → p-polarization at 7° and 45°, respectively. Continuous lines represent the modeled reflectance values.

For the InGaAs-photodiode, the absolute deviations are less than 1% for almost the whole spectral range investigated. The relative deviation between the measured and calculated values are less than 6 % for wavelengths between 1380 nm and 1620 nm and up to 18 % for wavelengths between 1260 nm and 1380 nm and between 1620 nm and 1640 nm, see Figure 6.14. Taking into a count that the relative expanded uncertainty in this case is between 3.7 % and 8 % (k = 2), the deviations between measured and calculated values are within the measurement uncertainty almost for the whole spectral range between 1380 nm and 1620 nm. These higher relative deviations for the InGaAs-photodiode compared to the Ge-photodiode are due to two principal reasons: First, poor fit of the model to the measurement, because of the more complicated structure of the InGaAs-photodiode; second, a higher uncertainty of the reflectance measurement, because of the lower reflectance levels. Both reasons are correlated, because the parameters used in the model were obtained based on the reflectance measurements (see section 6.3). Another possible reason is probably due to the non-homogeneity of the photodiodes responsivity, which takes effect especially at 45° where the beam illuminates more of the active area of the photodiode.

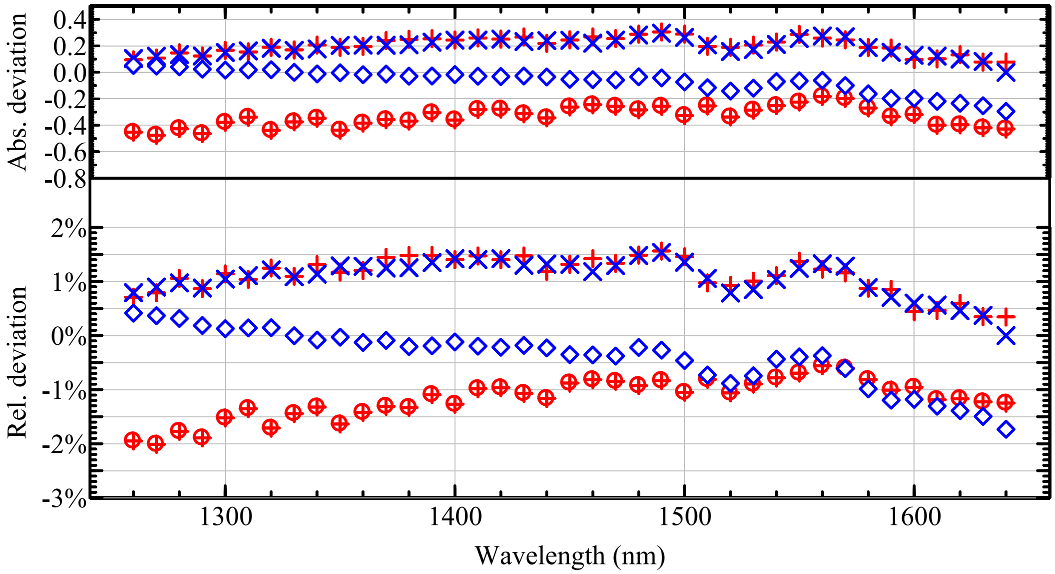

Figure 6.13 Absolute and relative deviations between the calculated and measured values of the reflectance of the Ge-photodiode. + and ⊕ → s-polarization at 7° and 45°, respectively. × and ◊ → p-polarization at 7° and 45°, respectively.

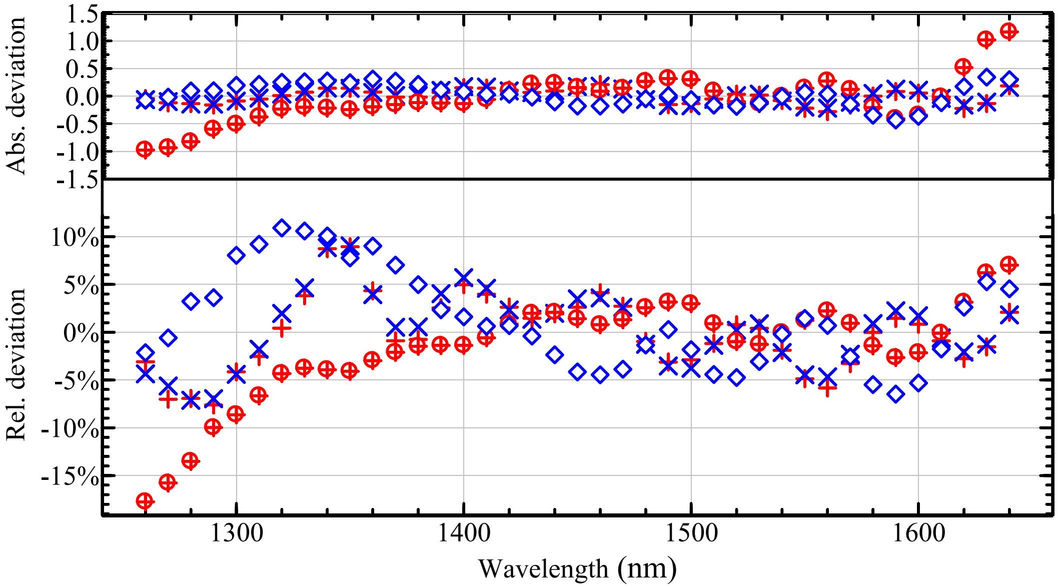

Figure 6.14 Absolute and relative deviations between the calculated and measured values of the reflectance of the InGaAs-photodiode. + and ⊕ → s-polarization at 7° and 45°, respectively. × and ◊ → p-polarization at 7° and 45°, respectively.

6.4 Spectral responsivity of single photodiodes at normal and oblique incidence

The measurement of the spectral responsivity at normal and oblique incidence (45°) was carried out using the measurement setup described in section 5.2. Figure 6.15 and Figure 6.16 show the measured as well as the calculated spectral responsivities of the Ge- and InGaAs-photodiodes at incidence angles of 7° and at 45°, respectively. In both cases the measurements were carried out with s- and p-polarization radiation. For the Ge-photodiode, the shape of the curves is practically the same as the one shown in Figure 6.1 for a single photodiode under normal incidence (see section 6.1). The difference is just a scaling of the curves at oblique incidence (45°) caused by the different spectral reflectance of the photodiode. For s-polarization the reflectance of the photodiode is higher than for p-polarization at the same incidence angle (45°), which reduces the responsivity of the photodiode.

The model of the spectral reflectance of the photodiodes described in section 6.5 allows calculating the spectral responsivity for any incidence angle. That is,

$$S_{\mathrm{mod}}(\lambda,\theta)_{\mathrm{s,p}} = \frac{qn\lambda}{hc}\langle\eta_{\mathrm{int}}(\lambda,\theta)\rangle\left(1 - R_{\mathrm{mod}}(\lambda,\theta)_{s,p}\right), \tag{6.13}$$

where $R_{\mathrm{mod}}(\lambda,\theta)_{\mathrm{s,p}}$ is the calculated spectral reflectance of the photodiode for s- or p-polarization, see section 6.2.1. $\langle\eta_{\mathrm{int}}(\lambda,\theta)\rangle$ is the mean value of the internal quantum efficiencies of both polarization states and incidence angles, where the $\eta_{\mathrm{int}}(\lambda,\theta)$ are calculated from:

$$\eta_{\mathrm{int}}(\lambda,\theta) = \frac{hc}{qn\lambda} S_{\mathrm{meas}}(\lambda,\theta)_{\mathrm{i}} \frac{1}{\left(1 - R_{\mathrm{meas}}(\lambda,\theta)_{\mathrm{i}}\right)} \tag{6.14}$$

where $S_{\mathrm{meas}}(\lambda,\theta)_{\mathrm{i}}$ and $R_{\mathrm{meas}}(\lambda,\theta)_{\mathrm{i}}$ are the measured spectral responsivities and reflectance, respectively. Actually, the internal quantum efficiency of a photodiode does neither depend on the polarization state nor on the incidence angle; however, as shown in Figure 6.17, small variations in the internal quantum efficiency were obtained especially at oblique incidence, most probable due to the non-homogeneity of the photodiodes. Therefore, in equation (6.13) the mean value of all internal quantum efficiencies was used. The standard deviation for the internal quantum efficiency is less than 1.8 % for the Ge-photodiode and less than 0.5 % for the InGaAs-photodiode. Moreover, the internal quantum efficiency for the spectral range not covered by the diode laser sources was interpolated by a 3-degree polynomial fit.

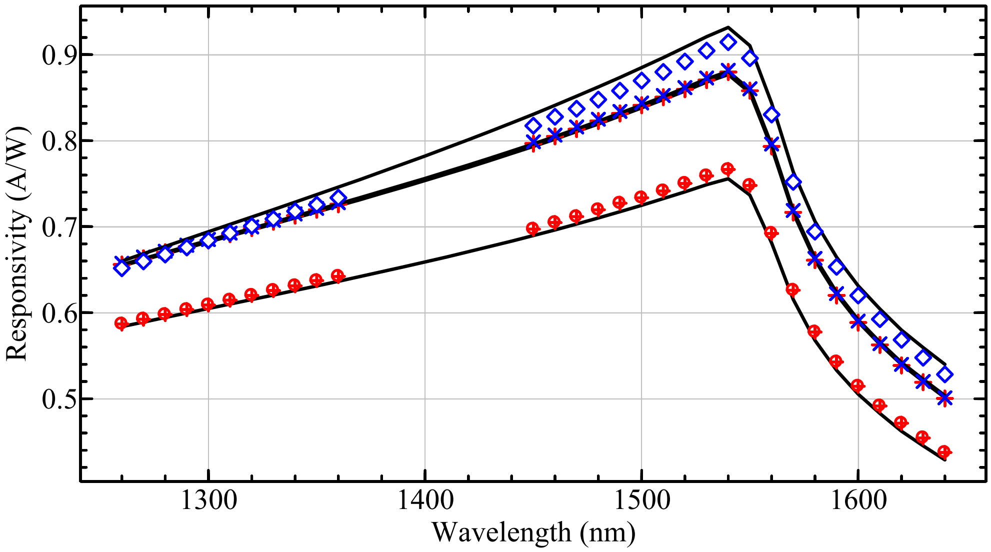

Figure 6.15 Spectral responsivity of the Ge-photodiode measured in s- and p- polarization at 7° and 45° incidence. + and ⊕ → s-polarization at 7° and 45°, respectively. × and ◊ → p-polarization at 7° and 45°, respectively. Continuous lines represent the calculated responsivity values.

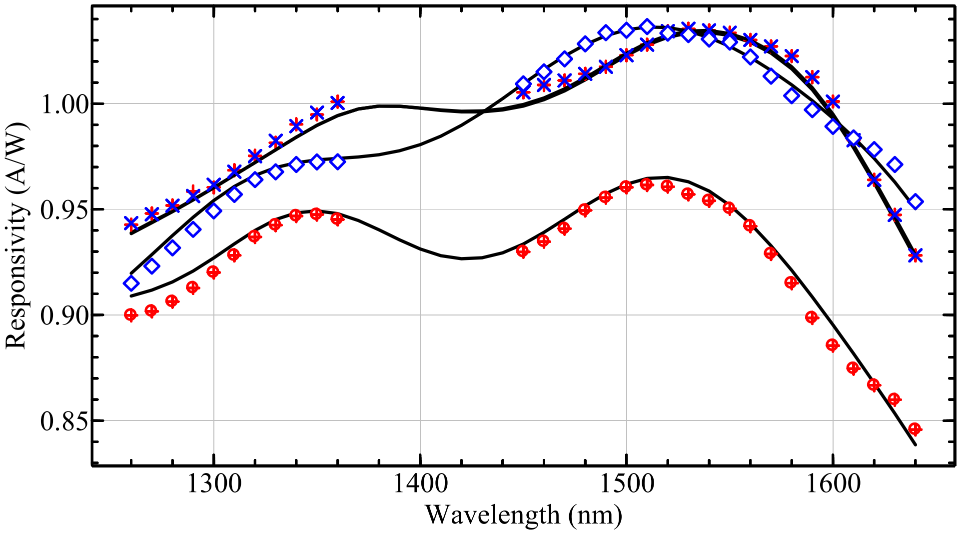

Figure 6.16 Spectral responsivity of the InGaAs-photodiode measured in s- and p-polarization states at 7° and 45° incidence angles. + and ⊕ → s-polarization at 7° and 45°, respectively. × and ◊ → p-polarization at 7° and 45°, respectively. Continuous lines represent the calculated responsivity values.

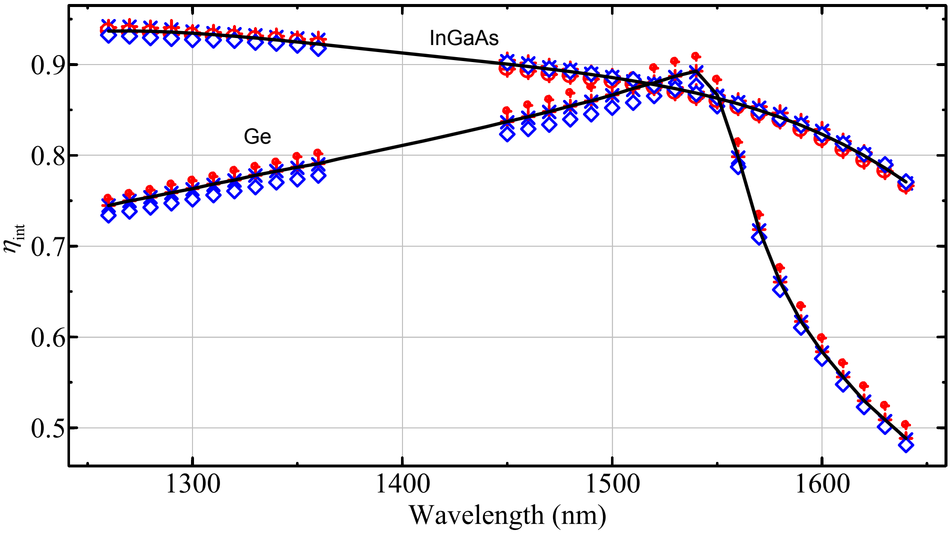

Figure 6.17 Internal quantum efficiency of the Ge- and InGaAs-photodiode for s- and p-polarization at 7° and 45° incidence angles. + and ⊕ → s-polarization at 7° and 45°, respectively. × and ◊ → p-polarization at 7° and 45°, respectively. Continuous lines represent the mean values of the internal quantum efficiencies.

Figure 6.18 and 6.19 show the relative deviation between the calculated and measured spectral responsivities for the Ge- and the InGaAs-photodiode, respectively, in both cases for incident angles of 7° and 45° and for s- and p-polarization. The relative deviations are less than 2.2 % for the Ge- and less than 1.2 % for the InGaAs-photodiode. The deviations are correlated to the absolute reflectance values and to the standard deviation of the internal quantum efficiencies. Therefore the relative deviations for the InGaAs-photodiode are even lower than for the Ge-photodiode, even when the relative deviation between modeled and calculated reflectance is much higher in the case of the InGaAs-photodiode.

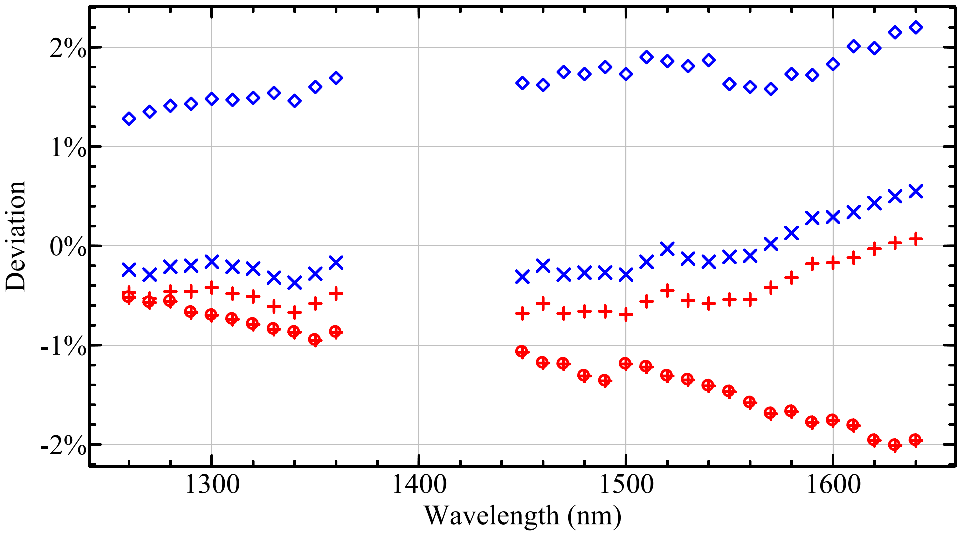

Figure 6.18 Relative deviations between the calculated and measured values of the responsivity of the Ge-photodiode. + and ⊕ → s-polarization at 7° and 45°, respectively. × and ◊ → p-polarization at 7° and 45°, respectively.

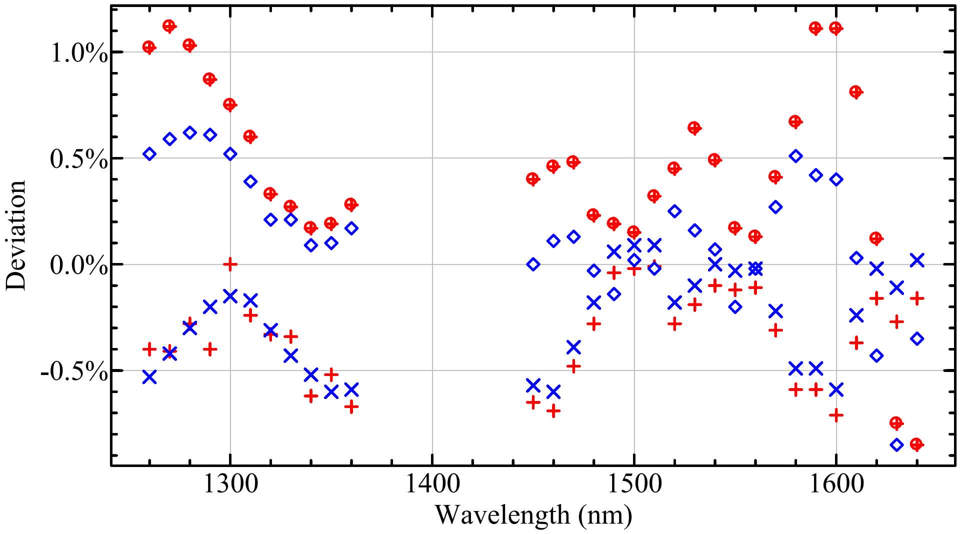

Figure 6.19 Relative deviations between the calculated and measured values of the responsivity of the InGaAs-photodiode. + and ⊕ → s-polarization at 7° and 45°, respectively. × and ◊ → p-polarization at 7° and 45°, respectively.

6.5 Model of the spectral responsivity of Ge- and InGaAs-trap detectors

The spectral reflectance at nearly normal (7°) and oblique incidence (45°) modeled in section 6.2.1 allows to calculate the spectral responsivity of the trap detectors. The spectral responsivity of the trap detectors is calculated by:

$$S(\lambda)_{\mathrm{trap}} = \frac{en\lambda}{hc} \langle \eta_{\mathrm{int}}(\lambda,\theta) \rangle \left[1 - \left(R(\lambda,45°,s)^{2}_{\mathrm{Diode\,1}} R(\lambda,45,p)^{2}_{\mathrm{Diode\,2}} R(\lambda,0)_{\mathrm{Diode\,3}} \right) \right], \tag{6.15}$$

where $R(\lambda,45°,s)^{2}_{\mathrm{Diode\,1}}$ and $R(\lambda,45,p)^{2}_{\mathrm{Diode\,2}}$ are the spectral reflectances of the first and second diode at 45° for s- and p-polarization, respectively. $R(\lambda,0)_{\mathrm{Diode\,3}}$ is the spectral reflectance of the third diode at normal incidence. Assuming that the three photodiodes contained in the trap have the same spectral reflectance, the values of the modeled spectral reflectance shown in Figure 6.15 and Figure 6.16 were used to calculate their corresponding spectral responsivity. Figure 6.18 shows the comparison of the modeled and measured spectral responsivity of the Ge- and InGaAs-trap detector. The relative deviation between modeled and measured responsivity is around 2 % for the Ge-trap detector and around 1 % for the InGaAs-trap detector, respectively. For the case of the Ge-trap detector, the deviation is similar to the reported one in Ref. [19] for Si-trap detectors. The deviations for the responsivity of the InGaAs-trap detector are even smaller.

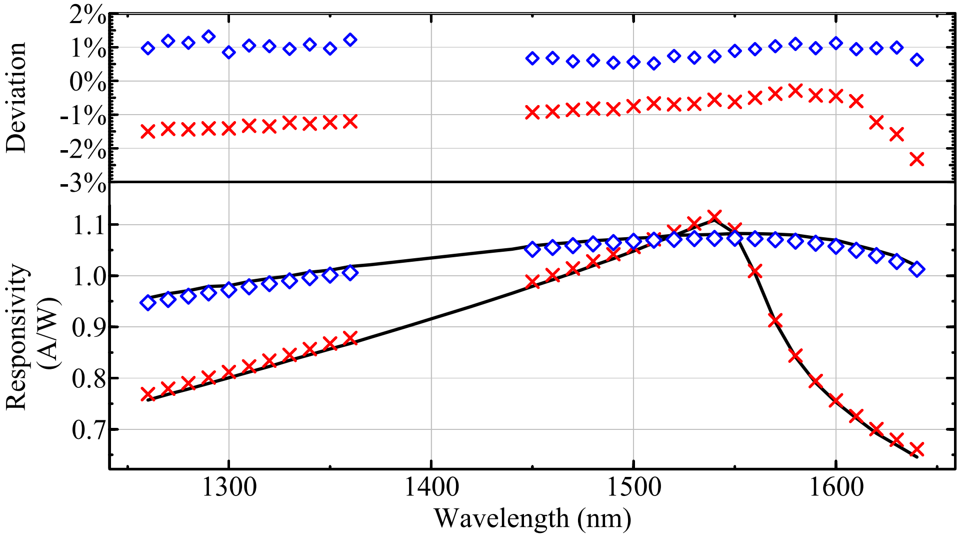

Figure 6.20 Comparison between the measured and calculated spectral responsivity of the Ge- and the InGaAs-trap detector. × and ◊ are the measured values (see Table 6.1 in section 6.1) for Ge- and the InGaAs-trap detector, respectively. Continuous lines represent the calculated values, according to equation (6.15). Deviations between the calculated and measured values are shown at the top of the graph.

6.6 Spatial non-uniformity of the photodiode responsivity

The knowledge of the non-uniformity of the responsivity of a photodiode is very important when it is used as a transfer standard for low uncertainty measurements. An ideal photodiode should have a spatially uniform responsivity. This means, if the photodiode is illuminated with different beam diameters or if the radiation hits different locations on its sensitive area, it should generate the same output signal. However, in the reality the photodiodes present a certain degree of non-uniformity, which depends principally on the fabrication method, size and material of its sensitive area. Moreover, the determination of the photodiode non-uniformity is also sensible to the wavelength, size and homogeneity of the beam used in the measurement.

In this work, the measurements of the non-uniformity of the responsivity of the Ge- and InGaAs-trap and single photodiode were carried out, in essence, by using the setup for the measurement of the responsivity of the photodiode described in section 5.2. However, a couple of modifications in the setup were made. A Y-axis translation stage was added, the aperture of 2 mm was substituted by an aperture of 1 mm and the polarizer was removed. Thus, the relative local responsivity of all photodiodes investigated was mapped with a laser beam spot size of 1 mm ($1/e^2$) in diameter at 0.5 mm intervals in two perpendicular axes. The wavelength of the tunable lasers sources was chosen to be 1310 nm and 1550 nm, respectively. The temperature of the photodiode was held constant at 20.5 ± 0.2°. The photodiodes were placed at normal incidence.

Figure 6.21 (a) and (b) show the non-uniformity of the responsivity of the Ge-photodiode at 1310 nm and 1550 nm, respectively. The results shown are relative to the local responsivity of the center of the sensitive area of the photodiode. In both cases the Ge-photodiode presents a strong non-uniformity at the border of the sensitive area. A sharp peak is observed at 1310 nm, which may be attributed to a local interference produced between the AR-coating and the Ge-semiconductor in this area, since it disappears at 1550 nm. One should consider here also that the absorption and penetration depth of the radiation in the semiconductor depend on the wavelength. For longer wavelengths the penetration depth is higher than for shorter wavelengths. Thus, the change of the non-uniformity of the photodiode responsivity at different wavelengths may be attributed also to surface defects or non-uniformity of the internal structure of the photodiode. For instance, a Ge-photodiode may show inhomogeneity of the distribution of recombination centers at the interface between the Ge-semiconductor and the passivation layer, generated during its fabrication.

On the other hand, the uniformity of the Ge-trap detector is significantly better than that of the Ge-single photodiode, see Figure 6.22 (a) and (b). This is expected, because the effective internal quantum efficiency resulting from a trap detector makes the response almost insensitive to the position of the radiation across the sensitive area of the detector.

Figure 6.23 (a) and (b) show the non-uniformity of the responsivity of the InGaAs-single photodiode at 1310 nm and 1550 nm, respectively. Here, a very good uniformity of the responsivity is observed for the two measured wavelengths. This means that the whole InGaAs-layer, where most of the photons with these wavelengths are absorbed, is very uniform. However, contrary to the Ge-trap case, the InGaAs-trap shows a higher non-uniformity than the InGaAs-single photodiode, see Figure 6.23 in comparison with Figure 6.24. This may be attributed to a low uniformity of the InGaAs-layer of the photodiodes contained in the trap. It should be noted that the InGaAs-photodiodes contained in the trap were fabricated in the 1980's when the preparation methods, for example Vapour Phase Epitaxy, of photodiodes with large surface size were not as optimized as nowadays, which is the case for the InGaAs-single photodiode fabricated recently. Most of the radiation is absorbed on the first photodiode due to the low reflectance, see section 6.3. This means that the sensitive are of the first photodiode is responsible of almost the total non-uniformity of the trap itself.

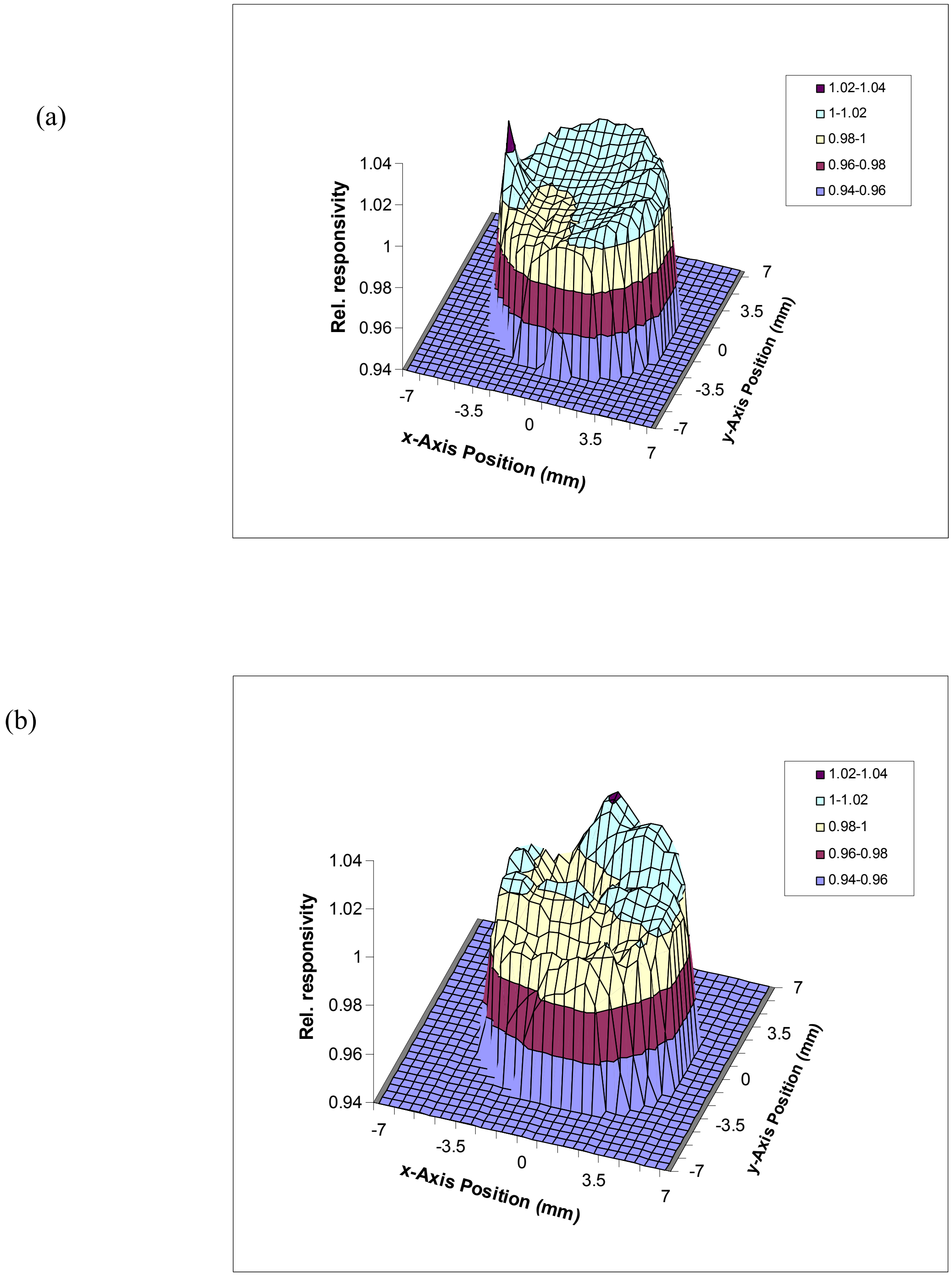

Figure 6.21 Spatial non-uniformity of the responsivity of the Ge-photodiode measured at 20.5° ± 0.2° with a laser beam of wavelength (a) 1310 nm and (b) 1550 nm and a spot size of $\phi = 1$ mm. The scan was carried out in intervals of 0.5 mm in the two perpendicular axes.

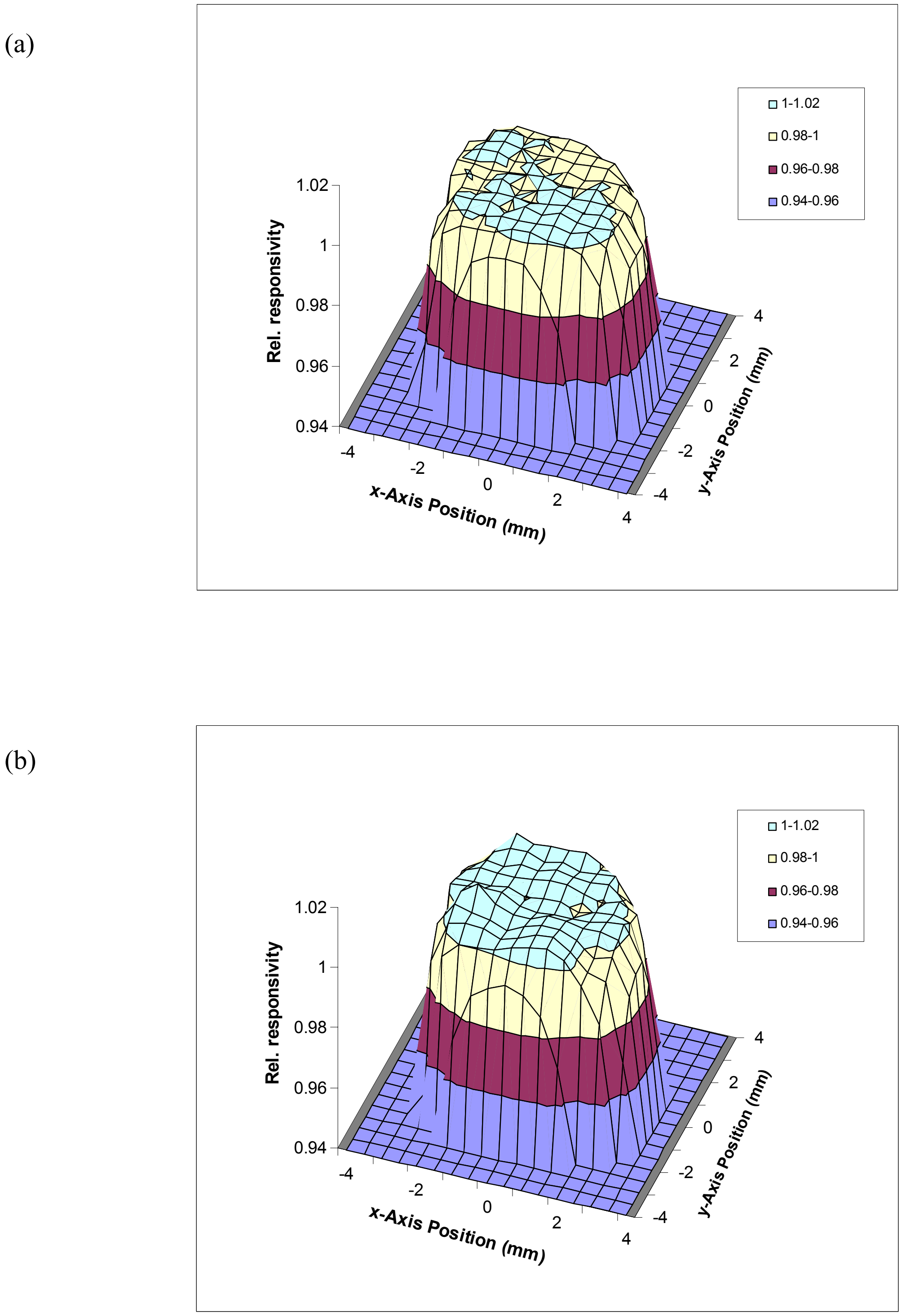

Figure 6.22 Spatial non-uniformity of the responsivity of the Ge-trap measured at 20.5° ± 0.2° with a laser beam of wavelength (a) 1310 nm and (b) 1550 nm and a spot size of $\phi = 1$ mm. The scan was carried out in intervals of 0.5 mm in the two perpendicular axes.

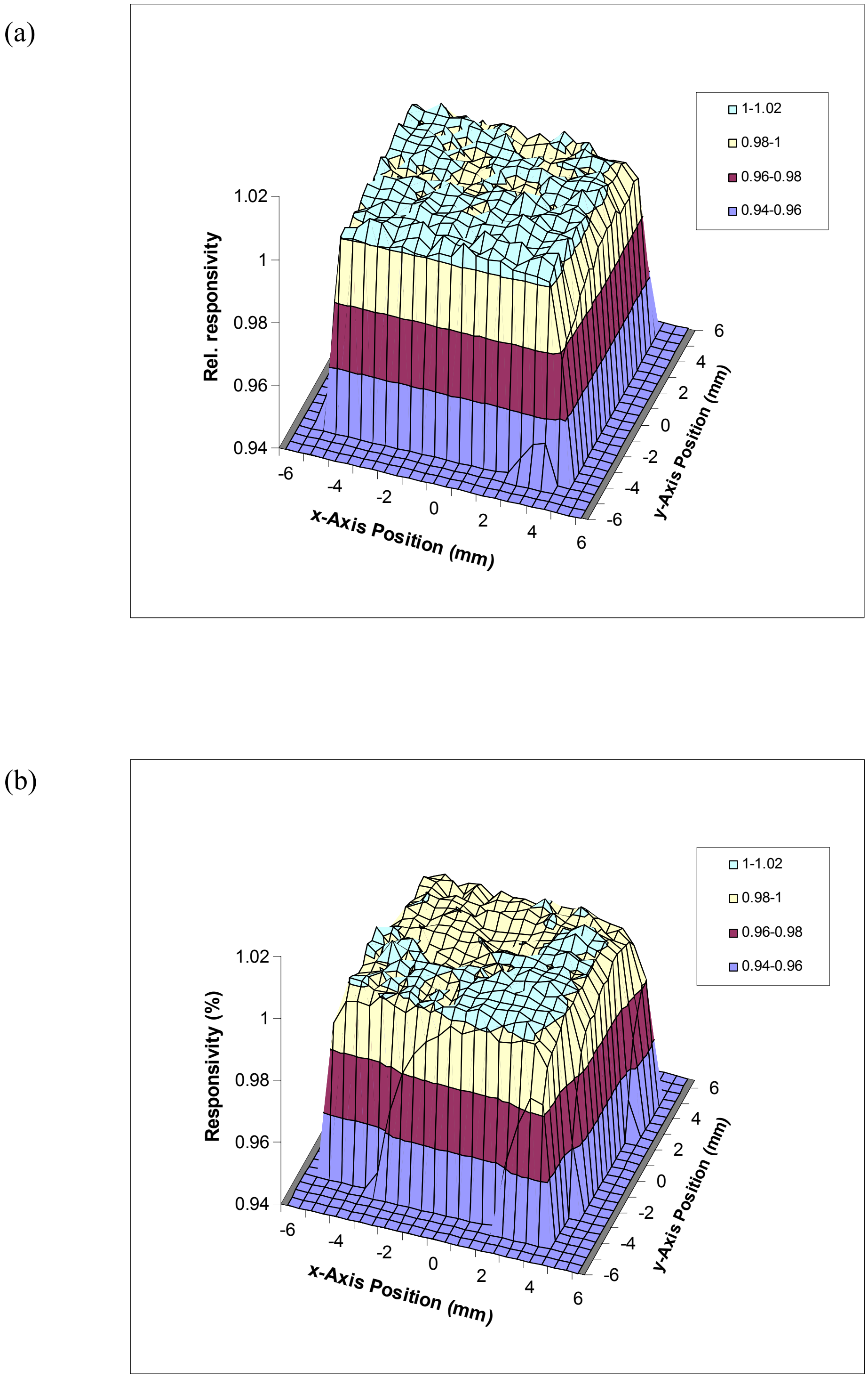

Figure 6.23 Spatial non-uniformity of the responsivity of the InGaAs-photodiode measured at 20.5° ± 0.2° with a laser beam of wavelength (a) 1310 nm and (b) 1550 nm and a spot size of $\phi = 1$ mm. The scan was carried out in intervals of 0.5 mm in the two perpendicular axes.

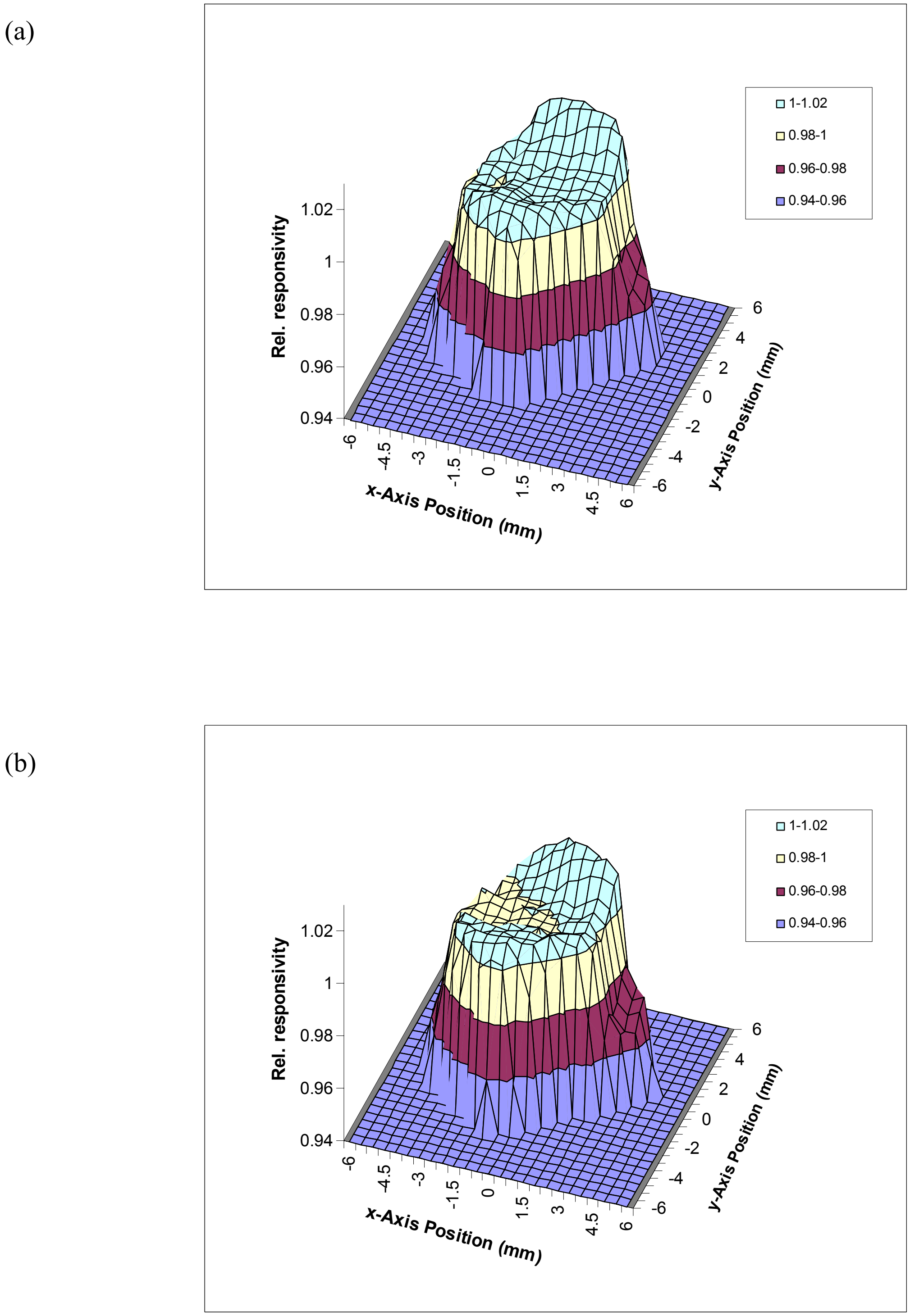

Figure 6.24 Spatial non-uniformity of the responsivity of the InGaAs-trap measured at 20.5°± 0.2° with a laser beam of wavelength (a) 1310 nm and (b) 1550 nm and a spot size of $\phi = 1$ mm. The scan was carried out in intervals of 0.5 mm in the two perpendicular axes.

Although the graphs of the photodiode non-uniformity give an idea of the level of the non-uniformity of the responsivity, it is necessary to quantify the effect of this non-uniformity on a real measurement or calibration. Generally the radiation beam is centered on the sensitive area of the photodiode, when it is used for a calibration or measurement. However, in many cases the beam diameter may be different than the one used on the calibration of the photodiode itself. Table 6.3 shows, as an example, the correction factor for a beam diameter ($\phi = 3$ mm) used typically for calibration of photodiodes, which is 1 mm wider than the one used on the calibration in this work. The correction factors are relative to a 2 mm beam diameter centered on the sensitive area of the photodiode. The highest relative deviation (0.25%) is observed for the Ge-photodiode at 1550 nm. For the rest of the photodiodes the relative deviation is ≤ 0.06 %.

The correction factors and deviation of the responsivity of the Ge- and InGaAs-photodiodes for different spot diameters ($\phi \leq 8$ mm) are shown in Figure 6.25 and 6.26, respectively. The maximal relative deviations observed are 0.3 % and 0.2 % for the Ge- and InGaAs-photodiode, respectively. For the InGaAs-photodiode the deviation of the responsivity is practically negligible for spot diameters between 2 mm and 4 mm at 1550 nm. For the case of the Ge- and InGaAs-trap detectors the deviation of the responsivity is ≤ 0.1 % for beam diameters between 1 mm and 4 mm, see

Figure **6.27** and Figure 6.28. Nevertheless, the deviation increases strongly for spot diameters > 5mm since for a trap detector the main limitation is precisely its field of view. For example, a collimated laser beam of $\phi = 6$ mm will project a spot beam diameter of ≈ 8.5 mm (6 mm / cos (45°)) on the first photodiode of the trap-detector.

Table 6.3 Correction Factor *CF* of the spectral responsivity of the Ge- and InGaAs-trap and single photodiode for a spot diameter (centered on the sensitive area of the diode) of 3 mm. All correction factors were calculated relative to a 2 mm beam diameter.

	Correction factor *CF* for a beam diameter of 3mm	
Photodiode	1310 nm	1550 nm
Ge-single diode	1.0000	0.9975
Ge-trap	1.0000	1.0004
InGaAs-single diode	1.0004	1.0001
InGaAs-trap	1.0006	1.0006

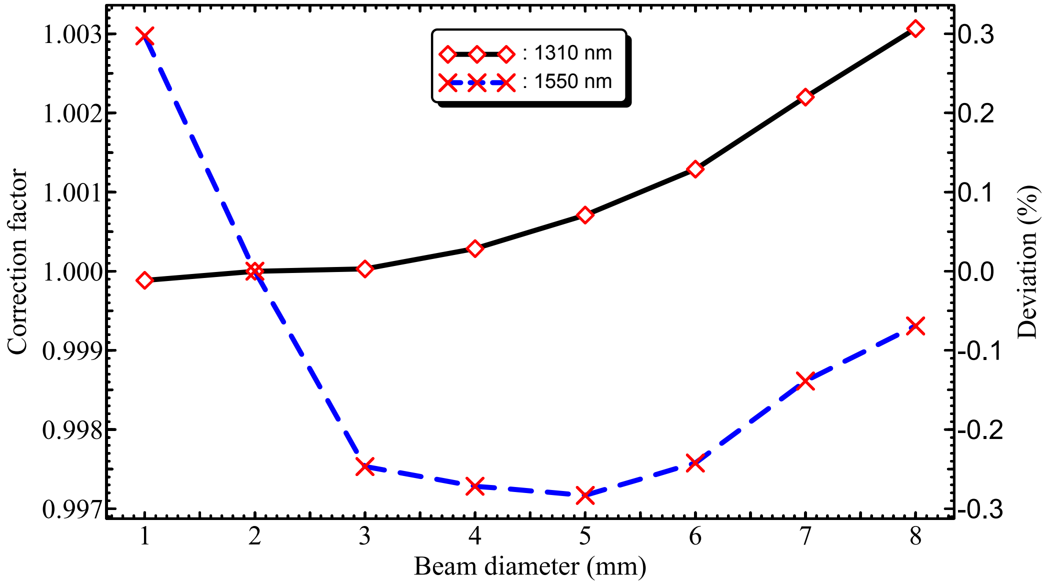

Figure 6.25 Correction factor *CF* of the responsivity of the Ge-photodiode as function of the beam diameter. The *CF*s are relative to a spot size of 2 mm in diameter centered on the active area of the photodiode.

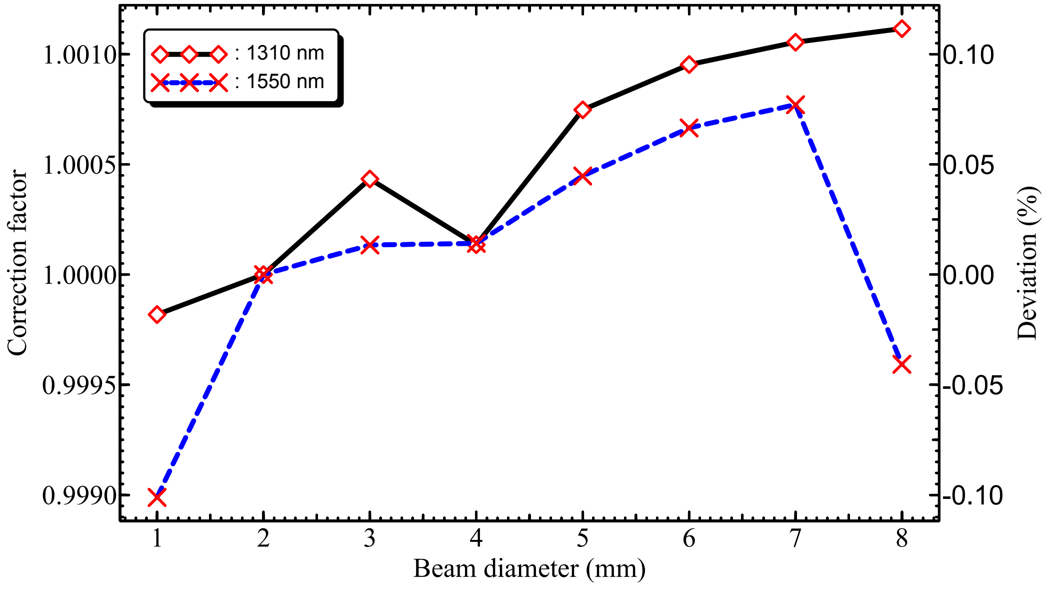

Figure 6.26 Correction factor *CF* of the responsivity of the InGaAs-photodiode as function of the beam diameter. The *CF*s are relative to a spot size of 2 mm in diameter centered on the active area of the photodiode.

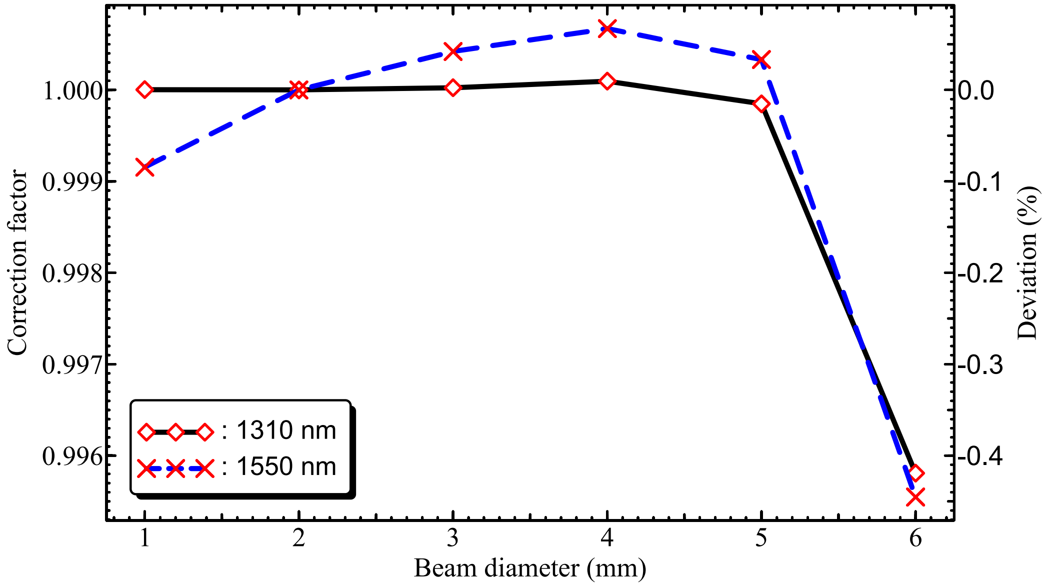

Figure 6.27 Correction factor *CF* of the responsivity of the Ge-trap as function of the beam diameter. The *CF*s are relative to a spot size of 2 mm in diameter centered on the active area of the photodiode.

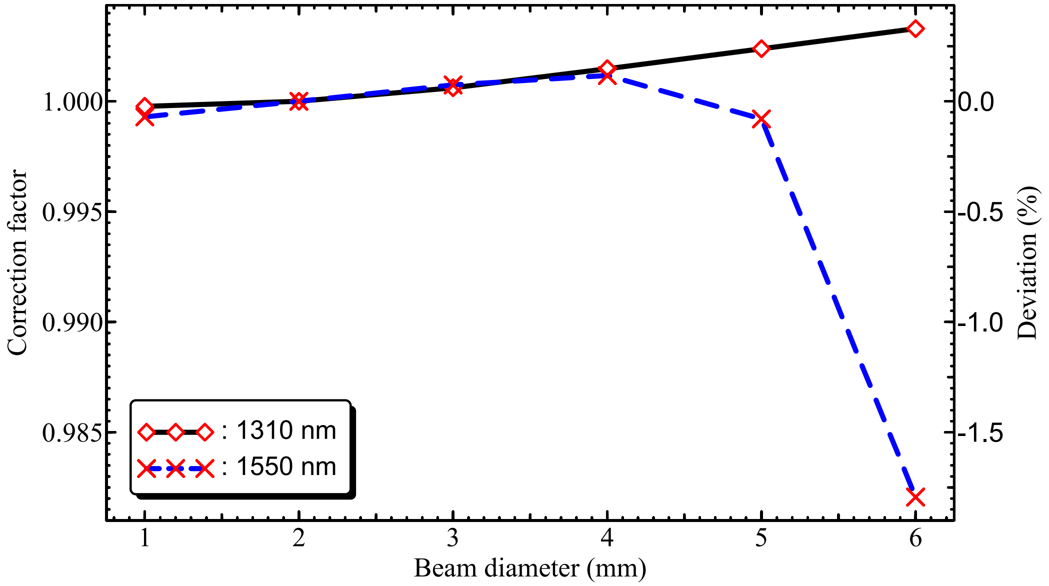

Figure 6.28 Correction factor *CF* of the responsivity of the InGaAs-trap as function of the beam diameter. The *CF*s are relative to a spot size of 2 mm in diameter centered on the active area of the photodiode.

Another source of error that can be quantified from the measurements of the non-homogeneity of the photodiodes responsivity is the case when the beam does not incident on the center of the sensitive area of the photodiode, but on a certain distance $l_{x,y}$ away. As an example, in Table 6.4 and Table 6.5 the relative deviations of the responsivity obtained for a beam spot diameter of 2 mm and 3 mm, respectively, are listed. The responsivity deviations $\mathit{\Delta}S(d;l_{x,y})$ were obtained by calculating the mean value of the responsivity of a beam spot displaced in the two perpendicular axes. The displacements were made in steps of 1 mm. The circular size of the spots was approximated by grid matrix elements.

$$\mathit{\Delta}S\left(d;l_{x,y}\right)=1-\frac{1}{4\cdot\bar{S}\left(d;\mathrm{x}=0,\mathrm{y}=0\right)}\left[\bar{S}(d;\mathrm{x}=l_x,\mathrm{y}=0)+\bar{S}\left(d;\mathrm{x}=-l_x,\mathrm{y}=0\right)+\bar{S}(d;\mathrm{x}=0,\mathrm{y}=l_y)+\bar{S}\left(d;\mathrm{x}=0,\mathrm{y}=l_y\right)\right] \tag{6.16}$$

where $l_{x/y}$ = 1, 2 or 3, $\bar{S}(d;\mathrm{x},\mathrm{y})$ is the mean value of the relative responsivities of the approximated grid matrix and d is the beam spot diameter. The highest deviation of 0.29 % was obtained for the Ge-photodiode when a beam spot of 2 mm diameter was displaced 3 mm from the center of the sensitive area. For the Ge-trap, a beam spot displacement of just 2 mm generates a deviation in the responsivity up to 8.68 %. In general, in order to limit errors at calibration to 0.1 % of all the detectors tested here, it is necessary to keep the beam spot position better than 1 mm with respect to the center of the photodiode sensitive area, which is possible by using an appropriate mechanical mounting system.

Table 6.4 Relative deviation of the responsivity for a displacement $l_{x,y}$ of a beam spot of 2 mm diameter, relative to the center of the sensitive area. The displacements are carried out in steps of 1 mm.

		1310 nm			1550 nm		
Photodiode	$l_{x,y}\rightarrow$	1 mm	2 mm	3 mm	1 mm	2 mm	3 mm
Ge-single diode		-0.02%	0.16%	0.29%	0.02%	0.01%	0.04%
Ge-trap		0.00%	1.77%	-	-0.01%	2.04%	-
InGaAs-single diode		-0.03%	-0.18%	-0.12%	-0.02%	-0.05%	-0.08%
InGaAs-trap		-0.09%	-0.25%	-	-0.09%	-0.25%	-

Table 6.5 Relative deviation of the responsivity for a displacement $l_{x,y}$ of a spot beam of 3 mm diameter, relative to the center of the sensitive area. The displacements are carried out in steps of 1 mm.

	1310 nm				1550 nm		
Photodiode	$l_{x,y} \rightarrow$	1 mm	2 mm	3 mm	1 mm	2 mm	3 mm
Ge-single diode		-0.04%	-0.21%	3.27%	-0.05%	-0.13%	3.59%
Ge-trap		0.10%	8.68%	-	0.12%	9.46%	-
InGaAs-single diode		-0.04%	-0.08%	0.3%	-0.02%	-0.04%	0.01%
InGaAs-trap		-0.08%	1.19%	-	-0.08%	1.15%	-

6.7 Nonlinearity of the photodiodes

As already mentioned, the measurement of the nonlinearity of the photodiodes responsivity is very important for radiometric applications, since it determines the range where the responsivity of the photodiode is constant (linear range), which is a basic request for ratio measurements commonly carried out in radiometric and photometric applications. For ranges where the photodiode is non-linear, a correction factor must be applied. Generally the linearity of the photodiode is limited mainly because of the photodiode saturation (upper limit) and the dark current (lower limit). In this work the main interest is focused on the upper limit, since the aim is the determination of the nonlinearity of the photodiodes responsivity at high irradiance levels and the experimental verification and validation of the different measurement methods.

Thus, the investigation of the nonlinearity of the photodiodes responsivity was carried out by using the three measurement setups described in section 5.4 based on the flux-addition method, DSR-method (*Differential Spectral Responsivity*) and the “relative” method. The photodiodes investigated in this work were single photodiodes only, because the trap detectors are designed mainly for working as a transfer standard where just one specific optical power level is generally used. To the set of photodiodes under investigation - as described in the previous sections - a Ge-photodiode with a sensitive area of 19.64 mm^2 ($\phi = 5$ mm, circular) was added. Table 6.6 lists all photodiode investigated together with their most relevant parameters. The measurements were carried out with an Erbium-Doped Fiber Amplifier (EDFA) as a radiation source tuned to a wavelength of 1550 nm and a diode laser operating at 980 nm. The sensitive areas of the photodiodes were irradiated with a Gaussian beam with a diameter of approx. 0.6 mm. The temperature of the photodiodes was held constant at 20.5° ± 0.5°.

Table 6.6 Parameters of the photodiodes under test.

Name	**Type**	**Manufacturer**	***S* (A/W) λ: 1550 nm**	**R_{shunt} (kΩ)**	**Diameter/ form**	**Sensitive area**
J16 810069	Ge-*pn*	Judson	0.90	20	5 mm / circular	19.64 mm^2
B1920-01SPL	Ge-*pn*	Hamamatsu	0.86	0.5	10 mm / circular	78.54 mm^2
35PD10M	InGaAs-*pin*	Anadigics	1.04	40	10 mm × 10 mm	100 mm^2

Figure 6.29 shows the nonlinearity, measured with the DSR method, of the three photodiodes as a function of the photocurrent for a wavelength of 1550 nm. All photodiodes investigated show a nonlinearity of the saturation type. It means that the responsivity of the photodiode decreases with an increase of the radiant power level. The Ge-photodiodes are very linear up to a photocurrent of around 6 mA, which is equivalent to an optical radiation power of approximately 7 mW. However, after this point the responsivity begins to be non-linear. The high saturation of the Ge-photodiodes starts at a photocurrent of the order of 10 mA where a nonlinearity of 1.2 % and 0.5 % for the J16-810069 and B1920-01SPL Ge-photodiode were found, respectively. The maximal nonlinearity measured was 40 % at 18 mA (28 mW). On the other hand, the InGaAs photodiode is linear up to a photocurrent of 3 mA (2.9 mW) and the maximal nonlinearity measured was 26.5 % at 6.9 mA (8.4 mW). Because of the high nonlinearity of the InGaAs-photodiode responsivity for optical power > 3 mW, this photodiode was measured just up to 8.4 mW, in order to avoid any damage of the photodiode.

Note that the nonlinearity of the Ge-photodiode J16 810069 is smaller than the rest of the photodiodes at the same photocurrent level. The nonlinearity of the saturation type of a photodiodes depends on the shunt resistance R_{shunt}, series resistance R_{s} and load resistance R_{L}. Photodiodes with high shunt resistance R_{shunt}, low series resistance R_{s} and low load resistance R_L present larger linearity range, as will be discussed in detail in section 6.6.1.

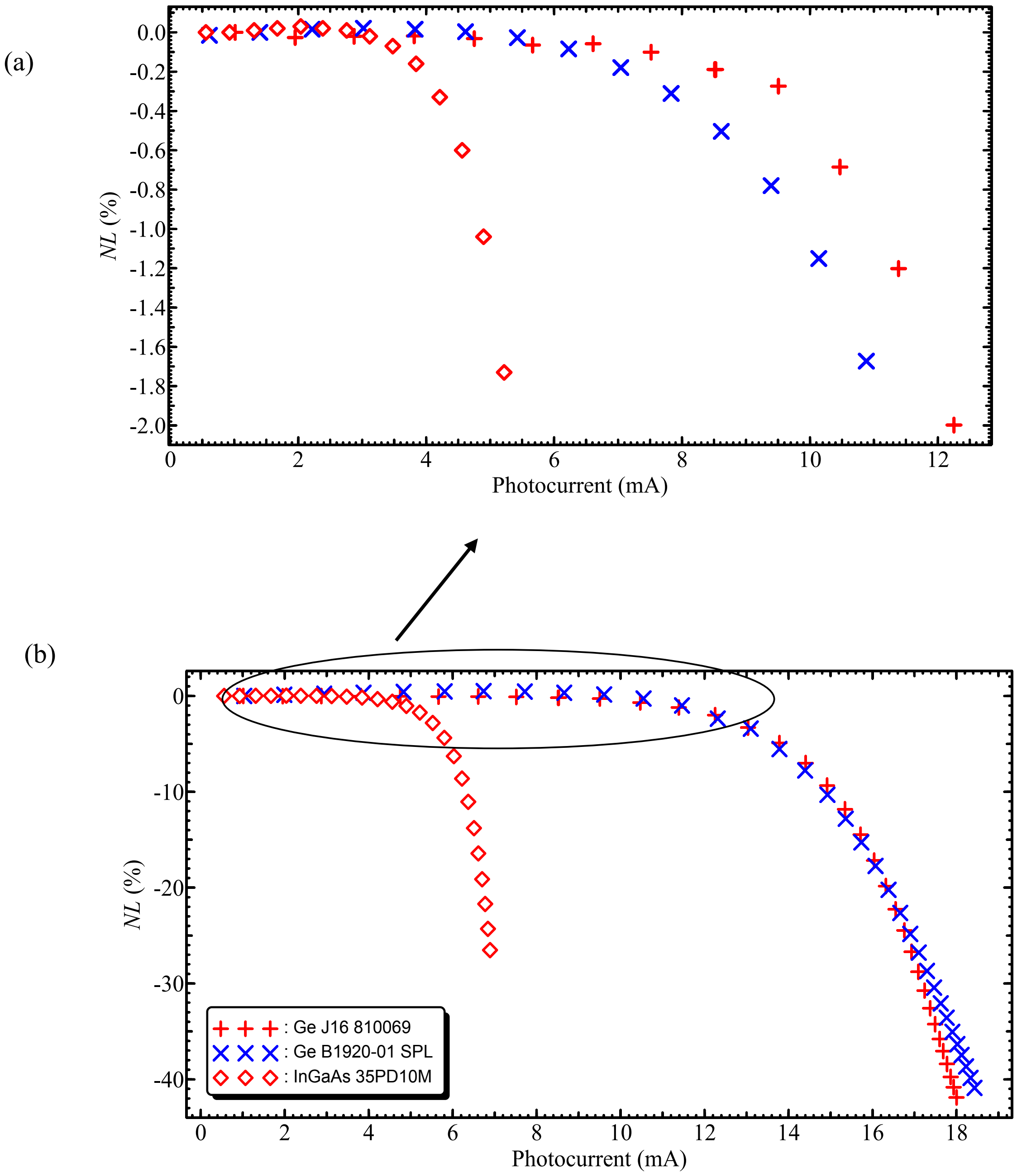

Figure 6.29 Nonlinearity of the Ge- and InGaAs-photodiodes measured at a wavelength of 1550 nm and a beam diameter of 0.6 mm. (a) Detailed view and (b) Overview.

The nonlinearity of the InGaAs- (35PD10M) and the Ge-photodiode (J16-810069) responsivity as a function of the optical radiant power and irradiance (W/mm^2) is given in Figure 6.30 and 6.31, respectively. The nonlinearity of the photodiodes was measured by using the DSR-, relative- and flux-addition-method (as validation). In both figures, a good consistency of the nonlinearity measurements with the different methods is observed. These measurements show the compatibility of the three methods. The maximal nonlinearity measured was 25 % at 8.5 mW (33.3 mW/mm^2) for the InGaAs-photodiode and 24.5 % at 23 mW (90.0 mW/mm^2) for the Ge-photodiode (J16-810069).

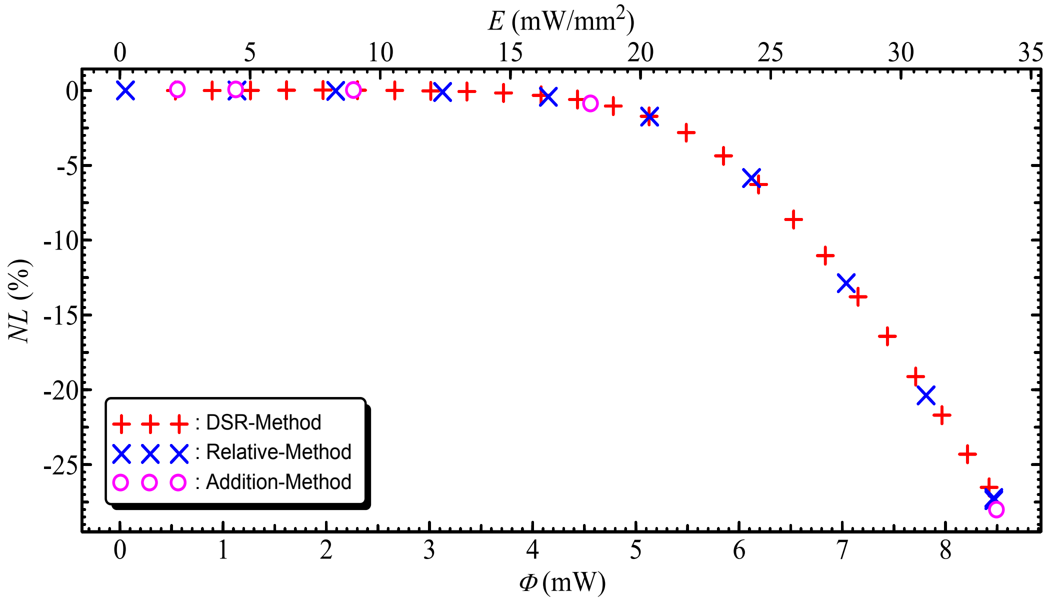

Figure 6.30 Nonlinearity of the InGaAs-photodiode (35PD10M) measured with the three methods (DSR, “relative” and flux-addition). Radiation source: EDFA tuned at a wavelength of 1550 nm (beam diameter: 0.6 mm, temperature: 22 ± 0.5°).

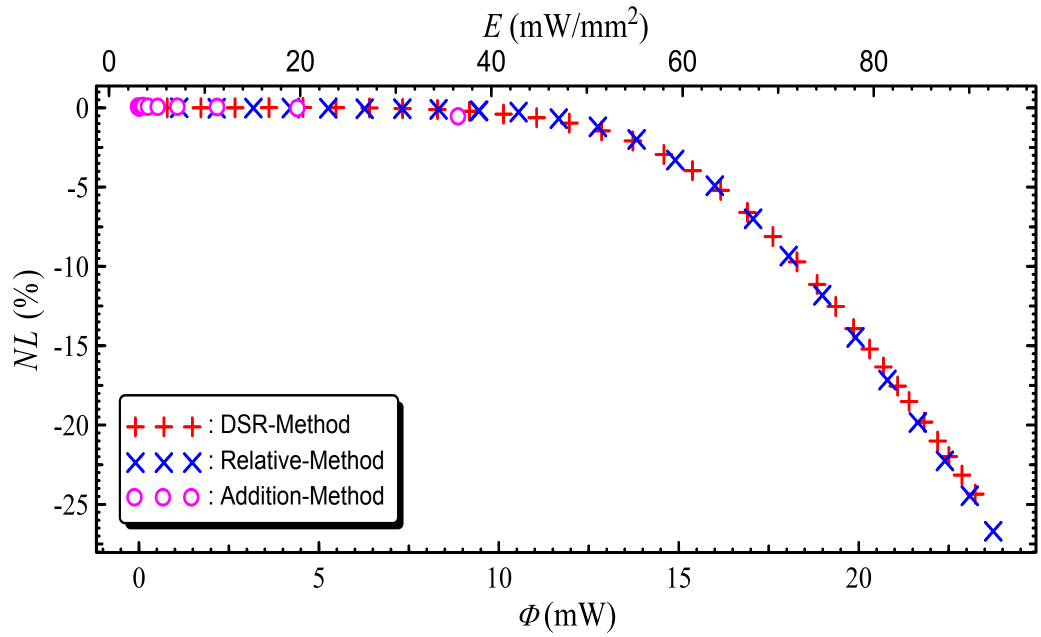

Figure 6.31 Nonlinearity of the Ge-photodiode (Judson J16-810069) measured with the three methods (DSR, "relative" and flux-addition). Radiation source: EDFA tuned at a wavelength of 1550 nm (beam diameter: 0.6 mm, temperature: 22 ± 0.5°).

By using the measurement setup described in section 5.4 (DSR-method), the nonlinearity of the Ge- (Judson J16-810069) and InGaAs- (35PD10M) photodiode was investigated also for 980 nm**.** Figure 6.32 compares the nonlinearity of both photodiodes for 980 nm and 1550 nm as a function of the photocurrent. The curves overlap, which proofs that the nonlinearity of saturation type is just a pure effect of the forward current loss into the diode. Obviously, the optical power needed at a wavelength of 1550 nm to reach the photodiode saturation is lower than for an optical power at 980 nm, because of the responsivity of the photodiodes, i.e. absorption of the photodiode itself.

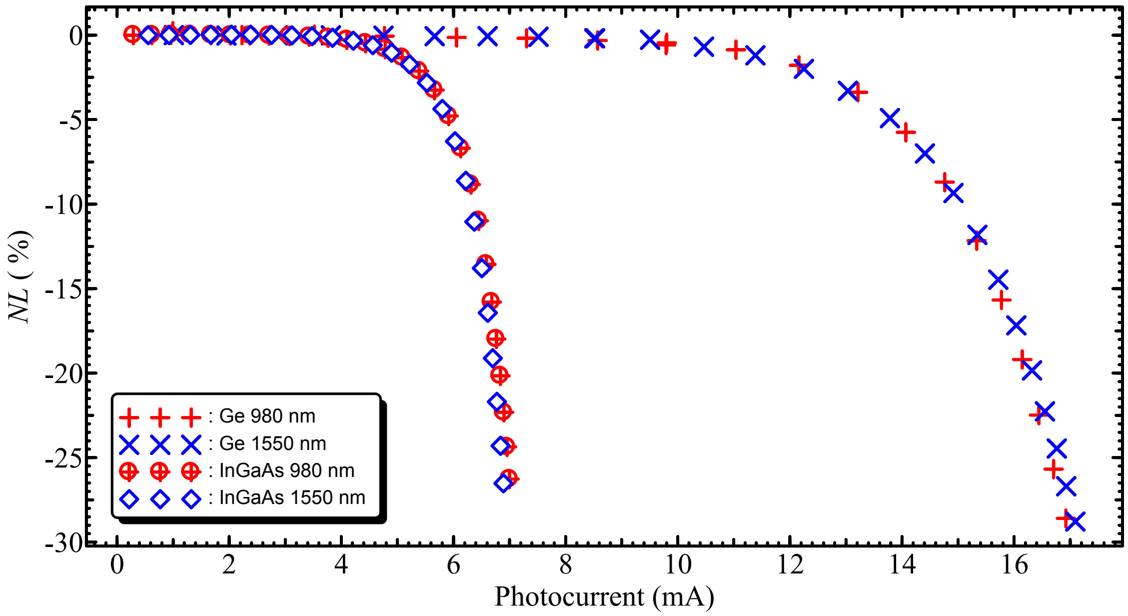

Figure 6.32 Nonlinearity of the Ge (Judson J16-810069)- and InGaAs (35PD10M)-photodiode at 980 nm and 1550 nm (beam diameter: 0.6 mm, temperature: 22 ± 0.5°).

6.7.1 Saturation of the photodiodes

The saturation of a photodiode can be explained by means of its equivalent circuit, see Figure 2.3 in section 2.2. For the case when the photodiode is operated in photoconductive mode (without V_{bias}), the total external current I_{T} of the circuit results as,

$$\begin{aligned} I_{\text{T}} &= I_{\text{ph}} - I_{\text{d}} - I_{\text{shunt}} \\ &= I_{\text{ph}} - I_{\text{sat}}\left(\exp\left(\frac{qV_{\text{d}}}{kT}\right)-1\right)-\frac{V_{\text{d}}}{R_{\text{shunt}}} \end{aligned} \tag{6.17}$$

Substituting V_{d} by $I_{\text{T}} \cdot (R_{\text{s}} + R_{\text{L}})$ in equation (6.17),

$$I_{\text{T}} = I_{\text{ph}} - I_{\text{sat}}\left(\exp\left(\frac{qI_{\text{T}}}{kT}(R_{\text{s}}+R_{\text{L}})\right)-1\right)-\frac{I_{\text{T}}}{R_{\text{shunt}}}(R_{\text{s}}+R_{\text{L}}). \tag{6.18}$$

For low optical radiation the voltage across the diode V_{d} is maintained at very low level. Thus, if $R_{\text{s}} << R_{\text{L}}$ and $R_{\text{shunt}} >> R_{\text{L}}$, the diode current I_{d} and shunt current I_{shunt} are negligible resulting that $I_{\text{T}} \approx I_{\text{ph}}$. So, in this case the total current I_{T} is proportional to the optical radiation power, this is the linear case. Note that in order to keep the photodiode linear, the conditions mentioned above require either the resistivity of the junction R_{shunt} to be very high or the load resistance R_L to be a short circuit. Otherwise when the photodiode is illuminated with high optical radiation, the voltage across the diode V_d increases significantly causing a forward injection current into the diode (I_d and I_{shunt} increase), which reduces the total current I_T to the external circuit load (non-linear case).

Due to the condition mentioned above, the photodiodes are operated in radiometry generally in the short-circuit mode or unbiased photoconductive mode with $R_L \approx 0$. In practice, the photodiode is connected to an operational amplifier OA, which is used as a current-voltage converter known also as trans-impedance amplifier, see Figure 6.33. In this circuit, the output voltage V_0 is proportional to the signal current I and the feedback resistance R_f. That is,

$$V_0 = I \cdot R_f. \tag{6.19}$$

A capacitor C_f is usually connected across the feedback resistor R_f to reduce the electrical noise. Here the RC time constant should be as large as permissible within the required response time of the measurement. The load impedance of a trans-impedance amplifier is given by [67],

$$Z_L = \frac{R_f}{G_o\left(1+\omega^2 R_f^2 C_f^2\right)^{1/2}}, \tag{6.20}$$

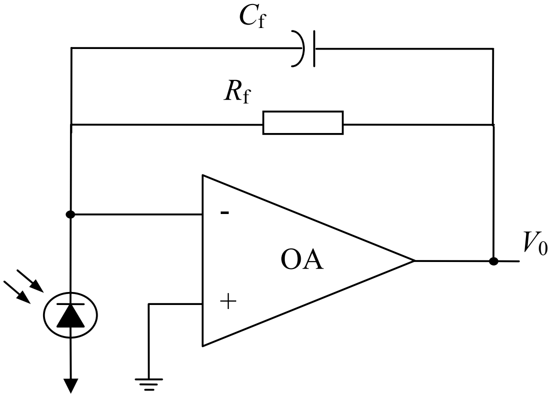

Figure 6.33 Basic circuit for unbiased operation of a photodiode. The circuit uses an operational amplifier which provides a short-circuit load to the photodiode.

where G_0 is the open loop gain of the operational amplifier and ω the signal frequency. For constant radiation $\omega = 0$, the equation (6.20) is then given by,

$$Z_{\mathrm{L}} = \frac{R_{\mathrm{f}}}{G_0} \tag{6.21}$$

Note that from the point of view of the photodiode, $Z_{\mathrm{L}} = R_{\mathrm{L}}$. Thus, according to equation (6.21), to obtain low load impedance, a high open loop gain of the operational amplifier and low feedback resistance as feasible are required. These two requirements are needed to achieve the best linearity of the photodiode. Therefore, in this work the photodiodes under test were connected to a low noise trans-impedance amplifier (OPA128LM) with a typical open loop gain G_0 of 1×10^6 and feedback resistors of 1 kΩ and of 10 kΩ, which results in a load impedance Z_L of 1×10^{-3} Ω and 1×10^{-2} Ω, respectively.

So far, considering that $R_{\mathrm{L}} \approx 0$, the parameters that limit the linearity range of the photodiodes are basically the shunt resistance R_{shunt} and the series resistance R_{s}. However, the shunt resistance of the photodiodes is normally high; e.g. high quality Si-photodiodes have a typical shunt resistance of 1 GΩ. The shunt resistances of the photodiodes investigated in this work are given in Table 6.6. The value of the shunt resistance is about inversely proportional to the sensitive area and the temperature of the diode; e.g. the Ge-photodiode (B1920-01SPL) with an area of 78.54 mm^2 has a shunt resistance of 2 kΩ, while the shunt resistance of the Ge-photodiode (J16 810069) with an area of 19.64 mm^2 is of 20 kΩ.

On the other hand, the series resistance R_{s} formed by the sum of the contact resistance and the undepleted bulk material is typically low. Unfortunately this parameter is not given by the manufacturer. Under carefully design, the series resistance R_{s} is typically on the order of 10 Ω - 100 Ω. Actually, the exact value of the series resistance R_{s} is not easy to determine experimentally since it may be distributed, that is, it may have also components like for example, surface resistance, etc. In practice, rather than measure R_{s} it is easier to perform direct the measurement of the linearity of the photodiode responsivity and from their to determine R_{s}. That is, knowing the nonlinearity of the photodiode responsivity, the photocurrent I_{ph} can be determined by

$$I_{\mathrm{ph}} = I_T\,(NL\text{-}1) \tag{6.22}$$

Thus, assuming that $R_{\text{shunt}} >> R_s$ and $R_L \approx 0$, the series resistance R_s can be estimated by fitting the value of R_s in equation (6.18). The best values of R_s fitted to the nonlinearity measurements of the tested photodiode in this work are listed in Table 6.7.

Once R_s is known and by measuring I_T, I_{ph} can be calculated from the equation (6.18). Thus, the nonlinearity of the photodiode is obtained then as,

$$NL_{\text{calc}} = (I_{ph} - I_T) / I_T. \tag{6.23}$$

As an example, in Figure 6.34 the calculated and measured nonlinearity of the investigated photodiodes are shown. Deviation between measured and calculated values of the nonlinearity occurs from the assumption that $R_{\text{shunt}} >> R_s$, which is not absolutely fulfilled.

Table 6.7 Estimated value of the series resistance R_s of the photodiodes.

Photodiode	**Series resistance R_s**
Ge (J16 810069)	16.56 Ω
Ge (B1920-01SPL)	15.00 Ω
InGaAs (35PD10)	52.67 Ω

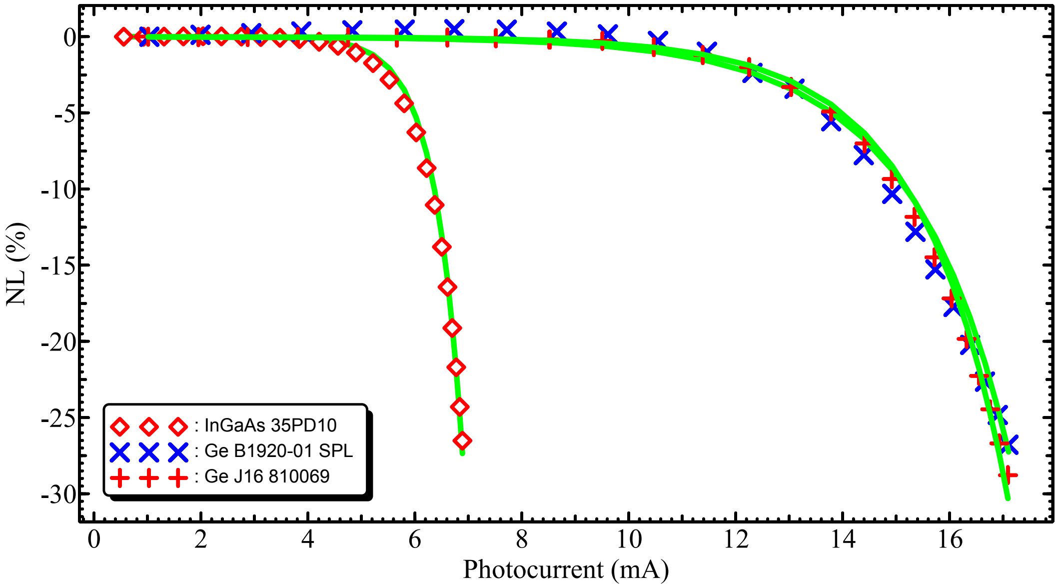

Figure 6.34 Measured and calculated (solid line) nonlinearity of the Ge- and InGaAs-photodiodes. The measured values are the same as the shown in Figure 6.29. The nonlinearity was calculated by $NL_{\text{calc}} = (I_{ph} - I_T) / I_T$, see text above.

6.8 Discussion

The results shown in this chapter are satisfactory from the point of view that they reveal the high potential of the Ge- and InGaAs-trap and single detectors to be used as transfer standards for high accuracy optical radiant power measurements in the near infrared. However, the part corresponding to the model of the photodiode reflectance, shown in section 6.2.1, exhibits some weakness, which is necessary to discuss in more detail.

In the model of the reflectance of the InGaAs-photodiode it was mentioned that the values of the refractive index of InP:Zn (*p*-layer) and InP:S (*n*-layer) differ from the refractive index of an undoped InP layer because of the doping and doping level. This argument was based on the values of the refractive index of InP:Zn reported by S. B. Youssef in Ref. [66]. In fact, it is well known that the refractive index of a semiconductor depends not only on the doping element and doping level, but also on the crystal composition, lattice mismatch, carrier density, temperature, etc. [68]. Therefore, in this work the refractive index of these layer were obtained by fitting an appropriated dispersion equation to the experimental data, see section 6.2.1. The refractive index obtained for InP:Zn was compared to the values reported in [66] and to the values of undoped InP [69], see Figure 6.35.

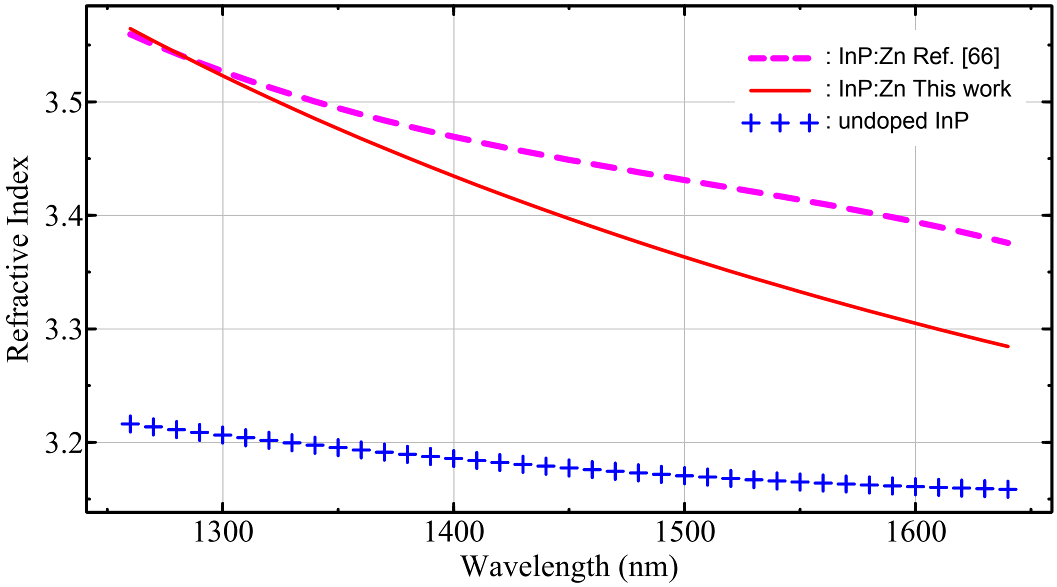

Figure 6.35 Refractive index of InP:Zn obtained in this work and the one reported in [66]. For comparison, the refractive index of undoped InP [69] is also shown. The refractive index of InP:Zn [66] corresponds to a sample of 10 × 8 × 0.5 mm with a carrier concentration of 2×10^{18} cm^{-3}.

Note that the refractive index obtained in this work is close to the one reported in [66], but there still are some differences which may be attributed to the dependences mentioned previously. However, the refractive index obtained in this work for InP:Zn and InP:S, and the values reported in [66] show significant deviations from the values reported by Patrick Martin et. al. [68], Laurent Chusseau et. al. [70] and B. Broberg et. al. [71]. As an example, Table 6.8 lists the refractive indices reported by the authors mentioned above and the refractive indices obtained in this work. Neglecting [66], the deviations between the fitted InP:Zn and InP:S values and the mean value of [68, 70 and 71] are about ~0.5 and ~0.3, respectively. Although the reflectance model is well fitted to the experimental data, the parameters in the dispersion functions may be forced to values which may result in overestimation or underestimation. The main errors that may contribute to the overestimation of the InP:Zn and InP:S values are for example: non-appropriate model, systematic errors in the measurement data, susceptible wrong convergence of the fitting process itself, etc.

Table 6.8 Refractive indices reported by several authors for *p*- and n-type InP samples at $T = 300$ K. n.s.= no specified.

Ref.	**Doping type**	**Doping level ($\times 10^{18}$ cm^{-3})**	**Refractive index $\lambda \sim 1300$ nm**	**Refractive index $\lambda \sim 1550$ nm**
[69]	undoped	≤ 0.05	3.20475	3.1658
[66]	Zn	$N = 2$	3.5268	3.4136
[68]	n.s.	$N = 2$	3.19929	3.15630
[70]	S	$N = 8.2$	3.1671	3.1251
	Zn	$P = 3.6$	3.2021	3.1616
[71]	S	$N = 1.2$	3.186	n.s.
	Zn	$P = 0.7$	3.161	
This work Eq. (6.10)	S	n.s.	3.701	3.575
This work Eq. (6.11)	Zn	n.s.	3.523	3.332

(a) Non-appropriate model

If the model does not fulfill totally the structure of the photodiode, it will carry some errors in the estimation of the dispersion functions of the refractive indices. Since this information is not provided by the manufacturer, the photodiodes investigated in this work were approximated by a basic structure: AR-coating/Ge and AR-coating/InP:Zn/InGaAs/InP:S for Ge and InGaAs, respectively. Thus, any additional layer which is not taken into account in the model may overestimate the real refractive index of the layer. This error could be the most probable one in the case of the determination of the refractive indices of InP:Zn and InP:S in this work.

(b) Systematic errors in the measurement data

It has been demonstrated that systematic errors in the measurement data may have significant effects in the determination of the optical parameters of thin-film coatings [72]. Typical systematic errors are, for example, the error in the angle on incidence, a misalignment between incidence and polarization planes, etc. Although the systematic errors in the measurement in this work were minimized due to the good characterization of the spectrophotometer of the PTB, they are not totally eliminated and may contribute to the determination of the refractive indices.

(c) Wrong convergence of the fitting

The correct convergence of the fitting depends also on the starting input parameters introduced in the minimization of the sum-of-squares discrepancy. In order to minimize this error source, the start parameters introduced in this work were selected according to the materials assumed in the model. However, the errors (a) and (b) already mentioned may contributed also to a wrong convergence of the fitting.

7 Estimation of the measurement uncertainty

7.1 Basic concepts

In general, a measurement is complete only when its result is accompanied by a quantitative statement of its uncertainty. The uncertainty of a measurement is defined as a “parameter, associated with the result of a measurement that characterizes the dispersion of the values that could reasonably be attributed to the measurand” [73]. The measurand is the quantity subject to be measured, e.g. the absolute spectral responsivity, the nonlinearity, etc. Since the definition of the uncertainty deals with a statistical concept, the measurement uncertainty can be expressed as a standard deviation or also as an interval where the true value of the measurand, with a certain probability, may be found.

The most common method to evaluate and to express the measurement uncertainty is based on the “*Guide to the Expression of Uncertainty in Measurement*” (GUM) [74]. This guide, published at the first time in 1993 and based on the CIPM approach, has been adopted worldwide by most of the National Metrology Institutes (NMIs), calibration and test laboratories, industry, etc. for evaluating and expressing the measurement uncertainty. On the other hand, a practical alternative to evaluate the uncertainty of a measurement is the Monte Carlo method [75, 76], which has shown to be useful for example, when the linearization of the measurand model provides an inadequate representation or when the output quantity differs from a Gaussian distribution. Both, the GUM and the Monte Carlo method are totally compatible [76, 77]. In this work, both methods are used depending on the measurand model.

7.1.1 Evaluation of the measurement uncertainty according to GUM

According to the GUM, the first step for evaluating the measurement uncertainty consists in defining the measurand. In many cases, a measurand Y is not measured directly, but is determined from N other quantities $X_1, X_2, \ldots, X_N$ through a function f:

$$Y = f(X_1, X_2, \ldots, X_N). \tag{7.1}$$

In the quantities X_i are included not only physical amounts, but also corrections (or correction factors) as well as quantities that can contribute to the measurement uncertainty, e.g. different observers, instruments, samples, etc.

An estimate of the measurand Y, denoted by y, is obtained from equation (7.1) by using input estimates x_1, x_2,…x_N for the values of N input quantities X_1, X_2, . . . ,X_N . Thus, the best estimate y (measurement result) is obtained from the best estimates $\bar{x}_\mathrm{k}$ of the input quantities. For example, if X_K is obtained from repeated measurements, the best estimate is the mean value of the n individual observations x_k.

$$\bar{x}_\mathrm{k} = \frac{1}{n} \cdot \sum_{i=1}^{n} x_\mathrm{i} \tag{7.2}$$

The second step is the evaluation of the uncertainty of each input quantity. Here the GUM classifies the uncertainty evaluation by two types: the evaluation of the uncertainty by the statistical analysis of series of observations, the so-called Type A evaluation, and the evaluation of the uncertainty by means other than the statistical analysis, named Type B evaluation. The Type A evaluation of the standard uncertainty is obtained generally by means of repeated observations of the input quantity X, where the dispersion of the random errors is obtained through its standard deviation. That means that the standard uncertainty u_A due to the repeatability of the measurement is estimated by the experimental standard deviation of the mean value $\bar{x}$, that is,

$$u_\mathrm{A}(x) = s(\bar{x}) = \frac{1}{\sqrt{n}} \cdot \sqrt{\frac{1}{n-1} \cdot \sum_{\mathrm{i}=1}^{n} (x_\mathrm{i} - \bar{x})^2}\ . \tag{7.3}$$

The type B evaluation of the standard uncertainty refers to any method different from the statistical analysis. It is based on scientific judgment using all the relevant information available; e.g. manufacturer's specifications, previous measurement data, data provided in the calibration and other reports, etc. In this method one can consider known systematic errors as well as not known random errors, which are, for example, represented by the calibration uncertainty of the instrument, its resolution, hysteresis, variability of the environment conditions, etc. Frequently, in this case it is supposed that the quantity in question lies, with a probability distribution, in the interval $\Delta a = a_+ - a_-$, where a_+ and a_- are the upper and lower limits of the quantity. The probability distribution may be uniform, triangular, sinusoidal etc. If the probability distribution is uniform or rectangular, which is very common, the standard uncertainty type B is obtained as:

$$u_{\mathrm{B}}(x) = \frac{a_{+} - a_{-}}{2 \cdot \sqrt{3}}. \tag{7.4}$$

The combined standard uncertainty $u_{\mathrm{c}}(y)$ of the measurand is calculated as a linear approach of the model. It is obtained by combining the individual standard uncertainties u_{i}, these can be evaluation Type A or Type B. That is,

$$u_{\mathrm{c}}^{2}(y) = \sum_{\mathrm{i=1}}^{\mathrm{N}} \left(\frac{\partial f}{\partial x_{\mathrm{i}}} \right)^{2} u^{2}(x_{\mathrm{i}}) + 2 \sum_{\mathrm{i=1}}^{\mathrm{N-1}} \sum_{\mathrm{j=i+1}}^{\mathrm{N}} \frac{\partial f}{\partial x_{\mathrm{i}}} \frac{\partial f}{\partial x_{\mathrm{j}}} u(x_{\mathrm{i}}) u(x_{\mathrm{j}}) r(x_{\mathrm{i}}, x_{\mathrm{j}}) \tag{7.5}$$

Equation (7.5) is also known as the *law of propagation of uncertainty*, which is based on the first-order Taylor series approximation. The partial derivatives $\partial f / \partial x_{\mathrm{i}}$ are known as the *sensitivity coefficients* and $u(x_{\mathrm{i}})$ and $u(x_{\mathrm{j}})$ are the standard uncertainties associated to the inputs quantities x_{i} and x_{j}, respectively and $r(x_{\mathrm{i}}, x_{\mathrm{j}})$ is the correlation coefficient. The correlation coefficient characterizes the degree of correlation between x_{i}, x_{j}, where its value can be found between -1 and +1. If the estimates x_{i} and x_{j} are independent, then $r(x_{\mathrm{i}}, x_{\mathrm{j}}) = 0$, and equation (7.5) is reduced to

$$u_{\mathrm{c}}^{2}(y) = \sum_{\mathrm{i=1}}^{N} \left(\frac{\partial f}{\partial x_{\mathrm{i}}} \right)^{2} u^{2}(x_{\mathrm{i}}). \tag{7.6}$$

Equation (7.6) is most commonly used for calculating the measurement uncertainty assuming that the input quantities are not correlated. However, if two or more input quantities are significantly correlated, the estimation of the measurement uncertainty may be over-estimated or under-estimated. Note that correlation between input quantities can be used to lower the uncertainty of a measurand.

The combined standard uncertainty $u_{\mathrm{c}}(y)$ can be used to express the uncertainty of a measurement result y in many practical measurement situations. However, because its probability distribution is approximately normal in most of the cases, it is believed that the measurand Y is found between the interval $y\text{-}u_c(y) \leq Y \geq y+u_c(y)$ with a level of confidence p of approximately 68%. Nevertheless, there are situations (e.g. when health and safety are concerned) where higher confidence levels are necessary. In this case, the uncertainty of the measurement result is frequently expressed as an expanded uncertainty $U(y)$, and is obtained by multiplying $u_c(y)$ by a coverage factor k. That is,

$$U(y) = k \cdot u_c(y). \tag{7.7}$$

The coverage factor $k(v_{\text{eff}}, p)$ depends on the “effective degree of freedom” v_{eff} of the output quantity and the confidence levels p wished or required in the application. Typically, a confidence levels p of 95.45 % is recommended in most of the fields. Table 7.1 lists the values of the coverage factor $k(v_{\text{eff}}, p)$ for a confidence level p = 95.45 % and a variety of effective degree of freedom $1 \leq v_{\text{eff}} \leq \infty$. The effective degree of freedom v_{eff} is calculated from the Welch-Satterthwaite formula [74],

$$v_{\text{eff}} = \frac{u_{\text{c}}^4(y)}{\sum_{\text{i}=1}^{n} \frac{u_{\text{i}}^4(y)}{v_{\text{i}}}}. \tag{7.8}$$

For input quantities with standard uncertainties type A, the degree of freedom v_i is limited by the number of readings n; that is $v_i = n - 1$. On the other hand, the degree of freedom is infinite $v_i \to \infty$ for input quantities with type B evaluation of uncertainty. Note that, according to equation (7.8), the effective degree of freedom v_{eff} increases with an increasing number of input quantities with standard uncertainty type B. In many cases $v_{\text{eff}} > 50$ and as listed in Table 7.1 a coverage factor $k = 2$ can be used. For $v_{\text{eff}} \leq 50$ the related coverage factor listed in Table 7.1 has to be used.

Table 7.1 Coverage factor values from the t-distribution for an effective degree of freedom v_{eff} and a fixed confidence level p = 95.45 %.

v_{eff}	1	2	3	4	5	6	7	8	9	10	20	50	∞
$k(v_{\text{eff}})$	13.97	4.53	3.31	2.87	2.65	2.52	2.43	2.37	2.32	2.28	2.13	2.05	2.0

7.1.2 Evaluation of the measurement uncertainty by using the Monte Carlo Method

As mentioned previously, the Monte Carlo method is a practical alternative to the GUM for evaluating the measurement uncertainty, specially for the case when the mathematical model of the measurand is non-linear or when the probability density function (PDF) for the output quantity differs appreciably from a Gaussian distribution.

The Monte Carlo method is a numerical procedure valid practically for any model. Here, the value and the associated uncertainty of the output quantity Y, represented by y, are assigned by a large number of simulated observations (see Figure 7.1). The values of the output quantity y are evaluated from the values of the input quantities x_i with the associated standard uncertainty $u(x_i)$. The shape of the probability distribution of such quantities may be normal $N(x_i, u(x_i))$, rectangular $R(x_i, u(x_i))$, or any other type. The related probability distributions are generated by means of random values.

As an example, for a single input quantity $N_{i,j} = N_j(x_i, u(x_i))$ the output quantity $y_{i,j} = f(x_1, x_2,..N_{i,j},..,x_N)$ can be evaluated for $1 < j < m$. Thus, the variance u_i^2 of the simulated values can be seen as the combined uncertainty of the mean values y_i. The values of all input quantities are simulated independently and in order to form an appropriate distribution, m is chosen often higher than 10000. Thus, from the simulated values of the output quantity, the mean value y and its associated variance $u(y)$ are calculated by

$$y = \frac{1}{m}\sum_{j=1}^{m} f\left(N_{1,j}, N_{2,j}, \ldots, N_{N,j}, \ldots, N_{N,j}\right) \tag{7.9}$$

$$u(y) = \sqrt{\frac{1}{m(m-1)}\sum_{j=1}^{m\cdot N}\left[f\left(N_{1,j}, N_{2,j}\ldots, N_{i,j}\ldots, N_{N,j}\right) - y\right]^2} \tag{7.10}$$

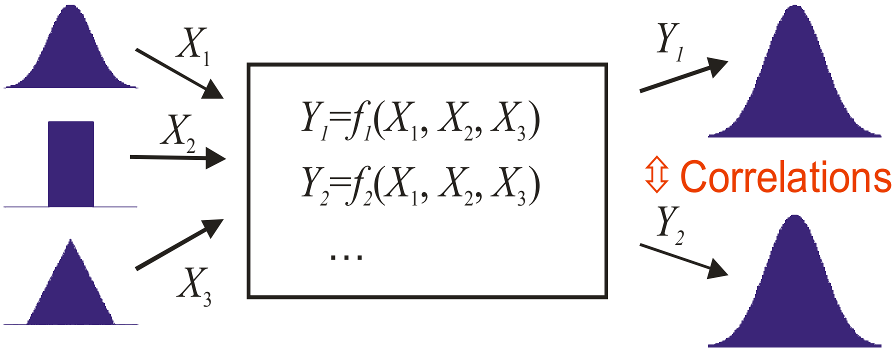

Figure 7.1 Principle of the Monte Carlo method. The numerical simulation is as follow: First, a complete set of random input variables X_i with appropriate distributions are generated. Second, the generated input variables X_i are used to calculate all results Y_j. Third, all important variable and results are stored. The cycle is repeated several times until an appropriated distribution function is reached. The stored results may used to calculate the standard deviation, the distribution functions and correlations between the input or output quantities [77].

7.2 Estimation of the measurement uncertainty of the absolute spectral responsivity of the trap detectors

7.2.1 Definition of the model

The basic model of the absolute spectral responsivity of the trap detectors can be obtained directly from equation (5.1) in section 5.1. That is,

$$s(\lambda)=\frac{I_{\mathrm{ph}}}{\Phi(\lambda)}=\frac{I_{\mathrm{ph}}}{\Delta P\cdot 1/\tau(\lambda)\cdot 1/\alpha(\lambda)}, \tag{7.11}$$

where I_{ph}, ΔP, $\tau(\lambda)$ and $\alpha(\lambda)$ are the already known photocurrent, electrical power difference, transmittance coefficient and absorbance coefficient of the Brewster-window, respectively. However, the process of evaluation of the measurement uncertainty requires a detailed model of the measurand composed of all real measurement parameters and the corresponding correction factors; e.g. the photocurrent I_{ph} is not measured directly, but by means of a trans-impedance amplifier whose output is $V_0 = I_{\mathrm{ph}}\cdot R_\mathrm{f}$. Thus, substituting the real measurement parameters in (7.11) and the corresponding correction factors, yield,

$$S(\lambda)=\frac{I_{\mathrm{ph}}}{\Phi(\lambda)}=\frac{I_{\mathrm{ph}}}{\Delta P\cdot 1/\tau(\lambda)\cdot 1/\alpha(\lambda)}=\frac{V_0}{R_{\mathrm{f}}}\cdot\frac{R\cdot\tau(\lambda)\cdot\alpha(\lambda)}{(V_{\mathrm{U1}}-V_{\mathrm{U2}})\cdot(V_{\mathrm{i1}}-V_{\mathrm{i2}})}\cdot H_{\mathrm{neq}}$$

$$=\frac{Q\cdot R\cdot\tau(\lambda)\cdot\alpha(\lambda)}{R_{\mathrm{f}}}\cdot H_{\mathrm{neq}} \tag{7.12}$$

with $Q=\frac{V_0}{(V_{\mathrm{U1}}-V_{\mathrm{U2}})\cdot(V_{\mathrm{i1}}-V_{\mathrm{i2}})}$,

where H_{neq} is the heating non-equivalence. Note that the feedback resistance R_{f} is equivalent to the gain of the trans-impedance amplifier. For simplicity, the value of H_{neq} was supposed 1 and just its uncertainty was taken into account for the estimation of the uncertainty of $S_{\mathrm{trap}}(\lambda)$. The heater voltage V_{Ux}, the voltage V_{ix} measured over the external resistance R = 1 kΩ, and the output voltage of the trans-impedance amplifier V_0 were measured with three 8 ½-digits digital voltmeters (HP 3458A, high-stability option). All these three voltage signals are put together in the factor Q whose standard uncertainty was estimated by the standard deviation of 400 measurements (see equation (7.3)).

7.2.2 Evaluation of the measurement uncertainty

The evaluation of the standard measurement uncertainty was carried out by using the commercial and validated software "GUM Workbench" existing at the PTB, which follows the guidelines of the GUM. Table 7.2 shows the uncertainty budget for the measurement of the responsivity of the InGaAs-trap for a wavelength of 1550 nm. The major and dominant uncertainty is the one associated with the measurement of the window transmission of the cryogenic radiometer for 1550 nm, i.e. 190×10^{-6}. It accounts for up to about 99.9 % of the total uncertainty making the uncertainties associated to the measurement of the electrical power, the heating non-equivalence and the cavity absorbance almost negligible. The estimation of the standard uncertainty was also carried out for the rest of the wavelengths of the whole measured spectrum for both trap detectors, see Figure 7.2. Here in both cases the maximum relative standard uncertainty is around 4.2×10^{-4} at a wavelength of 1520 nm.

Table 7.2 Example of the uncertainty budget of the responsivity of the InGaAs-trap detector at 1550 nm.

Qty	**Value**	**Standard uncertainty**	**Deg. of freedom**	**Sensitivity coefficient**	**Uncertainty contribution**	**Index**
Q	10.7446659 V^{-1}	21.0×10^{-6} V^{-1} (Type A)	399	0.10	2.1×10^{-6} A/W	0.0%
R_f	10003.0279 Ω	1.61×10^{-6} Ω (Type B)	50	-110×10^{-6}	-17×10^{-11} A/W	0.0%
R	1000.00530 Ω	300×10^{-6} Ω (Type B)	50	0.0011	3.2×10^{-8} A/W	0.0%
α	0.99977700	4.04×10^{-6} (Type B)	∞	1.1	4.3×10^{-6} A/W	0.0%
τ	0.99959600	190×10^{-6} (Type A)	39	1.1	200×10^{-6} A/W	99.9%
H_neq	1.00000000	3.10×10^{-6} (Type B)	∞	1.1	3.3×10^{-6} A/W	0.0%
		Combined standard uncertainty, u_c:			**20×10^{-5} A/W**	

Expression of the result according to GUM:

Quantity: $S_\text{trap}(\lambda)$

Measurement conditions: wavelength 1550 nm; beam diameter $\phi = 2$ mm ± 0.02 mm ($1/e^2$);

Temperature 20.5 °C ± 0.5°C

Value: 1.073 47 A/W

Standard measurement uncertainty: 21×10^{-5} A/W

Relative measurement uncertainty: 0.02 %

Coverage factor k: 2.1

Confidence level: 95.45 % (t-Table)

Effective degree of freedom ν_eff: 39

$S_\text{trap}(\lambda) = (1.073\,47 \pm 20\times10^{-5})$ A/W

The wavelength dependence of the standard uncertainty in Figure 7.2 is obviously just a pure effect of the different standard uncertainties of the window transmission measurement. The uncertainty of the window transmission was determined by calculating the standard deviation of 40 consecutive measurements for each wavelength. One may think that the wavelength dependence of the uncertainty of the window transmission measurement is caused by the window transmission dependence on the wavelength. However, the major uncertainty is located at 1520 nm where the transmission of the window is not wavelength dependent (see Figure 4.9 in section 4.4.2). Thus, the major contribution may be ascribed to the whole measurement technique whose repeatability is limited by fine mechanical devices which are used to align (manually) a photodiode, see section 4.4.2.

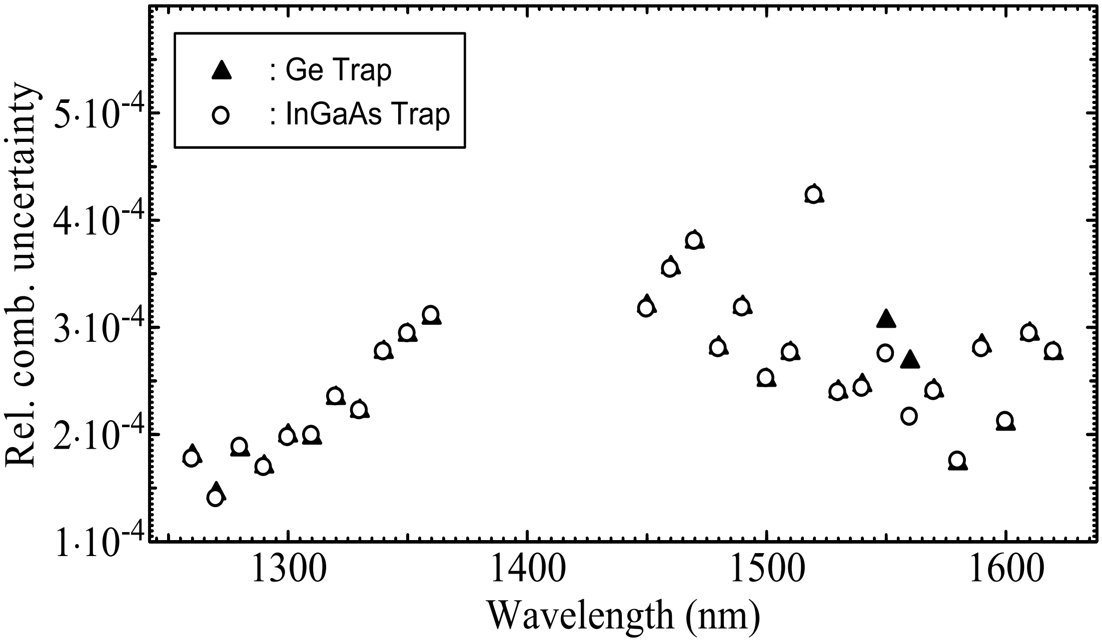

Figure 7.2 Combined relative standard uncertainty of the absolute responsivity measurements of Ge- and InGaAs-trap detectors for each measured wavelength (1260 nm to 1360 nm and 1460 nm to 1620 nm, in steps of 10 nm).

7.3 Estimation of the measurement uncertainty of the nonlinearity of the photodiodes

7.3.1 Definition of the model

In the same way as shown in the previous section, the first step to estimate the measurement uncertainty is the definition of the mathematical model of the measurand. Since the nonlinearity of the photodiodes responsivity was measured with different methods (see section 5.4), the resulting measurement uncertainty will depend also on the measurement method employed. Therefore, the measurement uncertainty should be evaluated individually for each method. Table 7.3 summarizes the three models of the measurand (nonlinearity) of the corresponding three methods; flux-addition-, DSR- and "relative"-method. All models are expressed in terms of their measurement parameters and correction factors:

$f_{\mathrm{lin\_amp}}$: Correction factor due to the possible nonlinearity of the transimpedance amplifier and the measurement equipment, for example, the linearity of the voltmeter.

$f_{\mathrm{lin\_diode}}$: Correction factor associated to the linearity of the reference photodiode used with the "relative"-method.

f_{ref}: Correction factor associated to possible variation of the backscatter and reflections on the connector ends of the fiber occurring during the measurement process. Backscatter and reflection variations may be present in the flux-addition setup when the two apertures are open or closed.

f_{dif}: Correction factor associated to possible variation of the photodiode responsivity for the case when I_a and I_b are not equal. Although these signals are adjusted to be equal for each measurement (see section 5.4) a small residual different may be left.

f_{rep}: Correction factor associated to the repeatability of the measurement system. Here possible random changes of the temperature, wavelength, etc. occurring during the measurement process are taken into account.

Table 7.3 List of the models for the nonlinearity measurement with respect to the measurement method employed: (a) Flux-addition-, (b) "relative"- and (c) DSR-method. All the models are expressed in terms of the measurement parameters and the corresponding correction factors.

(a) Flux-addition-method:

$$NL_{total}(I_{\mathrm{a}};I_{\mathrm{x}}) = \sum_{\mathrm{k}=1}^{n} NL_{\mathrm{k}} \tag{7.13}$$

with $NL_{\mathrm{k}}(I_{\mathrm{a}};I_{\mathrm{x_k}}) = \left(\dfrac{I_{\mathrm{a+b}} - I_0}{I_{\mathrm{a}} + I_{\mathrm{b}} - 2 \cdot I_0} - 1 \right) \cdot f_{\mathrm{lin\_amp}} \cdot f_{\mathrm{ref}} \cdot f_{\mathrm{dif}} \cdot f_{\mathrm{rep}}$

$$= \left(\frac{V_{\mathrm{a+b}} - V_0}{V_{\mathrm{a}} + V_{\mathrm{b}} - 2 \cdot V_0} - 1 \right) \cdot f_{\mathrm{lin\_amp}} \cdot f_{\mathrm{ref}} \cdot f_{\mathrm{dif}} \cdot f_{\mathrm{rep}} \tag{7.13a}$$

Note: I_0 is the dark current of the photodiode.

(b) "Relative"-method:

$$NL = \left(\frac{S_{\mathrm{DUT}}}{S_{\mathrm{ref}}} - 1 \right) \cdot f_{\mathrm{lin\_amp}} \cdot f_{\mathrm{lin\_diode}} \cdot f_{\mathrm{rep}} = \left(\frac{V_{\mathrm{DUT}}}{V_{\mathrm{ref}}} - 1 \right) \cdot f_{\mathrm{lin\_amp}} \cdot f_{\mathrm{lin\_diode}} \cdot f_{\mathrm{rep}} \tag{7.14}$$

(c) DSR-method:

$$NL(i_0;i_{\mathrm{x}}) = \left(\frac{S(\Phi_{\mathrm{bias}})}{S(\Phi_{\mathrm{ref}})} - 1 \right) \cdot f_{\mathrm{lin\_amp}} \tag{7.15}$$

with

$$S(\Phi_{\mathrm{bias}}) = I_{\mathrm{bias}}(\Phi_{\mathrm{bias}}) \cdot \left[\int_0^{I_{\mathrm{bias,x}}} \frac{dI_{\mathrm{bias}}}{\mathfrak{S}(I_{\mathrm{bias}})} \right]^{-1} \text{ and}$$

$$S(\Phi_{\mathrm{ref}}) = I_{\mathrm{ref}}(\Phi_{\mathrm{ref}}) \cdot \left[\int_0^{I_{\mathrm{ref,x}}} \frac{dI_{\mathrm{bias}}}{\mathfrak{S}(I_{\mathrm{bias}})} \right]^{-1}$$

7.3.2 Evaluation of the measurement uncertainty

For convenience, the evaluation of the measurement uncertainty of the nonlinearity measured with the flux-addition- and "relative"- method were carried out by employing the GUM procedure, because in these two cases the models are linear and easy to handle (see Table 7.3). The evaluation of the uncertainty was carried out for the nonlinearity of the InGaAs-photodiode responsivity shown in Figure 6.30, since here all three methods were employed.

Table 7.4 shows, as an example, the uncertainty budget of the local nonlinearity of the InGaAs-photodiode responsivity corresponded to one level of photocurrent; 4.6 mA (≈ 4.5 mW) measured with the flux-addition method. The combined standard uncertainty obtained in this case is 1.13×10^{-6}. The major contribution to the uncertainty is the one associated to the repeatability of the measurement system. In general, the measurement uncertainties of the voltages and linearity of the trans-impedance amplifier are almost negligible. Thus, the same procedure is employed to evaluate the rest of the local nonlinearities NL_{k}. By knowing the standard uncertainty of each local nonlinearity NL_{k}, the standard uncertainty of the total nonlinearity $NL_{\mathrm{total}}(I_{\mathrm{a}}; I_{\mathrm{x}})$ is obtained by applying the equation (7.6) to equation (7.13), which results as,

$$u_{\mathrm{c}}\left(NL_{\mathrm{total}}\right)=\left[\sum_{k} u_{\mathrm{c}}\left(NL_{k}\right)^{2}\right]^{1/2} ; \qquad (7.16)$$

that is, the standard uncertainty of the total nonlinearity $u_{\mathrm{c}}(NL_{\mathrm{total}})$ is the square-root-sum of all individual uncertainties $u_{\mathrm{c}}(NL_{\mathrm{k}})$, whose value increases with the number of measurement steps (local nonlinearities) and the measurement interval $(I_{\mathrm{a}};I_{\mathrm{x}})$. In Table 7.5 the standard uncertainties of the local nonlinearity and the total nonlinearity for a photocurrent range between 0.59 mA and 6.87 mA are shown. Here, the total nonlinearity was normalized to $I_{\mathrm{ph}} \approx 1$ mA. Note that in this case the difference between the combined standard uncertainties $u_{\mathrm{c}}(NL_{\mathrm{k}})$ and $u_{\mathrm{c}}(NL_{\mathrm{total}})$ is not significant because of the few number of measurement steps.

Table 7.4 Uncertainty budget of the local nonlinearity of the photodiode (InGaAs 35PD10M) responsivity by using the flux-addition-method. The evaluation of the uncertainty was carried out for a photocurrent of 4.6 mA and a wavelength of 1550 nm**.**

Qty	**Value**	**Standard uncertainty**	**Deg. of freedom**	**Sensitivity coefficient**	**Uncertainty contribution**	**Index**
V_0	11.449×10^{-6} V	577×10^{-9} V (Type B)	∞	0.21	120×10^{-9}	1.1%
V_a	2.363263 V	577×10^{-9} V (Type B)	∞	-0.21	-120×10^{-9}	1.1%
V_b	2.364596 V	577×10^{-9} V (Type B)	∞	-0.21	-120×10^{-9}	1.1%
V_{a+b}	4.685828 V	577×10^{-9} V (Type B)	∞	0.21	120×10^{-9}	1.2%
$f_{\mathrm{lin\_amp}}$	0.9999839	9.33×10^{-6} (Type B)	∞	-0.0089	-83×10^{-9}	0.5 %
f_{ref}	1.0000000	57.7×10^{-6} (Type B)	∞	-0.0089	-510×10^{-9}	20.6 %
f_{dif}	1.0000000	27.7×10^{-6} (Type B)	∞	-0.0089	-250×10^{-6}	4.8%
f_{rep}	1.0000000	106×10^{-6} (Type A)	9	-0.0089	-940×10^{-9}	69.5 %
NL:	-0.0088875	Combined standard uncertainty, u_c(NL):			$\pm 1.13\times10^{-6}$	
		Expanded uncertainty *U*(NL): (v_{eff} : 18, $k_{95\%} = 2.2$)			$\pm 2.2\times10^{-6}$	

Table 7.5 Standard uncertainty of the local NL_k and total nonlinearity NL_{total} for a photocurrent I_{ph} range between 0.59 mA and 6.87 mA. The total nonlinearity NL_{total} is calculated relative to a photocurrent $I_{ph} \approx 1$ mA.

I_{ph} (mA)	NL_k (rel)	$u_c(NL_k)$	NL_{total} (rel)	$u_c(NL_{total})$
0.5872	-1.3875×10^{-6}	1.24×10^{-4}	11.112×10^{-5}	1.24×10^{-4}
1.1713	-11.111×10^{-5}	1.00×10^{-6}	0	0
2.352	-29.608×10^{-5}	5.00×10^{-7}	-40.720×10^{-5}	5.00×10^{-7}
4.686	-88.863×10^{-4}	3.08×10^{-6}	-92.935×10^{-4}	3.12×10^{-6}
6.871	-0.2715	93.70×10^{-6}	-0.2808	93.75×10^{-6}

Table 7.6 shows, also as an example, the uncertainty budget of the nonlinearity measured with the "relative" method for a photocurrent of 4.6 mA. The combined standard uncertainties obtained in this case is 3.86×10^{-6}. Here, the major uncertainty is the one associated with the linearity measurement of the reference photodiode. The standard uncertainty of the reference photodiode is referred to an uncertainty of the total nonlinearity obtained after 7 local nonlinearities. Uncertainties associated to the linearity of the amplifier and the repeatability of the measurement system are almost negligible.

For the case of the measurement uncertainty evaluation of the nonlinearity measured with the DSR-method, the Monte Carlo method described in section 7.1.2 was used, which is more convenient because the mathematical model of the DSR-method is nonlinear and more complicated than the other two, see Table 7.3. The Monte Carlo simulation was carried out with a commercial software (Hypradata beta 3) that uses the evaluation procedure described in Figure 7.1, see section 7.1.2. In the simulation, the values of the input quantities i_{bias}, the differential responsivity $\mathfrak{s}\,(i_{bias})$ and the correction factor f_{lin_amp} where provided with their corresponding associated standard uncertainties. For example, for $NL = -0.0017$, obtained from $i_{bias} = 3.84$ mA, $\mathfrak{s}\,(i_{bias}) = 6.81$ V/W and $f_{lin\_amp} = 0.99998$, their corresponding standard uncertainties are 3×10^{-6} A (normal), 0.0018 V/W (normal) and 9.33×10^{-6} (rectangular), respectively. After 10000 simulation draws, the estimated standard uncertainty obtained was 1.3×10^{-4}, which correspond to normal probability distribution, see Figure 7.3.

Table 7.6 Uncertainty budget of the nonlinearity of the photodiode (InGaAs 35PD10M) responsivity by using the “relative”-method. The evaluation of the uncertainty was carried out for a photocurrent of 3.2 mA and a wavelength of 1550 nm.

Qty	Value	Standard uncertainty	Deg. of freedom	Sensitivity coefficient	Uncertainty contribution	Index
V_{DUT}	3.23258855V	577×10^{-9} V (Type B)	∞	0.31	180×10^{-9}	21.4 %
V_{ref}	3.30335241 V	577×10^{-9} V (Type B)	∞	-0.31	-170×10^{-9}	20.5 %
f_{lin_amp}	0.9999839	9.33×10^{-6} (Type B)	∞	-980×10^{-6}	-9.1×10^{-9}	0.1 %
f_{lin_diode}	1.0000000	300.0×10^{-6} (Type B)	50	-980×10^{-6}	-290×10^{-9}	57.6 %
f_{rep}	1.0000000	26.6×10^{-6} (Type A)	9	-980×10^{-6}	-26×10^{-9}	0.5 %
NL:	-0.000975	Combined standard uncertainty, u_c(NL):			$\pm 3.86\times10^{-6}$	
		Expanded uncertainty U(NL): (ν_{eff} : ∞, $k_{95\%} = 2$)			$\pm 7.7 \times10^{-6}$	

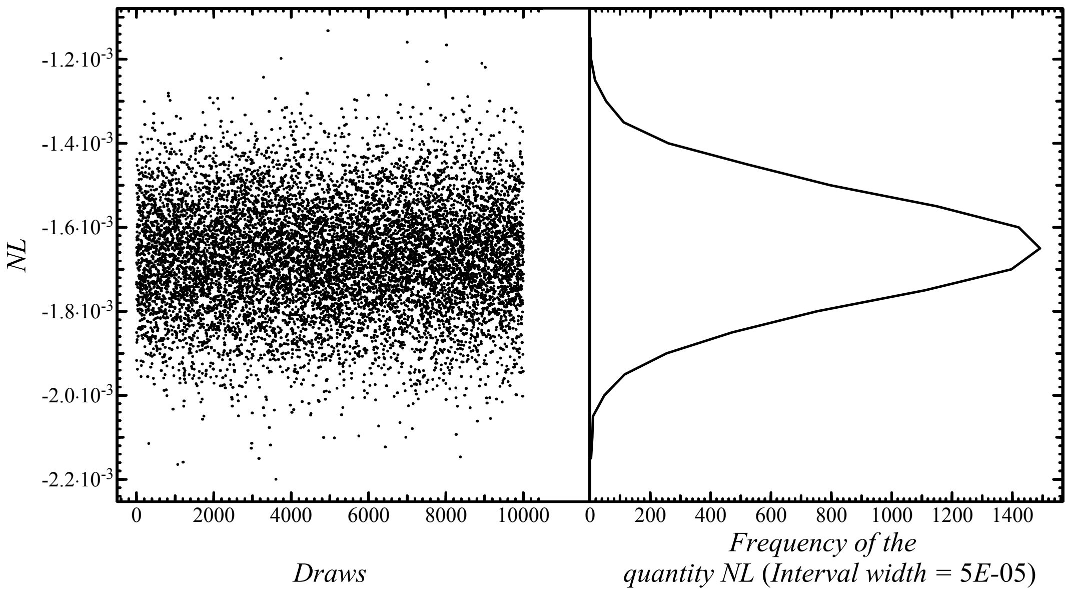

Figure 7.3 Histogram of the *NL*(-0.0017) values obtained with the Monte Carlo simulation after 10000 draws. Left: values of the simulated *NL* and right: histogram of the values.

The standard uncertainty of the nonlinearity of the InGaAs-photodiode responsivity measured with the three methods was estimated for the whole photocurrent range between 0.5 mA and 7 mA (0.5 mW-6.8 mW), see Figure 7.4. All measurement uncertainties were calculated for a reference photocurrent of 1 mA. In all cases the uncertainty increases for higher photocurrent, e.g. for the flux-addition- and the "relative"-method the maximum uncertainty reached is 9×10^{-5} and for the DSR-method the maximum uncertainty reached is 4.5×10^{-4}. As for the flux-addition method, the uncertainty of the "relative"- and DSR-method depends also on the number of measurement steps. As an example, in Figure 7.4 the measurements of the nonlinearity obtained with the DSR-method were reduced to 9 measurement steps, and the maximum standard uncertainty reached was 2.6×10^{-4}. On the other hand, the uncertainty obtained with the "relative"-method is also depending on the measurement steps because in this case the dominant uncertainty is the one associated to the nonlinearity reference photodiode, which is measured previously with one of the two absolute methods already mentioned.

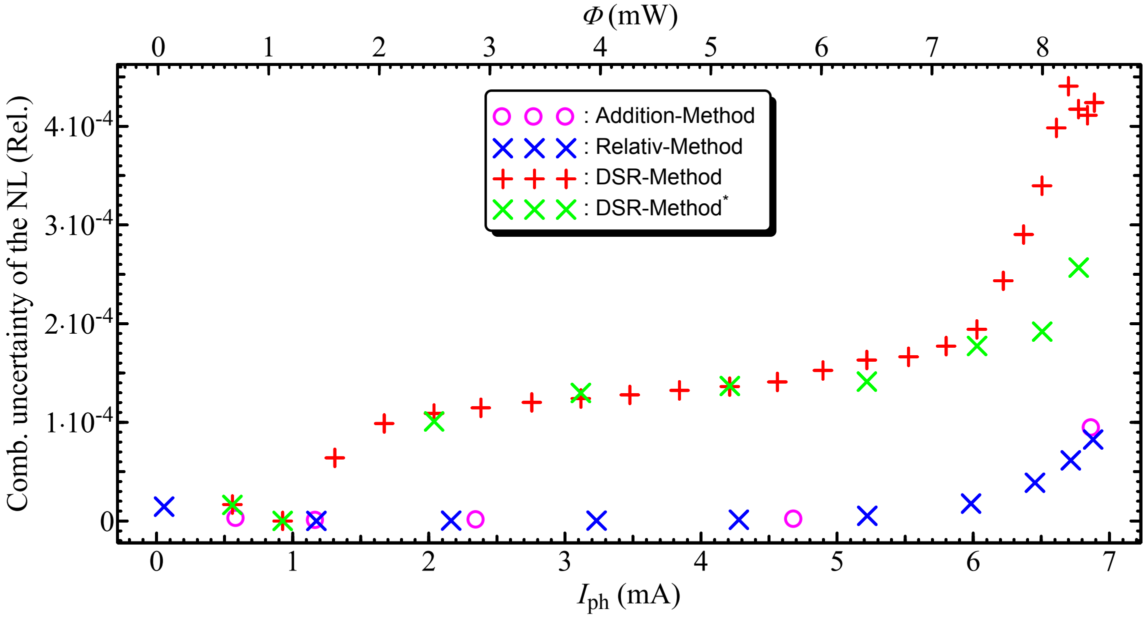

Figure 7.4 Standard combined uncertainty of the nonlinearity of the InGaAs-photodiode responsivity measured with the three methods (Flux-add-, relative- and DSR-method). The standard uncertainty depends on the optical power level and the number of measurement steps, see for example DSR-method (+) and (×) in the graph.

In general, the standard uncertainty obtained with the DSR-method is higher than the one obtained with the other two methods and it increases strongly from 6 mA. This behavior can be attributed to the uncertainty associated to the measurement of the differential responsivity $\tilde{s}$, which in this case is the dominant uncertainty. Figure 7.5 shows the relative standard deviation of $\tilde{s}$, where a clear instability is observed precisely for photocurrents higher than 6 mA. One should consider here that the differential responsivity $\tilde{s}$ is measured directly with a Lock-in amplifier and the Φ_{bias} and Φ_{mod} (constant and low radiation) generated by two diode lasers operating at 1550 nm and 980 nm, respectively, see section 6.7. Thus, the repeatability of the measurement $\tilde{s}$ depends strongly on the stability of Φ_{mod} and $\Phi_{\mathrm{bias.}}$ Thereby, in order to reduce the measurement uncertainty of $\tilde{s}$, a monitor photodiode should be used.

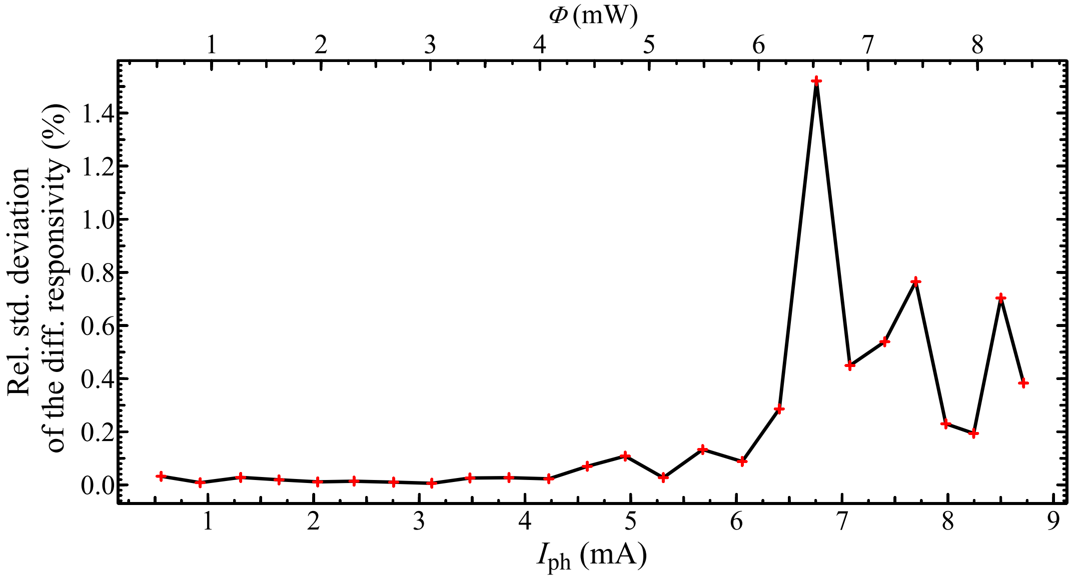

Figure 7.5 Relative standard deviation of the differential responsivity $\tilde{s}$ of the InGaAs-photodiode.

8 Summary and outlook

In this work the optical characterization of Ge- and InGaAs-trap detector and single photodiodes was presented. The optical characterization of these detectors gives the base for the improvement of the actual responsivity scale based on semiconductor detectors for the near infrared, especially where the optical fiber communications are operated. The characterization of the detectors included the measurement of the following optical parameters: absolute spectral responsivty, reflectance, quantum efficiency, non-uniformity and nonlinearity.

In order to achieve the lowest measurement uncertainty, the absolute spectral responsivity of the Ge- and InGaAs-trap detectors was measured by direct calibration against the cryogenic radiometer of the PTB. A new measurement setup was established which uses two tunable laser diodes as radiation sources. A fiber optic and a collimator were used to prepare the beam to reach quality required by the cryogenic radiometer. The measurements were carried out in the spectral range between 1260 nm and 1360 nm and between 1460 nm and 1620 nm. The optical characterization of the two major error sources of the cryogenic radiometer; the Brewster-window transmission and the cavity absorption, was also carried out. The Brewster-window, made of S1-UV schlieren grade fused silica, presents an OH absorption band between 1320 nm and 1480 nm, reaching a maximum value of approx. 4.5 % at 1382 nm. On the other hand, the absorption coefficient of the cavity (0.999777 ± 0.000014) of the cryogenic radiometer is almost constant for the whole spectral range measured. A detailed analysis of the standard uncertainty of the absolute responsivity was performed. Here, the relative standard uncertainty achieved is less than 5×10^{-4} for the whole spectral range measured. The major uncertainty is the one associated to the measurement of the optical transmission of the Brewster-window, which is caused mainly due to the "low" repeatability and reproducibility of the measurement setup.

The absolute spectral responsivity of the trap detectors investigated was compared with the existing spectral responsivity scale of the PTB based on a thermopile detector. That is, the same trap detectors were calibrated against the thermopile. The deviation obtained between the scales is less than ± 0.3 % and less than ± 0.2 % for the Ge- and InGaAs-trap detector, respectively. The agreement is therefore well within the combined standard uncertainty.

The spectral reflectance and responsivity at normal and oblique incidence of the Ge- and InGaAs-single photodiodes were measured and modeled. The reflectance and responsivity were measured for *s*- and *p*-polarized radiation at 7° and 45° incidence angles over the spectral range from 1260 nm to 1640 nm. The spectral reflectance of the Ge- and InGaAs-photodiodes was modeled considering them as an optical thin film assembly. For the case of the *p-n* Ge-photodiode, a simple optical assembly of an AR coating and substrate is considered. However, for the case of the *p-i-n* InGaAs-photodiode a multilayer structure is considered. In order to generalize a solution for both cases, the spectral reflectance of the photodiodes was modeled by using the matrix approach, which gives a general solution for a single and multilayer optical assembly. Furthermore, the refractive indexes of the different layers and their thickness of both photodiodes were obtained by using least-squares fitting. From the model of the reflectance and by considering the internal quantum efficiency of the photodiodes to be independent of the incident angle and the polarization, the responsivity of the single photodiodes and trap detectors was also calculated.

For the Ge and InGaAs single photodiodes, the relative difference obtained between modeled and calculated responsivity is approx. ≤ 1 % and ≤ 3 %, respectively. On the other hand, the difference between the modeled and calculated spectral responsivity of the Ge- and InGaAs-trap detectors was 1 % and ≤ 2 %, respectively. These differences are comparable to the one reported for Si-photodiodes.

The spatial non-uniformity of the responsivity of the single- and trap-detectors was investigated at 1310 nm and 1550 nm with a beam spot size of 1 mm in diameter. From the measurement of the spatial non-uniformity, the change of the responsivity of the single photodiodes and trap detectors was quantified as a function of different incident beam diameters and beam positions on the sensitive area. For the single photodiodes, irradiated with a spot diameter ≤ 8 mm, a maximal deviation of the responsivity of 0.3 % was observed. For the case of the trap detectors, the relative deviation of the responsivity was ≤ 0.1 % for beams diameters between 1 mm and 4 mm.

The change of the responsivity as a function of a beam displacement was quantified for a beam spot diameters of 2 mm and 3 mm relative to the center of the detectors. For the trap detectors a displacement of the beam is critical due to its field of view. For example, a displacement of just 2 mm of a spot beam with 3 mm of diameter may generate a deviation of the responsivity up to approx. 9 %. Thus, in general, in order to limit the error of the measurement of the responsivity of a single photodiode and trap detector to 0.1 %, the beam position should be better than 1 mm with respect to the center of the sensitive area of the detectors investigated in this work.

The measurement of the nonlinearity of the photodiodes responsivity was carried out with three measurement setups based on three different methods: flux-addition, DSR- and “relative”-method, respectively. The aim in this case was not only the investigation of the nonlinearity of the photodiodes responsivity, but also to prove the feasibility of new measurement setups based on the DSR- and “relative”- method to measure the nonlinearity of photodiodes at high irradiance levels. The setups tested are based on a fiber optic coupler and use as a radiation source an Erbium-Doped Fiber Amplifier tuned to 1550 nm and a diode laser at 980 nm, whose maximal optical powers available are 500 mW and 300 mW, respectively. However, due to the high nonlinearity of the photodiodes, the nonlinearity of the photodiodes was measured only up to 28 mW ($E \approx 90$ mW/mm^2) in order to avoid any damage of the photodiodes.

All photodiodes tested present a nonlinearity due to the saturation of the photodiodes themselves. For a wavelength of 1550 nm, the Ge- and InGaAs-photodiodes are linear up to approx. 7 mW and 3 mW, respectively. The Ge- and InGaAs- photodiodes show a maximal nonlinearity of 40 % at 28 mW and of 25.5 % at 8.4 mW, respectively.

The measurement uncertainty of the nonlinearity, measured with the three methods, depends on the optical power level and the number of measurement steps. For example, the combined standard uncertainty estimated for the three methods is less than 0.02 % for 10 measurement steps distributed between approx.1 mW and 9 mW.

In general, the measurement setups for the measurement of the nonlinearity investigated, based on the DSR- and “relative”- method, have shown to be a good alternative to measure the nonlinearity of the photodiodes. The optical components needed are less than for the flux-addition method and the measurement process is also faster.

The measurements uncertainties and models of the optical characteristics of the Ge- and InGaAs-trap detectors and single photodiodes presented in this work may be still improved. Some suggestions for future work are listed in the following:

- The measurement uncertainty of the absolute spectral responsivity of the trap detectors obtained by direct comparison against the cryogenic radiometer can be improved significantly by reducing the measurement uncertainty of the transmittance of the Brewster-angle window. In principle, it should be possible by automating the measurement process, which will achieve a better reproducibility of the measurements. Another possibility is to implement the concept of window-correction-free transfer proposed by Stock *et al* in [78]. This concept proposes to place the transfer detector in a vacuum chamber together with the cryogenic radiometer behind one Brewster-angle window. In that way, because both the cryogenic radiometer and the transfer are affected by the transmittance of the same Brewster-angle window, the transmittance correction is eliminated.

- The model of the responsivity of the photodiodes can be improved by modeling their internal quantum efficiency with an appropriate representation for the carrier-collection efficiency dependence on the penetration depth. Here, the models developed by Geist *et al* [52], Gentile *et al* [8] or Ferrero *et al* [79] for Si-photodiodes may be used.

- The model of the nonlinearity of the photodiodes can be improved by knowing the exact value of the shunt resistance as a function of the optical power as well as the series resistance as function of the irradiated area on the sensitive area of the photodiode. The shunt resistance can be obtained from the *I-V* curves of the diodes for several optical power levels. The series resistance may depend on the thickness of the substrate, the diffuse area of the junction and the contacts.

- The measurement systems based on the DSR or "relative" method studied in this work can be used to determinate the linearity factor of a detector for high optical power measurements, e.g. an integrating sphere radiometer, which can be used as a transfer standard. In this way, the calibration capability in the optical fiber power meters at the PTB can be extended up to ≈ 500 mA.

9 References

1 Jia-Ming Liu, *Photonic Devices*, Cambridge University Press 2005, pp 926-927

2 K. D. Stock, "Spectral ageing pattern of carefully handled silicon photodiodes," Measurement **5**, 141-143 (1987)

3 J.E. Martin, N.P. Fox and P.J. Key, "A Cryogenic Radiometer for Absolute Radiometric Measurements," Metrologia **21**, 147-155 (1985)

4 C.C. Hoyt and P.V. Foukal, "Cryogenic Radiometer and their Application to Metrology," Metrologia **28**, 163-167 (1990)

5 R. Goebel, R. Pello, K.D. Stock and H. Hofer, "Direct comparision of cryogenic radiometers from the BIPM and the PTB," Metrologia **34**, 257-259 (1997)

6 K.D. Stock, H. Hofer, J.G. Suarez Romero, L.P. Galvan and W. Schmid, "Cryogenic radiometer facility of the CENAM and first international comparision," Metrologia **37**, 269-271 (2000)

7 J. F. Clare and K.M Nied, "Realization of a photometric scale based on cryogenic radiometry," Metrologia **35**, 251-254 (1998)

8 T. R. Gentile, J. M. Houston, C. L. Cromer, "Realization of a scale of absolute spectral response using the National Institute of Standards and Technology high-accuracy cryogenic radiometer," Applied Optics **35**, 4392-4403 (1996)

9 J. H. Lehman and C.L. Cromer, "Optical tunnel-trap detector for radiometric measurements," Metrologia **37**, 477-480 (2000)

10 K. D. Stock and R. Heine, "Spectral characterization of InGaAs trap detectors and photodiodes used as transfer standards," Metrologia **40**, S163-S166 (2003)

11 K. D. Stock and R. Heine, "Spectral characterization of Ge trap detectors and photodiodes used as transfer standards," Metrologia **37**, 449-452 (2000)

12 L. P. Boivin and T. C. Smith, "Electrically calibrated radiometer using a thin film thermopile (E)," Applied Optics **17**, 3067- (1978)

13 P. Corredera, M. L. Hernanz, J. Campos, A. Corróns, A. Pons and J. L. Fontecha, "Comparison between absolute thermal radiometers at wavelengths of 1300 nm and 1550 nm," Metrologia **37,** 543-546

14 E. Gaviot, F. Polet, F. Raucoules, F. Brachelet and K. Ziouche, "Planar differential radiometers: a quantitative approach to designing enhanced units," Meas. Sci. Technol. **10**, 84-92 (1999)

15 H. Lehman, E. Theocharous, G. Eppeldauer, C. Pannell, "Gold-black coating for freestanding pyroelectric detector," Meas. Sci. Technol. **14**, 916-922 (2003)

16 M. López, H. Hofer, S. Kück, "Measurement of the absorptance of a cryogenic radiometer cavity in the visible and near infrared," Metrologia **42**, 400 – 405 (2005).

17 M. López, H. Hofer, K. D. Stock, J. C. Bermúdez, A. Schirmacher, F. Schneck, S. Kück, "Spectral reflectance and responsivity of Ge- and InGaAs-photodiodes in the near-infrared: measurement and model," Applied Optics **46**, 7337-7344 (2007).

18 H A Macleo, *Thin-Film Optical Filters* (3rd ed. Institute of Physics Publishing 1986) pp. 37-47

19 L. - P. Boivin, "Spectral responsivity of various types of silicon photodiode at oblique incidence: comparison of measured and calculated values," Applied Optics **40**, 485-491 (2001)

20 J. Metzdorf, W. Möller, T. Wittchen and D. Hünerhoff, "Principle and Application of Differential Spectroradiometriy, " Metrologia **28**, 247-250

21 Sanders, C. L., "A photocell linearity tester", Applied Optics **1**, 207 (1962)

22 S. M. Sze, *Physics of Semiconductors*, 2nd ed. (John Wiley & Sons, 1981), pp. 749-782

23 David Wood, *Optoelectronic Semiconductor Devices,* (Prentice Hall, 1994), pp. 249-325

24 W. Budde, *Optical radiation measurement*, Vol. 4, (Academic Press, 19839, pp. 215-275

25 H. Melchior, "Demodulation and Photodetection Techniques," F.T. Arecchi and E.O. Schulz-Dubois, Eds., *Laser Hanbook*, Vol. **1**, North-Holland, Amsterdam, 1972, pp. 725-835

26 W. W. Gartner, "Depletion Layer Photoeffects in Semiconductors," Phys. Rev. **116**, 84 (1959)

27 N. P. Fox, "Trap Detectors and their Properties," Metrologia, **28**, 197-202 (1991)

28 Toomas Kübarsepp, Petri Kärhä and Erkki Ikonen, "Characterization of a polarization-independent transmission trap detector," Applied Optics, **36**, 2807-2812 (1997)

29 John H., Lehman and Christopher L. Cromer, "Optical Trap Detector for Calibration of Optical Fiber Powermeters: Coupling Efficiency," Applied Optics, **41**, 6531-6536 (2002)

30 Putley, E. H., *Thermal Detectors. Inc* "Optical and Infrared Detectors" (R. J. Keyes, ed.), Chapter 3. (Springer-Verlag, Berlin and New York 1980)

31 Klaus D. Stock, Stefan Kück, Friedhelm Brandt, "Laserradiometrie," PTB-Mitteilungen, 113, 33-43 (2003)

32 *A Guide to Reflectance Coatings and Materials*, Labsphere, pp. 4-8

33 *A Guide to Integrating Sphere Radiometry and Photometry*, Labsphere, pp. 4-5

34 K.D. Stock and H. Hofer, “PTB primary standard for optical radiant power: transfer-optimized facility in the clean-room center,” Metrologia **32**, 545-549 (1995/96)

35 http://www.mellesgriot.com/pdf/CatalogX/X_04_11-13.pdf

36 K. M. Nield, J. F. Clare, J. D. Hamlin and A. Bittar, “Calibration of a trap detector against a cryogenic radiometer,” Metrologia **35**, 581-586 (1998)

37 C. C. Hoyt and P. V. Foukal, “Cryogenic Radiometers and their Application to Metrology,” Metrologia **28**, 163-167(1991)

38 *LaseRad User´s Manual Revision 1.1*, Cambridge Research & Instrumentation Inc. (CRI, 1990), pp. 67

39 M. López, H. Hofer and S. Kück, “High accuracy measurement of the absolute spectral responsivity of Ge and InGaAs trap detector by direct calibration against an electrically calibrated cryogenic radiometer in the near-infrared,” Metrologia **43**, 508-514 (2006)

40 IEC, International Standard IEC1315, *Calibration of fiber optic power meters* (International Electrotechnical Commission, Ed. 1) 1995

41 A. R. Schaefer, E. F. Zalewski, and Jon Geist, "Silicon detector nonlinearity and related effects,” Applied Optics 22, 1232-1236

42 Budde, W, “Multidecade linearity measurement on Si-photodiodes,” Applied Optics **18**, 1555 (1979)

43 Stock K. D., “Si-Photodiode spectral nonlinearity in the infrared,” Applied Optics **25**, 830-832 (1986)

44 C. L. Sanders, “Accurate measurement and corrections for nonlinearity in radiometer,” J. Res. Natl. Bur. Stand. Sect. A **76**, 437-453 (1972)

45 K. D. Mielenz and K. L. Eckerle, “Spectrophotometer linearity testing using the doble-aperture method,” Applied Optics **11**, 2294-2303 (1972)

46 M. A. Lind, “Measurement of the absolute spectral response of detectors,” in *Proceeding of the Electro-Optics System Design Conference* (Industrial & Scientific Conference Management, Chicago, III), pp. 55-58

47 E. F. Zalewski and J. Geist, “Solar cell spectral response characterization,” Applied Optics **18**, 3942-3947 (1979)

48 Shao Yang, Igor Vayshenker, et. a. “Optical nonlinearity: Simulation,” NIST Technical note 1376, 1995

49 J. Metzdorf, “Calibration of solar cells. 1: The differential spectral responsivity method,” Applied Optics **26**, 1701-1708 (1987)

50 I. Vayshenker, H. Haars, X. Li, J. H. Lehman, D. J. Livigni, “Optical-Fiber Power Meter Comparison between NIST and PTB,” J. Res. Natl. Inst. Stand. Technol. **108**, 391-394 (2003)

51 I. Vayshenker, H. Haars, X. Li, J. H. Lehman, D. J. Livigni, “Comparison of optical-power meters between the NIST and the PTB,” Metrologia **37**, 349-350 (2000)

52 J. Geist, E. F. Zalewski, and A. R. Schaefer Zalewski, “Spectral response self-calibration and interpolation of silicon photodiodes,” Applied Optics **19**, 3795-3799 (1980)

53 Edward F. Zalewski and C. Richard Duda, “Silicon photodiode device with 100% external quantum efficiency,” Applied Optics **22**, 2867-2873 (1983)

54 Atte Haapalinna, Petri Kärhä, and Erkki Ikonen, “Spectral reflectance of silicon photodiodes,” Applied Optics **37**, 729-732 (1998)

55 J. Campos, P. Corredera, A Pons, A. Corróns and J. L. Fontecha, “Reflectance dependencies of silicon trap detectors,” Metrologia **35,** 455-460 (1998)

56 M. Born, E. Wolf, *Principles of Optic,* 3rd ed. (Pergamon, Oxford, 1965), pp. 40, 632-633

57 Eugene Hecht, *Óptica*, 3a Edicion (Addison Wesley, 1998), pp. 113-118

58 E. D. Palik, *Handbook of Optical Constants of Solids* (New York: Academic 1985) pp. 465-478

59 S. Adachi, *Physical properties of III-V Semiconductor compounds InP, InAs, GaAs, GaP, InGaAs, and InGaAsP,* (John Wiley & Sons, 1992) pp 135-192

60 R. K. Ahrenkiel, “Modified Kramers-Kronig analysis of optical spectra,” J. Opt. Soc. Am. **61**, 1651-1655 (1971)

61 K. F. Palmer, M. Z. Williams, B. A. Budde, “Multiply Substractive Kramers Kronig Analysis of Optical Data,” Applied Optics **37**, 2660-2673 (1998)

62 J. A. Dobrowolski, F.C. Ho, and A. Waldorf, “Determination of optical constants of thin film coating materials based on inverse synthesis,” Applied optics **22**, 3191-3200 (1983)

63 Shu-Chung Chiao, Bertrand G. Bovard, H.A. Macleod, “Optical-constant calculation over an extended spectral region: application to titanium dioxide film,” Appl. Opt. **34**, 7355-7360 (1995)

64 J. Conradi, "Planar germanium photodiodes", Appl. Opt. **14**, 1948-1952 (1975)

65 D. M. Braun, "Design of single layer antireflection coatings for InP/$In_{0.53}Ga_{0.47}As$/InP photodetectors for the 1200-1600 nm wavelength range,” Applied Optics **27**, 2006-2011 (1988)

66 S. B. Youssef, “Optical properties of Zn-doped InP single crystals,” Physica A **235**, 334-344 (1997)

67 G. Eppeldauer and J. E. Hardis, “Fortheen-decade photocurrent measurements with large-area silicon photodiodes at room temperature,” Applied Optics **30**, 3091-3099 (1991)

68 Patrck Martin, EL Mostafa Skouri, Lauren Chusseau, Claudie Alibert and Hans Bissessur, “Accurate refractive index measurement of doped and undoped InP by grating coupling technique,” App. Phys. Lett. **67** (7), 881-883 (1995)

69 G.D. Pettit and W. J. Turner, “Refractive Index of InP,” J. App. Phys. **36**, 2081 (1965)

70 Laurent Chusseau, Patrick Martin, Céline Brasseur and Claude Alibert, Philippe Hervé, Philippe Arguel and Francoise Lozes-Dupuy, “Carrier-induced change due to dopping in refractive index of InP: Measurements at 1.3 and 1.5 μm,” Appl. Phys. Letter **69** (20), 3054-3056 (1996)

71 B. Broberg and S. Lindgren, “Refractive index of $In_{1-x}Ga_xAs_yP_{1-y}$ layers and InP in the transparent wavelength region,” J. App. Phys. **59,** 3376-3381 (1984)

72 S. Nevas, F. Manoocheri and E. Ikonen, “Determination of thin-film parameters from high accuracy measurements of spectral regular transmittance,” Metrologia **40**, S200-S2003 (2003)

73 “International Vocabulary of Basic and General Terms in Metrology,” ISO (1998)

74 “Guide to the Expression of Uncertainty in Measurement,” BIPM, IEC, IFCC, ISO, IUPAC, IUPAP, OIML (1995)

75 Maurice G Cox and Bernd R L Siebert, “The use of a Monte Carlo method for evaluating uncertainty and expanded uncertainty,” Metrologia **43**, S178-S188 (2006)

76 “Evaluation of measurement data — Supplement 1 to the “Guide to expression of the uncertainty in measurement” — Propagation of distribution using a Monte Carlo method,” BIPM Joint Committee for Guides in Metrology, Final draft September 2006

77 Winter, Stefan and Sperling, Armin, “Uncertainty analysis of a photometer calibration at the DSR setup of the PTB,” Proceedings of the 2nd CIE Expert Symposium on Measurement Uncertainty, 139-142 (June 2006)

78 K. D. Stock and H. Hofer, “Present State of the PTB Primary Standard for Radiant Power Based on Cryogenic Radiometer,” Metrologia **30**, 291-296 (1993)

79 Alejandro Ferrero, Joaquin Campos, Alicia Pons, and Antonio Corrons, “New model for the internal quantum efficiency of photodiodes based on photocurrent analysis,” Applied Optics **44**, 208-216 (2005)

Acknowledgment

The research work presented in this thesis was carried out in the Laser Radiometry working group 4.13 in the Physikalisch-Technische Bundesanstalt (PTB) in Braunschweig in collaboration with the Centro Nacional de Metrologia (CENAM) of Mexico.

I wish to thank Dr. Klaus Stock, head of the Photometry and Applied Radiometry department at PTB, and Dr. J. Salvador Echeverría Villagómez, head of the Physics Area at CENAM for providing me the support and opportunity to carry out this research work.

I am most grateful to my supervisor, Priv. Doz. Dr. Stefan Kück for his help, guidance and support provided during the development of the research project. I also wish to express my gratitude to Dr. Saulius Nevas and to Dr. Stefan Winter for their encouragement and helpful discussions.

I would like to thank all the members of the Laser Radiometry group: Mr. Hofer, Mr. Taddeo and Mr. Brandt, for their help provided and for sharing their experience during these years with me.

I also wish to thank the Deutsche Akademische Austauschdienst (DAAD) for the financial aid granted for the research project through the PhD scholarship A/03/18297.

Finally, I want to express my sincere gratitude to my wife Jana and to my children Lisa, Elsa and André for their patience and support during my studies and writing of this thesis.

Curriculum Vitae

Name: Marco Antonio López Ordoñez
Address: Gassnerstraße 12
38116 Braunschweig

Date of birth: 13.04.1973
Place of birth: La Huerta, Jal., México
Nationality: Mexican

1979 – 1985	Primary school, La Huerta, Jal., México
1987 – 1985	Technical Secondary school No. 22, La Huerta, Jal., México
1987 – 1990	Technical High school, Cd. Guzmán, Jal., México
1990 – 1994	Bachelor studies in electronic in the Technology Institute of Cd. Guzmán, México
1994 – 2003	Head of the fiber optic and laser power measurement laboratory in the National Center of Metrology (CENAM), México
2000 – 2003	Master in Science studies in Advance Technology in the Research Center in Applied Science and Technology of the National Polytechnic Institute, México
April 2004 – March 2008	PhD studies in the Technischen Universität Braunschweig in collaboration with the Physikalisch-Technischen Bundesanstalt, Germany